Copyright © 1991, by the author(s).
All rights reserved.

Permission to make digital or hard copies of all or part of this work for personal or classroom use is granted without fee provided that copies are not made or distributed for profit or commercial advantage and that copies bear this notice and the full citation on the first page. To copy otherwise, to republish, to post on servers or to redistribute to lists, requires prior specific permission.

# MODELING AND SIMULATION OF REACTION KINETICS IN ADVANCED RESIST PROCESSES FOR OPTICAL LITHOGRAPHY

by

Richard A. Ferguson

Memorandum No. UCB/ERL M91/78

17 September 1991

# MODELING AND SIMULATION OF REACTION KINETICS IN ADVANCED RESIST PROCESSES FOR OPTICAL LITHOGRAPHY

by

Richard A. Ferguson

Memorandum No. UCB/ERL M91/78

17 September 1991

**ELECTRONICS RESEARCH LABORATORY**

College of Engineering
University of California, Berkeley
94720

# MODELING AND SIMULATION OF REACTION KINETICS IN ADVANCED RESIST PROCESSES FOR OPTICAL LITHOGRAPHY

by

Richard A. Ferguson

Memorandum No. UCB/ERL M91/78

17 September 1991

ELECTRONICS RESEARCH LABORATORY

College of Engineering
University of California, Berkeley
94720

TITLE PAGE

# Modeling and Simulation of Reaction Kinetics in Advanced Resist Processes For Optical Lithography

Ph.D. Richard A. Ferguson EECS Department

## ABSTRACT

A general and comprehensive methodology has been developed for the characterization, modeling, and simulation of advanced technologies and complex resist materials for optical lithography. The foundation of this methodology is the new lithography simulation program, ***SAMPLE-ARK,*** which simulates reaction kinetics and diffusion, and their effect upon chemical species concentrations within the resist, during post-exposure processing. The implementation of fundamental mechanisms such as multiple chemical reactions, simultaneous reaction-diffusion, concentration-dependent diffusion, diffusion from outside sources, and multiple species dissolution rate expressions has resulted in a general purpose line-edge profile simulator that has demonstrated the capability of simulating a wide range of complex resist technologies including image reversal, chemical amplification, and silylation processes.

In order to develop mechanistic resist models for simulation in ***SAMPLE-ARK***, material characterization techniques have been evaluated and refined for monitoring the resist behavior during the exposure, post-exposure bake, and development steps. These techniques include measurements of optical transmission, FTIR spectroscopy, and interferometry. New modeling software has been written to facilitate the conversion of experimental data to mechanistic models. These programs range from quantitative FTIR analysis tools to parameter extraction routines for fitting kinetic models to exposure and bake data.

The validity of this methodology has been confirmed through the systematic application to two state-of-the-art deep-UV chemical amplification resists. Predictive models as well as an increased understanding of the important factors that affect the performance of these resists have resulted. For Shipley SNR 248, an acid hardening resist, monitoring of the crosslinking reaction with FTIR spectroscopy lead to the development of a kinetic post-exposure bake model that required an acid loss mechanism to account for quenching of the crosslinking reaction. The derivation of a dissolution rate expression based upon crosslinking-induced molecular weight variations accurately described the development data. For an AT&T t-BOC resist, the resist behavior depended strongly upon chemical composition. Use of an onium salt acid generator minimized sensitivity to the bake conditions as a result of acid loss during the bake. Increasing the loading of either the onium salt or the tosylate acid generator provided improved resist contrast.

Committee Chairman

# ACKNOWLEDGEMENT

First of all, I would like to express my gratitude to Professor Andrew Neureuther for his guidance on this project. His knowledge and dedication have helped convert this project from some vague initial notions to a completed Ph.D. thesis. I would also like to thank Professor William Oldham and Professor Charles Stone who both served on my dissertation committee and Professor Ping Ko for acting as my qualifying committee chairman. They have all provided valuable experience and knowledge over the duration of this project. I am especially grateful to Chris Spence whose friendship and active support as a second "research advisor" have been essential to the completion of this thesis.

My years at Berkeley would not have been as fulfilling without the everyday interactions with the members of the SAMPLE group. Coming into the office would not have been so easy without Friday football games, paper ball matches, and excursions to Zachary's. People such as Gino Addiego, Alex Wong, Kenny Toh, Nelson Tam, Ed Scheckler, Bill Partlo, and Carl Galewski to name just a few have contributed both knowledge and friendship to my life.

Finally, I would like to express special thanks to some people who have made special contributions to the completion of this thesis. My family has given me constant love and support from beginning to end and have always been there when I needed them. Sam Osofsky has also provided a friendship that has somehow made six long years seem much shorter.

I would also like to acknowledge the financial support provided by SEMATECH and the Semiconductor Research Corporation.

# Table of Contents


Chapter 1: Introduction ..... 1

1.1 Simulation of Lithography ..... 1

1.2 Advances in Resist Technology ..... 3

1.3 A General Approach to Resist Modeling and Simulation ..... 5

Chapter 2: Evolution of Resist Modeling and Simulation ..... 14

2.1 Models for Diazo-type Resists ..... 14

2.1.1 Overview of Diazo-type Resist Chemistry ..... 15

2.1.2 Modeling the Exposure ..... 15

2.1.3 Modeling the Post-Exposure Bake ..... 17

2.1.4 Modeling the Development ..... 18

2.2 Models for Advanced Resist Technologies ..... 20

2.2.1 Models for Image Reversal ..... 21

2.2.2 Models for Chemical Amplification ..... 21

2.2.3 Models for Silylation ..... 22

2.3 Resist Simulation ..... 22

2.3.1 Simulation with *SAMPLE* ..... 23

2.4 A General Modeling and Simulation Methodology ..... 24

Chapter 3: The *SAMPLE-ARK* Program ..... 39

3.1 Introduction ..... 39

3.2 Simulation Tool Requirements ..... 40

3.3 Overview Of *SAMPLE-ARK* ..... 41

3.3.1 *SAMPLE-ARK* Capabilities ..... 41

3.3.2 Systems View Of *SAMPLE-ARK*......42

3.3.3 *SAMPLE-ARK* Operation ......43

3.3.4 Program Basics......44

3.3.4.1 Compatibility with *SAMPLE* ......44

3.3.4.2 Command Format......45

3.4 Program Commands in *SAMPLE-ARK*......45

3.4.1 Starting and Ending the Post-Exposure Bake ......46

3.4.2 Specifying the Bake Conditions......46

3.4.3 Initializing Species Concentrations......46

3.4.4 Specifying Chemical Reactions ......47

3.4.4.1 Chemical Reaction Data Structure......49

3.4.5 Specifying Diffusion ......50

3.4.5.1 Constant Diffusion Coefficient......51

3.4.5.2 Concentration-Dependent Diffusion......53

3.4.5.3 Boundary Conditions for Diffusion......54

3.4.6 Algebraic Manipulations with the DEFINE Command ......55

3.4.7 Specifying Dissolution Functions ......56

3.4.8 Running the Bake......58

3.5 Solving the System of Differential Equations ......58

3.5.1 The Numerical Algorithm ......59

3.5.2 Modifications For Diffusion......61

3.6 Summary......62

Chapter 4: Examples using *SAMPLE-ARK* ...... 70

4.1 Introduction......70

4.2 Image Reversal....70
4.2.1 Chemistry and Processing of Image Reversal Resists....70
4.2.2 Simulation of Image Reversal Resists....71
4.3 Chemical Amplification....73
4.3.1 Chemistry and Processing of Chemical Amplification Resists....74
4.3.2 Simulation of Chemical Amplification Resists....75
4.4 Silylation....76
4.4.1 Chemistry and Processing of Silylated Resists....76
4.4.1.1 Simulation of Silylated Resists....77
4.5 Summary....79
Chapter 5: Characterization and Modeling Techniques....97
5.1 Introduction....97
5.2 Exposure Characterization and Modeling....98
5.2.1 Optical Transmission Measurements....98
5.2.2 Fitting the ABC Model....101
5.2.3 FTIR Spectroscopy Measurements....102
5.2.4 Comments on the Exposure of Chemical Amplification Resists....103
5.3 Bake Characterization and Modeling....104
5.3.1 FTIR Spectroscopy....104
5.3.1.1 FTIR Measurement Techniques....105
5.3.1.2 Extracting Data from FTIR Spectra....107
5.3.2 Interferometric Measurements....108
5.3.3 Kinetic Modeling of Bake Data....109
5.3.4 Measuring the Diffusion Coefficient....110

5.4 Development Characterization and Modeling ........ 110
5.4.1 Dissolution Rate Measurements with the DRM ........ 111
5.4.2 Parameter Extraction with ***PARMEX*** ........ 111
5.5 Summary ........ 112
Chapter 6: Modeling of an Acid Hardening Resist ........ 127
6.1 Introduction ........ 127
6.2 Resist Chemistry, Preparation, and Processing ........ 129
6.3 Modeling the Exposure ........ 130
6.4 Modeling the Bake ........ 132
6.5 Modeling the Development ........ 136
6.6 Comparison of Simulation with Experimental Results ........ 139
6.7 Summary ........ 140
Chapter 7: Modeling of a T-BOC Resist ........ 154
7.1 Introduction ........ 154
7.2 Resist Chemistry, Preparation, and Processing ........ 155
7.3 Modeling the Exposure ........ 156
7.3.1 Tosylate Exposure Model ........ 158
7.3.2 Onium Salt Exposure Model ........ 160
7.4 Modeling the Bake ........ 161
7.4.1 Tosylate Bake Model ........ 163
7.4.2 Onium Salt Bake Model ........ 165
7.5 Comparison of Acid Generator Performance ........ 167
7.6 Summary ........ 168
Chapter 8: Conclusions, Comments, and Perspective ........ 182

8.1 Conclusions ........................................................................................182

8.2 Comments for Future Work..............................................................185

8.3 A Final Perspective..............................................................................187

Appendix: *SAMPLE-ARK* Program Commands.................................................. 189

# CHAPTER 1

# INTRODUCTION

## 1.1 SIMULATION OF LITHOGRAPHY

During the optical lithography step of integrated circuit (IC) manufacturing, a mask pattern comprised of dark and clear areas is transferred to a photosensitive layer on the wafer surface called a photoresist through the use of imaging optics. This pattern transfer process has become one of the most critical steps in determining both yield and cost during IC manufacturing. The need for smaller device dimensions to increase circuit speed and to reduce chip size continues to push the lithographic process well into the submicron regime. The complexity of IC's, which typically require more than ten masking levels, demands accurate and reliable pattern transfer to obtain functioning circuits at a high yield. These stringent demands necessitate a complete understanding of the lithographic process. This understanding must encompass the complex issues associated with the exposure tool, the resist material, and their interaction. However, balancing the many and complex trade-offs between lithographic processing parameters can become both time consuming and prohibitively expensive.

Simulation has become a valuable tool in IC manufacturing. Simulation of standard IC processes such as oxide growth, dopant distribution during implantation and diffusion, and metal deposition over topography continues to demonstrate the viability of simulation as a powerful, fast, and low-cost tool to the process engineer. In lithography, currently available simulation programs such as ***SAMPLE*** [1] possess the power and flexibility to evaluate and optimize a variety of lithographic processes. With the abundance of equipment, material, and environmental parameters that affect the pattern transfer process, simulation is ideally suited

for isolating and understanding the fundamental effects of individual process parameters on the final resist images obtained on the wafer.

Dill and his co-workers pioneered the field of lithography simulation with their series of ground-breaking papers in 1975 [2]-[4]. In their approach, lithography simulation, as shown in the schematic of Figure 1.1, can be broken into two basic components: simulation of the exposure tool and simulation of the resist. In order to simulate the exposure tool, the aerial image distribution obtained from the imaging optics that impinges upon the resist-coated wafer is calculated. Initial efforts in calculating the aerial image used diffraction-limited optics to determine the intensity distribution for one dimensional mask patterns on a UV stepper [4]. Since that time, other complex and diverse issues in image simulation such as defocus and partial coherence [5]-[7], aberrations [8][9], two dimension mask structures [9]-[11], and phase shift masks [12][13] have been addressed. Furthermore, non-optical tools such as e-beam [14][15], X-ray [16][17], and ion beam machines [18][19] have been successfully simulated.

Following the simulation of the exposure tool, resist simulation converts the calculated aerial image to a resist structure on the wafer which acts as a masking layer for the process steps that follow. Calculation of this resist structure typically requires simulation of two process steps: the exposure and the development† of the resist. Exposure by the illumination energy causes the resist to undergo chemical changes. The extent of these chemical changes determines the resist dissolution rate during development. Calculation of the chemical changes that occur during the exposure, and the corresponding dissolution rates during development, leads to a comprehensive model of the resist behavior for simulation.

†. The development may be a standard wet development process or a dry development process such as the oxygen plasma etch used in silylation.

In the field of resist modeling and simulation, Dill *et al.* proposed the first quantitative model for the exposure and development of a class of positive resists that use a diazonaptho-quinone as the photoactive compound, a resist technology that has dominated the IC industry since the 1960's [3]. This work still serves as a guideline for much of the effort in resist modeling to date. Chapter 2 provides a detailed historical perspective of the evolution of resist modeling and simulation since this original work.

Dill *et al.* also simulated the final resist development profiles by combining the resist model with aerial image calculations [4]. This basic approach for the complete simulation of optical lithography eventually inspired ***SAMPLE***, a simulation program for lithography and etching, developed at the University of California at Berkeley in 1977 [1]. Since that time, other programs have demonstrated success in lithography simulation [20]-[28] including programs that perform a more rigorous electromagnetic calculation that combines the optical imaging with the resist exposure to simulate specific applications such as high numerical apertures and substrate topography [29]-[31].

## 1.2 ADVANCES IN RESIST TECHNOLOGY

For many years, the diazo-type resists have remained the dominant resist technology because they have provided the IC industry with high resolution and sensitivity, good etch resistance, and relatively simple processing requirements. In addition, the chemistry of the diazo-type resists was easily adapted as the wavelength of exposure tools decreased from g-line (436 nm) to i-line (365 nm) for increased resolution. Formulations of diazo-type resists for i-line lithography now demonstrate the ability to produce linewidths down to 0.5 μm in a manufacturing environment.

As the demands on lithography continue, however, a multitude of new resist materials and processes have begun to rival the diazo-type resists for use in the submicron regime.

These new resist technologies often require a variety of sophisticated processing techniques and chemistries previously unseen with standard diazo-type resists. Some of these new processes use a modification of diazo-type chemistries to extend their limitations. For example, image reversal resists have demonstrated increased flexibility and resolution by converting the diazo-type resist tone from positive to negative [32].

As the exposure wavelength continues to decrease beyond i-line into the deep-UV (248 nm and 193 nm for example), however, the diazo-type resists become too absorbing to reproduce small features with low exposure energies. Resist materials that combine chemical amplification with more transparent resin materials have recently demonstrated high resolution in the range of 0.25 to 0.5 μm with exposure doses below 50 $mJ/cm^2$ in the deep-UV [33]-[35]. In chemical amplification, acid generated upon exposure catalyzes a reaction during the subsequent post-exposure bake. The extent of this acid catalyzed reaction determines the dissolution rate during development. Both positive and negative tone formulations have been proposed with chemistries that vary markedly from diazo-type resists.

Another resist technology, silylation [36], addresses the depth-of-focus problems associated with substrate topography and thus may be expected to produce linewidths below 0.25 μm for deep-UV exposures. The silylation process selectively introduces silicon containing compounds into the resist following exposure. This is followed by an oxygen plasma etch which creates a silicon dioxide barrier protecting the underlying resist in the silicon containing regions. Resists ranging from diazo-type resists [37] to chemical amplification resists [38] have been successfully silylated.

Because of the added complexity contained in these new resist technologies including additional process steps and new chemistries, simulation has become even more valuable in gaining a comprehensive understanding necessary for the development of an optimal resist

process. Unfortunately, current resist models and simulation tools do not have the capability and breadth to accurately predict the behavior of these new resists. More sophisticated models and extended simulation tools must be developed to keep pace with current trends in resist technology.

## 1.3 A GENERAL APPROACH TO RESIST MODELING AND SIMULATION

A complete and working resist model should accurately predict the behavior of a resist under a variety of processing conditions. Several alternative approaches can successfully accomplish this goal. The simplest method, both conceptually and in practice, consists of relating measurements of observable resist behavior to a set of processing parameters through a purely empirical expression. This resist-specific method can lead to the rapid completion of a working model, but provides little useful information about the actual mechanisms involved in determining the resist performance. With the multitude and complexity of new resists whose lithographic performance must be evaluated, this type of fundamental understanding of basic resist mechanisms has become an essential ingredient in the diagnosis, optimization, and comparison of advanced resist technologies.

In this thesis, a mechanistic approach has been used to construct a general and comprehensive methodology for the characterization, modeling, and simulation of advanced resist technologies. This methodology is described by the schematic diagram of Figure 1.2. The central aspect of this methodology is a new lithography simulator, ***SAMPLE-ARK***, which simulates the basic chemical and physical changes the resist undergoes during processing. This new program provides the capability of simulating a large class of advanced resist technologies including image reversal, chemical amplification, and silylation. A comprehensive set of characterization techniques and modeling software has also been established for monitoring the resist behavior during processing and for converting the data into mechanistic resist models for simulation in ***SAMPLE-ARK***.

The methodology has been verified through a complete modeling study for two state-of-the-art, deep-UV chemical amplification resists. Through the application of this methodology, predictive models have been developed for simulating the behavior of these resists over a variety of processing conditions. In addition, this general approach has led to a more in-depth understanding of the basic mechanisms which affect the overall performance of chemical amplification resists.

## REFERENCES


[1] W. Oldham, S. Nandgaonkar, A. Neureuther, M. O'Toole, "A General Simulator for VLSI Lithography and Etching Processes: Part I - Application to Projection Lithography," *IEEE Transactions on Electron Devices*, vol. 26, no. 4, pp. 717-722, April 1979.

[2] F. Dill, "Optical Lithography," *IEEE Transactions on Electron Devices*, vol. 22, no. 7, pp. 440-444, July 1975.

[3] F. Dill, W. Hornberger, P. Hauge, and J. Shaw, "Characterization of Positive Photoresist," *IEEE Transactions on Electron Devices*, vol. 22, no. 7, pp. 445-452, July 1975.

[4] F. Dill, A. Neureuther, J. Tuttle, and E. Walker, "Modeling Projection Printing of Positive Photoresists," *IEEE Transactions on Electron Devices*, vol. 22, no. 7, pp. 456-464, July 1975.

[5] M. Narasimham and J. Carter, "Effects of Defocus on Photolithographic Images Obtained with Projection-Printing Systems," *Proceedings SPIE: Developments in Semiconductor Microlithography III*, vol. 135, pp. 2-9, 1978.

[6] R. Hershel, "Partial Coherence in Projection Printing," *Proceedings SPIE: Developments in Semiconductor Microlithography III*, vol. 135, pp. 24-29, 1978.

[7] S. Subramanian, "Rapid Calculation of Defocused Partially Coherent Images," *Applied Optics*, vol. 20, no. 10, pp. 1854-1857, May 1981.

[8] P. Jain, A. Neureuther, and W. Oldham, "Influence of Axial Chromatic Aberration in Projection Printing," *IEEE Transactions on Electron Devices*, vol. 28, no. 11, pp. 1410-1416, November 1981.

[9] K. Toh, "Two-Dimensional Images with Effects of Lens Aberrations in Optical Lithography," *M.S. Thesis, Memorandum No. UCB/ERL M88/30*, University of California, Berkeley, May 1988.

[10] P. Flanner, S. Subramanian, and A. Neureuther, "Two-Dimensional Optical Proximity Effects," *Proceedings SPIE: Optical Microlithography V*, vol. 633, pp. 239-244, 1986.

[11] B. Lin, "Partially Coherent Imaging in Two Dimensions and Theoretical Limits of Projection Printing in Microfabrication," *IEEE Transactions on Electron Devices*, vol. ED-27, pp. 931-938, 1980.

[12] M. Prouty and A. Neureuther, "Optical Imaging with Phase Shift Masks," *Proceedings SPIE: Optical Microlithography III: Technology for the Next Decade*, vol. 470, pp. 228-232, 1984.

[13] M. Levenson, D. Goodman, S. Lindsey, P. Bayer, and H. Santini, "The Phase-Shifting Mask II: Imaging Simulations and Submicrometer Resist Exposures," *IEEE Transactions on Electron Devices*, vol. 31, no. 6, pp. 753-763, June 1984.

[14] A. Neureuther, D. Kyser, and C. Ting, "Electron-Beam Resist Edge Profile Simulation," *IEEE Transactions on Electron Devices*, vol. 26, no. 4, pp. 686-693, April 1979.

[15] K. Murata, E. Nomura, and K. Nagami, "Experimental and Theoretical Study of Cross-Sectional Profiles of Resist Patterns in Electron-Beam Lithography," J. *Vac. Sci. Technol.*, vol. 16, no. 6, pp. 1734-1738, Nov./Dec. 1979.

[16] A. Neureuther, "Simulation of X-Ray Resist Line Edge Profiles," *J. Vac. Sci. Technol.*, vol. 15, no. 3, pp. 1004-1008, May/June 1978.

[17] K. Heinrich, H. Betz, A. Heuberger, and S. Pongratz, "Computer Simulations of Resist Profiles in X-Ray Lithography," *J. Vac. Sci. Technol.*, vol. 19, no. 4, pp. 1254-1258, Nov./Dec. 1981.

[18] L. Karapiperis, I. Adesida, C. Lee, and E. Wolf, "Ion Beam Exposure Profiles in PMMA-Computer Simulation," *J. Vac. Sci. Technol.*, vol. 19, no. 4, p. 1259-1263, Nov./Dec. 1981.

[19] G. Atkinson and A. Neureuther, "Simulation of Mask Scattering Effects in Masked Ion Beam Lithography," *J. Vac. Sci. Technol. B*, vol. 3, no. 1, pp. 421-424, Jan./Feb. 1985.

[20] D. Bernard, "Optical Lithography Simulation: Introduction to SPESA," *Microelectronic Engineering*, vol. 3, p. 379, 1985.

[21] C. Mack, "PROLITH: A Comprehensive Optical Lithography Model," *Proceedings SPIE: Optical Microlithography IV*, vol. 538, pp. 207-220, 1985.

[22] C. Garza and S. Grindle, "Resist Characterization and Optimization Using a Development Simulation Computer Program, PROSIM," *Proceedings SPIE: Advances in Resist Technology and Processing III*, vol. 631, pp. 117-123, 1986.

[23] E. Barouch, B. Bradie, and S. Babu, "Three Dimensional Profile Simulation for Positive Photoresists," *Proceedings SPIE: Advances in Resist Technology and Processing VI*, vol. 1086, pp. 495-501, 1989.

[24] J. Pelka, "SOLID: Comprehensive Three Dimensional Simulation Program for Optical Microlithography," *Information Brochure, Fraunhofer-Institut fur Mikrostrukturtechnik*, May 1990.

[25] F. Jones and J. Paraszczak, "RD3D (Computer Simulation of Resist Development in Three Dimensions)," *IEEE Transactions on Electron Devices*, vol. ED-28, no. 12, pp. 1544-1552, December 1981.

[26] A. Moniwa, T. Matsuzawa, T. Ito, and H. Sunami, "A Three-Dimensional Photoresist Imaging Process Simulator for Strong Standing-Wave Effect Environment," *IEEE Transactions on Computer-Aided Design*, vol. CAD-6, no. 3, May 1987.

[27] M. Fujinaga, N. Kotani, T. Kunikiyo, H. Oda, M. Shirahata, and Y. Akasaka, "Three-Dimensional Topography Simulation Model: Etching and Lithography," *IEEE Transactions on Electron Devices*, vol. ED-37, no. 10, pp. 2183-2192, October 1990.

[28] J. Bauer, W. Mehr, U. Blaubitz, H. Baborski, N. Hasse, and J. Mueller, "Simulation and Experimental Results in 0.6 μm Lithography Using a I-Line Stepper," *Proceedings SPIE: Optical/Laser Microlithography III*, vol. 1264, pp. 431-445, 1990.

[29] M. Yeung, "Modeling High Numerical Aperture Optical Lithography," *Proceedings SPIE: Optical/Laser Microlithography*, vol. 922, pp. 149-167, 1988.

[30] H. Urbach and D. Bernard, "Modeling Latent Image Formation in Photolithography using the Helmholtz Equation," *Proceedings SPIE: Optical/Laser Microlithography III*, vol. 1264, pp. 278-293, 1990.

[31] J. Gamelin, R. Guerrieri, and A. Neureuther, "Exploration of Scattering from Topography," *J. Vac. Sci. Technol. B*, vol. 7, no. 6, pp. 1984-1990, 1989.

[32] H. Moritz, G. Paal, U. S. Patent 4, 104.070, 1978.

[33] C. Willson, H. Ito, J. Frechet, T. Tessier, and F. Houlihan, "Approaches to the Design of Radiation-Sensitive Polymeric Imaging Systems with Improved Sensitivity and Resolution," *J. Electrochem. Soc.*, vol. 133, no. 1, pp. 181-187, January 1986.

[34] J. Thackeray, G. Orsula, E. Pavelchek, D. Canistro, L. Bogan, A. Berry, and K. Graziano, "Deep UV ANR Photoresists for 248 nm Excimer Laser Photolithograhy," *Proceedings SPIE: Advances in Resist Technology and Processing VI*, vol. 1086, pp. 34-47, 1989.

[35] R. Tarascon, E. Reichmanis, F. Houlihan, A. Shugard, and L. Thompson, "Poly(t-BOC-styrene sulfone)-Based Chemically Amplified Resists for Deep-UV Lithography," *Polymer Engineering and Science*, vol. 29, no. 13, pp. 850-855, Mid July, 1989.

[36] G. Taylor, L. Stillwagon, and T. Venkatesan, "Gas-Phase Functionalized Plasma-Developed Resists: Initial Concepts and Results for Electron-Beam Exposure," *J. Electrochem. Soc.*, vol. 131, p. 1658, 1984.

[37] F. Coopmans and B. Roland, "DESIRE: A Novel Dry Developed Resist System," *Proceedings SPIE: Advances in Resist Technology and Processing III*, vol. 631, pp. 34-39, 1986.

[38] S. MacDonald, H. Ito, H. Huraoka, and C. Willson, "A New Oxygen Plasma-Developable UV-Sensitive Resist," *SPE Proceedings Tech. Conf. Photopolymers - Principles, Processes, and Materials*, p. 177, 1985.

**Figure 1.1:** Schematic of optical lithography simulation.

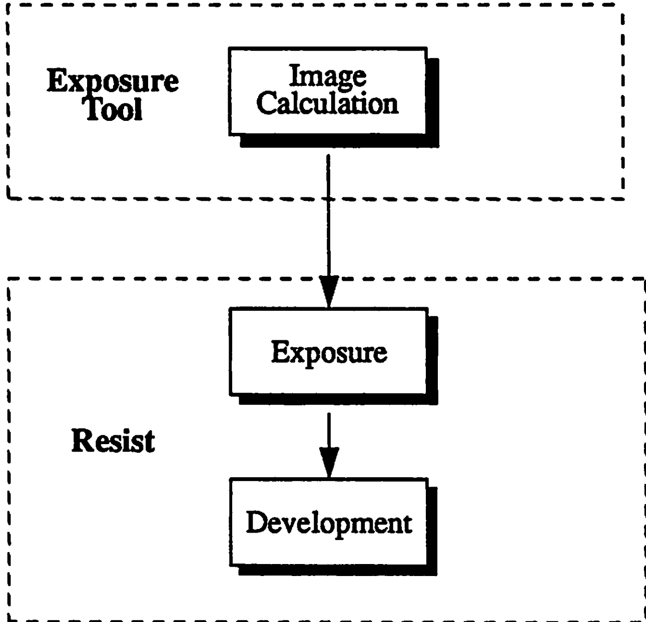

**Figure 1.2:** A general framework for the characterization, modeling, and simulation of advanced resist processes.

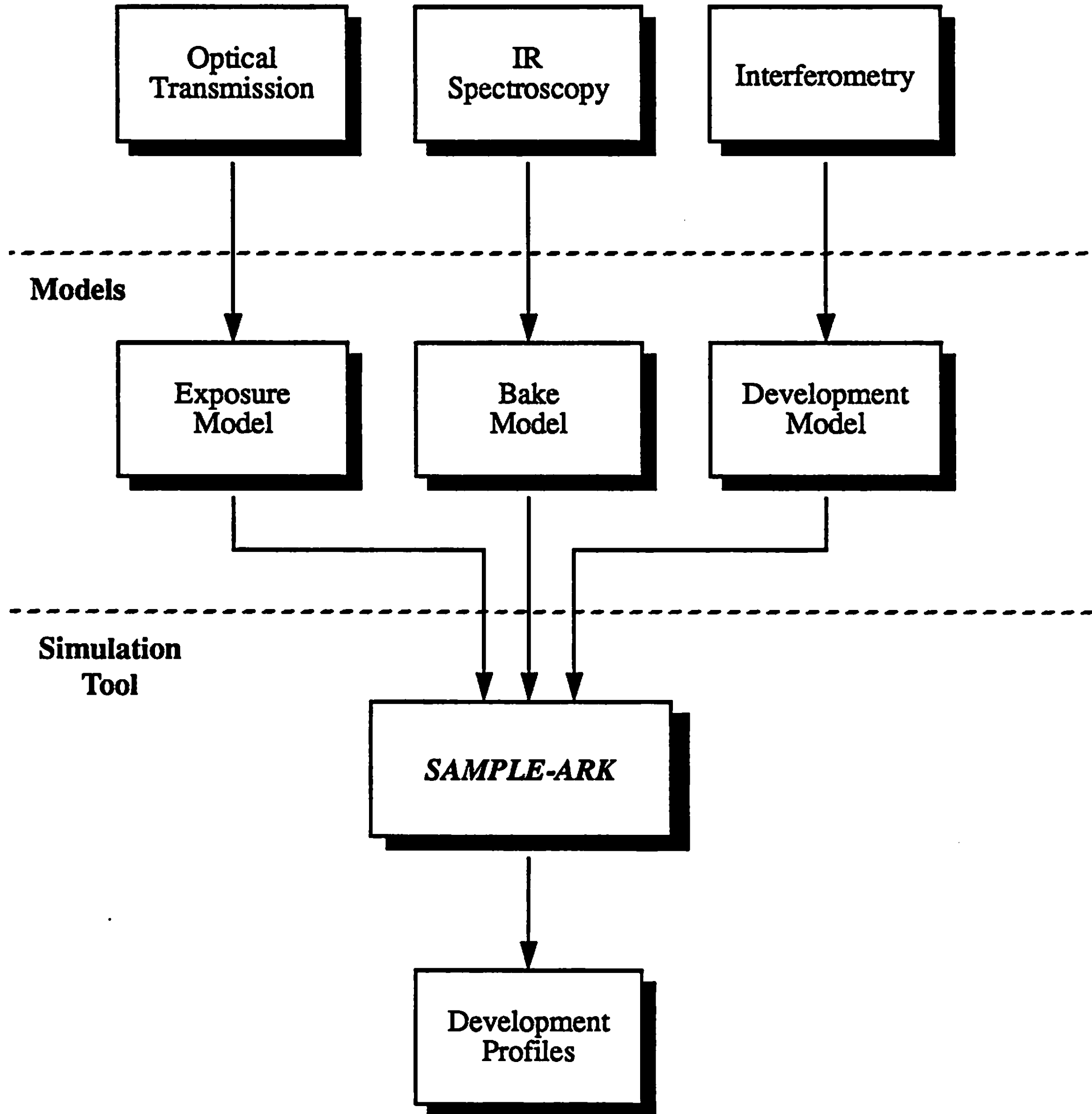

# CHAPTER 2

# EVOLUTION OF RESIST MODELING AND SIMULATION

Modeling and simulation can provide both an accurate prediction of resist behavior as well as valuable information concerning the fundamental mechanisms that affect the resist performance. Initial models described the behavior of diazo-type resists. Recently, complex kinetic models have been proposed for more advanced resist technologies such as image reversal, chemical amplification, and silylation. Simulation programs provide an interface to these mathematical models and have proven to be a valuable tool in the evaluation and optimization of a variety of resist technologies. This chapter presents the evolution of resist modeling and simulation from its initial beginnings to its current state. This evolutionary process has led to the development of a general methodology for the characterization, modeling, and simulation of advanced resist technologies.

## 2.1 MODELS FOR DIAZO-TYPE RESISTS

Diazo-type resists have been the mainstay of the photolithography field since the 1960's. Exposure of the resist to UV wavelengths in the range of 350 to 450 nm produces a positive tone image of the mask pattern. The diazo-type resists have achieved success as a result of good resolution and high etch resistance for use with g-line (436 nm) photolithography. Recently, tuning of the resist chemistry has produced high-resolution i-line resists that are capable of replicating feature sizes down to 0.5 μm. Most of the effort in resist modeling and simulation to date has concentrated on this positive resist technology.

### 2.1.1 Overview of Diazo-type Resist Chemistry

The diazo-type resists are composed of two essential components: a base resin and a photoactive compound (PAC). The resin is typically a low molecular weight novolac polymer whose structure is shown in Figure 2.1. The novolac resin alone dissolves readily in aqueous alkaline developers such as KOH. However, the photoactive compound, a diazonapthoquinone, acts as a dissolution inhibitor. Combining the PAC with the resin in sufficient quantities can substantially reduce the dissolution rate.

The PAC is sensitized to UV radiation, and will undergo a transition from the diazonapthoquinone to indene carboxylic acid (ICA) with the evolution of nitrogen gas as a side product. This photolytic reaction is shown in Figure 2.2. Once the PAC has been destroyed through exposure, the resist become soluble once again in the developer. Consequently, as a result of the dissolution-inhibition properties of the PAC, the resist develops from the wafer where exposed (in the clear regions of the mask), and thus acts as a positive resist. The ratio between development rates in the exposed and unexposed regions of the resist can be as high as a factor of about of $10^4$.

### 2.1.2 Modeling the Exposure

Dill and his co-workers proposed a model for the exposure of diazo-type resists in terms of the illumination intensity and the PAC concentration within the resist [1]. In this model, the intensity distribution for an optically matched substrate is given by:

$$\frac{\partial I(z,t)}{\partial z} = -I(z,t)\,[AM(z,t) + B] \qquad [2.1]$$

where I is the illumination intensity, M is the normalized concentration of PAC, z is the depth into the resist, and t is the exposure time. The destruction of PAC is described by:

$$\frac{\partial M(z,t)}{\partial t} = -I(z,t)\,M(z,t)\,C \qquad [2.2]$$

The A, B, and C parameters of equations [2.1] and [2.2] depend on the particular resist being used† and are typically referred to as Dill's ABC parameters.

Equation [2.1] has its origin in the Lambert-Beer Law in which the rate of change of the intensity is proportional to the intensity itself through an absorption coefficient, $\alpha$. The resist, in the Dill model, has an absorption coefficient that depends linearly on the PAC concentration such that $\alpha = AM + B$. Before exposure (M = 1), the absorption coefficient is given by $\alpha = A + B$, while when the resist is fully exposed (M = 0), the absorption coefficient becomes $\alpha = B$. For the positive values of A obtained for diazo-type resists, the absorption coefficient decreases with increasing exposure causing the resist to *bleach*. For this reason, A and B are typically referred to as the bleachable and nonbleachable parts of the absorption coefficient. The photolytic conversion of the PAC to ICA produces this bleaching phenomenon.

Equation [2.2] describes the rate of PAC destruction and has its basis in the kinetics of photolytic reactions. In this equation, the rate of PAC destruction is proportional to both the concentration of PAC as well as the illumination intensity through a rate coefficient, C, typically referred to as the bleach rate. The inverse of the C parameter provides information about the photo-speed of the reaction. Typically, C is greater than 0.01 $cm^2/mJ$ for diazo-type resists resulting in sensitivities less than 100 $mJ/cm^2$.

---

†. These parameters also depend on the pre-exposure bake treatment.

The change in the absorption coefficient due to the PAC destruction affects the resist transmission during exposure. From equations [2.1] and [2.2], the transmission of the resist on a matched substrate is given by:

$$T(t) = exp\left[-\int_0^d \{AM(z,t) + B\}\, dz\right] \quad [2.3]$$

where d is the thickness of the resist film. This change in transmission provides a practical method for extracting the ABC parameters. Chapter 5 describes in detail the procedure involved in monitoring the resist transmission and the subsequent determination of the ABC parameters from the results.

Figure 2.3 shows the simulated transmission of KTI 820 resist on a matched substrate using A = 0.49 $\mu m^{-1}$, B = 0.031 $\mu m^{-1}$, C = 0.0125 $cm^2/mJ$ and a film thickness of 1 $\mu m$. The bleaching of the resist is clearly demonstrated in this plot by the exponential increase in the transmission with increasing exposure doses.

The Dill model has also been used to describe the exposure for several variations to the standard diazo-type resist process. The addition of an absorbing dye to reduce standing wave effects has been modeled as an increase in the nonbleachable absorption parameter, B [2][3]. Shacham-Diamand used a second set of ABC parameters to describe the observed darkening reaction in the novolac resin when diazo-type resists are exposed at 248 nm [4].

### 2.1.3 Modeling the Post-Exposure Bake

The use of a bake step following the exposure of diazo-type resists tends to reduce unwanted standing wave effects that result from substrate reflections and thus results in enhanced process latitude [5]. It has been theorized that this post-exposure bake diffuses the PAC within the resist [5][6]. Consequently, several methods have demonstrated success in

modeling this post-exposure bake effect as a diffusion-controlled redistribution of the PAC following the exposure [7][8].

### 2.1.4 Modeling the Development

The chemistry of the resist dissolution process is a more complex problem to address. The rate of dissolution depends on many factors including the structure and molecular weight of the novalac resin, the PAC and ICA concentration, and the concentration and type of cations and anions in the developer. During the dissolution process, the developer penetrates the resist surface, reacts with the novolac resin, and finally removes the reacted molecules into the developer solution [9]. The PAC acts to inhibit this dissolution process. For diazo-type resists, the rate of dissolution is determined by the events near the surface of the resist only.† With sufficient developer flow, the developer concentration near the resist surface remains constant, and the dissolution rate depends primarily on the PAC concentration for a given developer solution.

Even with the above assumptions, the development process is extremely complex and not well understood. Therefore, many proposed dissolution models simply relate the dissolution rate to the PAC concentration through empirical or semi-empirical functions. Dill *et al.* first proposed such an approach for modeling resist dissolution in conjunction with the ABC exposure model [1]. They found a good fit to the experimental data occurred using an expression given by:

$$\text{Rate}\ (M) = \exp\left(E_1 + E_2 M + E_3 M^2\right) \qquad [2.4]$$

where M is the normalized concentration of PAC and $E_1$, $E_2$, and $E_3$ are the model fitting parameters.

†. For some negative resists, the dissolution rate is controlled by the rate of gel formation as the solvent penetrates the resist.

Kim *et al.* also suggested a development model relating the dissolution rate to the PAC concentration [10]. In addition, they also observed that, for some resists, the dissolution rate slowed considerably at the initial resist surface when compared with the bulk. They proposed a depth-dependent expression with six fitting parameters to account for this surface inhibition phenomenon. In this model, the dissolution rate in the bulk of the resist is given by:

$$R(M) = \left[ \frac{1 - (M \cdot e^{-R_3(1-M)})}{R_1} + \frac{M \cdot e^{-R_3(1-M)}}{R_2} \right]^{-1} \qquad [2.5]$$

where R is the dissolution rate in the bulk and $R_1$, $R_2$, and $R_3$ are three of the model fitting parameters.

The surface inhibition effect was incorporated in the model through a multiplicative term which decays exponentially with depth into the resist. As a result, the complete dissolution rate expression as a function of depth and PAC concentration is given by:

$$\text{Rate}(z, M) = R(M) \{ 1 - [1 - (R_5 - (R_5 - R_6) M) ] \, exp(-z/R_4) \} \qquad [2.6]$$

where z is the depth into the resist, $R_4$ is the characteristic depth of the surface inhibition effect, and $R_5$ and $R_6$ are the ratio of the surface dissolution rate to the bulk dissolution rate for the fully exposed and unexposed resist, respectively.

Figure 2.4 shows the fit of the Kim model to experimental dissolution rate data for KTI 820 resist obtained through interferometric measurements with the Perkin-Elmer Development Rate Monitor (DRM) [11]. The two curves in Figure 2.4 correspond to the dissolution rate in the bulk ($z \gg R_4$) and at the surface of the resist ($z = 0$) using equation [2.6]. The best fit to the data occurred with $R_1 = 0.1143$ μm/sec, $R_2 = 0.001683$ μm/sec, $R_3 = 4.667$, $R_4 = 0.10$ μm, $R_5 = 0.45$, and $R_6 = 0.30$.

Alternative approaches based more heavily on development mechanisms and dissolution kinetics have also achieved some success in describing the resist dissolution process. Quantitative models for use in simulation have resulted from the derivation of alternative semi-empirical or mechanistic functions relating dissolution rate to PAC concentration [12]-[15], the application of percolation theory to dissolution simulation [16][17], the examination of developer effects on the dissolution [18][19], and the study of the exposure and dissolution mechanisms for polyfunctional PAC inhibitor molecules [20]. In addition, other contributions have extended the understanding of the kinetics of novolac resin dissolution and PAC inhibition [21]-[30]. The variety and breadth presented by this substantial collection of research clearly demonstrates the complex nature of resist dissolution. Further work is still required to extend this knowledge into a complete and quantitative model that accurately describes observed dissolution phenomena for use with simulation programs.

## 2.2 MODELS FOR ADVANCED RESIST TECHNOLOGIES

While the majority of modeling efforts have concentrated on the diazo-type resists, several advanced resist technologies such as image reversal, chemical amplification, and silylation have recently begun to receive considerable attention. All of these technologies require additional post-exposure processing, referred to simply as a post-exposure bake, which must be accounted for in any modeling scheme. Recent modeling approaches for these technologies have tended to stress the fundamental mechanisms that determine the resist behavior and have used a variety of characterization techniques ranging from single performance parameter measurements to the individual characterization of each process step.

### 2.2.1 Models for Image Reversal

In one type of image reversal process [31], the use of an additional post-exposure bake and flood exposure converts the tone of diazo-type resists from positive to negative (see Chapter 4 for details). Klose *et al.* modeled the kinetics of the post-exposure bake and flood exposure using characteristic curve measurements of resist thickness versus exposure dose and proposed an analytical model relating the resist line-edge slope to various resist properties and processing parameters [32]. The model accurately predicted the patterning and flood exposure conditions under which the resist line-edge slope would change from negative to positive. Ziger and Mack assumed simplified kinetics during the post-exposure bake and flood exposure to simulate the latent image of inhibitor concentration within the resist [33]. Using this model, they demonstrated that overexposure in image reversal processes leads to resolution enhancement through an increased slope in the latent image at the mask edge. Visser *et al.* used a new program called ***SLIM*** to simulate the latent image for an image reversal process and to search for the optimal flood exposure dose [34]. This program was also used to simulate several other advanced technologies including built-in mask and image reversal with two image-wise exposures.

### 2.2.2 Models for Chemical Amplification

Chemical amplification resists use an acid catalyzed reaction during the post-exposure bake to achieve high sensitivities. Various resist chemistries have produced both positive and negative tone resists with chemical amplification (see Chapters 6 and 7).

Several kinetic studies have been performed on one such resist for the deep-UV, Shipley SNR 248 acid hardening resist [35]. Using measurements of characteristic curves and resist sensitivity for an early version of SNR 248, Seligson *et al.* demonstrated that a reciprocity existed between the exposure dose, the bake temperature, and the bake time and expressed

this reciprocity mathematically as an "effective dose" [36]. Fukuda and Okazaki performed dissolution rate measurements [38] while Ziger *et al.* used measurements of the characteristic curve [39] in order to model the kinetics of the crosslinking reaction and to generate quantitative models for use with simulation.

Chemical amplification resists are not designed exclusively for the deep-UV. For an X-ray resist with chemical amplification, Dammel *et al.* derived a kinetic model for the acid catalyzed destruction of a dissolution inhibitor based on UV spectroscopy measurements during the exposure/bake step [40]. Barouch *et al.* developed a complete model for the simulation of an i-line acid hardening resist [41].

### 2.2.3 Models for Silylation

Silylation processes take advantage of the selective incorporation of silicon into a shallow layer at the resist surface to obtain a large depth-of-focus with little or no sensitivity to substrate topography (see Chapter 4 for details). Reuhman-Huisken *et al.* used resist swelling and RBS measurements to model the silicon uptake and then combined this result with etch rate experiments to simulate the final resist images obtained using the DESIRE process [42]. Bauch *et al.* also developed a quantitative model for the simulation of DESIRE including a mathematical description of the silylating agent diffusion coefficient and its dependence on PAC concentration [43].

## 2.3 RESIST SIMULATION

Simulation programs provide a convenient interface between the user of the program and the mathematical models that describe the resist behavior. Several programs have been written for the simulation of optical lithography (see Chapter 1). The following section demonstrates the use of lithography simulation through the description of one such program, *SAMPLE*.

### 2.3.1 Simulation with *SAMPLE*

Since its conception in 1977 at the University of California at Berkeley, the *SAMPLE* program (*S*imulation *A*nd *M*odelling of *P*rofiles in *L*ithography and *E*tching) [44] has provided a powerful tool for IC manufacturing. The scope of the program has grown to include a wide range of IC processes such as optical, e-beam, x-ray, and ion beam lithography, wet and dry etching, and deposition of metals and insulators [7]. In optical lithography, *SAMPLE* presents a low-cost aid for the in-depth analysis, evaluation, and optimization of diazo-type resist processes.

The Dill model of equations [2.1] and [2.2] provides the basis for the numerical algorithm that simulates resist exposure in *SAMPLE*. The program first divides the resist film into a number of homogeneous vertical layers. The configuration of the resist film for the exposure algorithm is shown in Figure 2.5. Each layer is defined by an average PAC concentration, and thus an absorption coefficient, $\alpha_i(t) = AM_i(t) + B$. A rigorous routine for thin-film stack computations by Berning calculates the average intensity in each layer for each incremental time step [45]. The PAC concentration in each layer is then updated using the kinetic expression of equation [2.2]. The calculation of the normalized PAC concentration, M, for a given time step is given by:

$$M_i(t + \Delta t) = M_i exp[-CI_i(t)\Delta t] \qquad [2.7]$$

This routine is repeated until the appropriate exposure dose is obtained. Figure 2.6 shows a simulation of constant PAC contours in KTI 820 resist following exposure for a line-space grating pattern with a 2.6 μm pitch using the ABC parameters given in section 2.1.2.

Simulation of the development step follows the exposure. First, the local PAC concentration is converted to a dissolution rate at each point in the resist using one of the development models of Section 2.1.4. *SAMPLE* implements both the Dill model of equation

[2.4] as well as the Kim model of equation [2.6]. A routine called the string algorithm advances the resist surface during development [46]. A pictorial description of the string algorithm is shown in Figure 2.7. In this routine, the surface of the resist is delineated by a string of points with interconnecting segments. During each time step of the numerical algorithm, the segments on the string advance by an amount determined by the dissolution rate at that point in a direction perpendicular to the surface. Delooping routines remove the non-physical looping of segments that occur with this type of surface motion algorithm when the string moves through regions of non-uniform dissolution rates.

Combining the simulations of the aerial image, the exposure, and the development produces two-dimensional resist development profiles in ***SAMPLE***. Simulated development profiles for KTI 820 resist using the Kim development model with the R parameters given in section 2.1.4 are shown in Figure 2.8 for a line-space grating pattern with a 2.6 μm pitch. Profiles are shown for three cases: best exposure and focus, 22% underexposure, and best exposure with 3 μm of defocus. These simulations correspond to the three SEM pictures shown in Figure 2.9. The excellent correlation obtained between the simulation and the experimental results provides a good example of the successful application of lithography simulation using accurate, quantitative resist models.

## 2.4 A GENERAL MODELING AND SIMULATION METHODOLOGY

A comparison between the advances in resist technology discussed in Chapter 1 and the current trends in the modeling and simulation of these technologies provides a valuable perspective for future directions. The use of more complex resist materials and processes to address problematic areas of optical lithography has made the development of accurate resist models much more difficult. Because of the additional complexity associated with new technologies, modeling trends have moved towards more mechanistic approaches in order to gain a better understanding of the factors that affect the resist behavior. While a variety of

experimental methods have been used for obtaining quantitative data, resist characterization, in general, has tended to emphasize the use of single-step data collection techniques in which overall performance parameters such as the sensitivity and contrast are measured. Complete resist models describing the entire process are then backed out from the final experimental results. While this approach provides a rapid method for quantifying resist behavior and for understanding the effects of various process parameters on resist performance, it can sometimes lead to oversimplified models without direct verification of the actual changes occurring within the resist during each process step. Therefore, the work present here emphasizes the use of characterization techniques for separately monitoring each individual process step.

Many aspects of current modeling and simulation techniques extend to more complex resist technologies while other aspects require further generalization. Figure 2.10 presents a general methodology for the characterization, modeling, and simulation of advanced resist technologies which builds upon the established methods for diazo-type resists. The foundation of this methodology, the ***SAMPLE-ARK*** simulation tool, combines mechanistic resist models describing each process step for the simulation of resist line-edge profiles. In general, the modeling approach and characterization techniques for diazo-type resists are extendable to the exposure and development of more advanced resist technologies. The difficulty for these technologies lies in the characterization and the modeling of the fundamental changes that occur during the post-exposure bake. FTIR spectroscopy provides the capability of monitoring specific chemical bonds within the resist as the bake progresses. As a result, this technique can be applied to the characterization of a wide range of advanced resist technologies. Once the bake has been characterized, kinetic models can be fit to the experimental results. The following chapters describe in detail the extension of current

characterization, modeling, and simulation techniques for the implementation of this new methodology.

## REFERENCES


[1] F. Dill, W. Hornberger, P. Hauge, J. Shaw, "Characterization of Positive Photoresist," *IEEE Transactions on Electron Devices*, vol. ED-22, no. 7, pp. 445-452, July 1975.

[2] M. Cagan, M. Blanco, V. Wise, P. Trefonas, B. Daniels, and C. McCants, "A Lithographic Study of Photoresists Containing a Base Soluble Dye," *Proceedings SPIE: Advances in Resist Technology and Processing VI*, vol. 1086, pp. 515-534, 1989.

[3] C. Mack, "Dispelling the Myths about Dyed Photoresist," *Solid State Technology*, vol. 31, no. 1, pp. 125-130, 1988.

[4] Y. Shacham-Diamand, "Modeling of Novolak-Based Positive Photoresist Exposed to KrF Excimer Laser UV Radiation at 248 nm," *IEEE Transactions on Semiconductor Manufacturing*, vol. 3, no. 1, pp. 37-44, May 1990.

[5] E. Walker, "Reduction of Photoresist Standing-Wave Effects by Post-Exposure Bake," *IEEE Transactions on Electron Devices*, vol. ED-22, no. 7, p. 464, July 1975.

[6] P. Trefonas, B. Daniels, M. Eller, and A. Zampini, "Examination of the Mechanism of the Post Exposure Bake Effect," *Proceedings SPIE: Advances in Resist Technology and Processing V*, vol. 920, pp. 203-211, 1988.

[7] *SAMPLE 1.7a User's Guide,* Department of Electrical Engineering and Computer Sciences, University of California, Berkeley, CA, 1989.

[8] D. Bernard, "Simulation of Post-Exposure Bake Effects on Photolithographic Performance of a Resist Film," *Philips Journal of Research,* vol. 42, no. 5/6, pp. 566-582, 1987.

[9] A. Reiser, *Photoreactive Polymers - The Science and Technology of Resists*, John Wiley and Sons, Inc., pp. 215-216, 1989.

[10] D. Kim, W. Oldham, and A. Neureuther, "Development of Positive Photoresist," *IEEE Transactions on Electron Devices*, vol. ED-31, pp. 1730-1735, December 1984.

[11] A. McCullough and S. Grindle, "Resist Characterization Using a Multichannel Development Rate Monitor," *Proceedings Sixth International Technical Conference on Photopolymers*, Ellenville, New York, 1982.

[12] Y. Hirai, M. Sasago, M. Endo, K. Tsuji, Y. Mano, "Process Modeling for Photoresist Development and Design of DLR/SD (Double-Layer Resist by a Single Development) Process," *IEEE Transactions on Computer-Aided Design*, vol. CAD-6, no. 3, pp. 403-409, May 1987.

[13] C. A. Mack, "Development of Positive Photoresists," *Journal of Electro-Chemical Society*, vol. 134, no. 1, pp. 148-152, 1987.

[14] T. Ohfuji, K. Yamanaka, and M. Sakamoto, "Characterization and Modeling of High Resolution Positive Photoresists," *Proceedings SPIE: Advances in Resist Technology and Processing V, vol. 920*, pp. 190-197, 1988.

[15] C. Garza and C. Szmanda, "Resist Dissolution Kinetics and Submicron Process Control," *Proc. Proceedings SPIE: Advances in Resist Technology and Processing V*, vol. 920, pp. 321-338, 1988.

[16] A. Bogdanov, A. Polyakov, K. Valiev, L. Velikov, and D. Zaroslov, "Computer Simulation of the Percolational Development and Pattern Formation in Pulsed Laser Exposed Positive Photoresists," *Proceedings SPIE: Advances in Resist Technology and Processing IV*, vol. 771, pp. 167-172, 1987.

[17] P. Trefonas, "Positive Photoresist Development: A Multiple State Percolation Model," *Proceedings SPIE: Advances in Resist Technology and Processing VI*, vol. 1086, pp. 484-494, 1989.

[18] W. Hinsberg and M. Gutierrez, "Effect of Developer Composition on Photoresist Performance," *Proceedings SPIE: Advances in Resist Technology*, vol. 469, pp. 57-64, 1984.

[19] C. Zee, W. Bell, and A. Neureuther, "Effect of Developer Type and Agitation on Dissolution of Positive Photoresist," *Proceedings SPIE: Advances in Resist Technology and Processing V*, vol. 920, pp. 154-161, 1988.

[20] P. Trefonas and B. Daniels, "New Principle for Image Enhancement in Single Layer Positive Photoresists," *Proceedings SPIE: Advances in Resist Technology and Processing IV*, vol. 771, pp. 194-210, 1987.

[21] M. Templeton, C. Szmanda, and A. Zampini, "On the Dissolution Kinetics of Positive Photoresists: The Secondary Structure Model," *Proceedings SPIE: Advances in Resist Technology and Processing IV*, vol. 771, pp. 136-147, 1987.

[22] L. Blum, M. Perkins, and A. McCullough, "A Study of the Dissolution Kinetics of a Positive Photoresist using Organic Acids to Simulate Exposed Photoactive Compounds," *Proceedings SPIE: Advances in Resist Technology and Processing IV*, vol. 771, pp. 148-159, 1987.

[23] M. Hanabata, A. Furuta, Y. Uemura, "Novolak Design for High Resolution Positive Photoresists," *Proceedings SPIE: Advances in Resist Technology and Processing IV*, vol. 771, pp. 85-92, 1987.

[24] M. Hanabata, Y. Uetani, and A. Furuta, "Novolak Design for High Resolution Positive Photoresists (II): Stone Wall Model for Positive Photoresist Development," *Proceedings SPIE: Advances in Resist Technology and Processing V*, vol. 920, pp. 349-354, 1988.

[25] M. Murata, M. Koshiba, and Y. Harita, "Mechanisms of the Dissolution Inhibition Effect and Their Application to Designing Novel Deep-UV Resists," *Proceedings SPIE: Advances in Resist Technology and Processing VI*, vol. 1086, pp. 48-55, 1989.

[26] C. Szmanda, A. Zampini, D. Madoux, and C. McCants, "Photoactive Compound Structure and Resist Function: The Influence of Chromophore Proximity," *Proceedings SPIE: Advances in Resist Technology and Processing VI*, vol. 1086, pp. 363-373, 1989.

[27] J. Huang, T. Kwei, and A. Reiser, "On the Molecular Mechanism of Positive Novolac Resists," *Proceedings SPIE: Advances in Resist Technology and Processing VI*, vol. 1086, pp. 74-84, 1989.

[28] K. Honda, B. Beauchemin, R. Hurditch, and A. Blakeney, "Studies of the Molecular Mechanism of Dissolution Inhibition of Positive Photoresist Based on Novolak-DNQ," *Proceedings SPIE: Advances in Resist Technology and Processing VII*, vol. 1262, pp. 493-500.

[29] A. Zampini, P. Turci, G. Cernigliaro, H. Sandford, G. Swanson, C. Meister, and R. Sinta, "High Resolution Positive Photoresists: Novolak Molecular Weight and Molecular Weight Distribution Effects," *Proceedings SPIE: Advances in Resist Technology and Processing VII*, vol. 1262, pp. 501-512, 1990.

[30] R. A. Arcus, "A Membrane Model for Positive Photoresist Development," *Proceedings SPIE: Advances in Resist Technology and Processing III*, vol. 631, p. 124-134, 1986.

[31] H. Moritz, G. Paal, U. S. Patent 4, 104.070, 1978.

[32] H. Klose, R. Sigush, W. Arden, "Image Reversal of Positive Photoresist: Characterization and Modeling," *IEEE Transactions on Electron Devices*, vol. ED-32, no. 9, pp. 1654-1661, September 1985.

[33] D. Ziger and C. Mack, "Lithographic Characterization of a Rapid Ammonia Catalyzed Image Reversal Process," *KTI Microelectronics Seminar - Interface '88*, pp. 165-175, November 1988.

[34] R. Visser, H. Urbach, A. Tol, H. Eggink, and E. Kemna, "Simulation of Latent Image Manipulation - A Versatile Simulation Program for New Photolithographic Systems," *Proceedings SPIE: Advances in Resist Technology and Processing VI*, vol 1086, pp. 605-614, 1989.

[35] J. W. Thackeray, G. W. Orsula, E. K. Pavelchek, D. Canistro, L. E. Bogan, A. K. Berry, K. A. Graziano, "Deep UV ANR Photoresists for 248 nm Excimer Laser Photolithograhy," *Proceedings SPIE: Advances in Resist Technology and Processing VI*, vol. 1086, pp. 34-47, 1989.

[36] D. Seligson, S. Das, H. Gaw, "Process Control with Chemical Amplification Resists Using Deep Ultraviolet and X-Ray Radiation," *J. Vac. Sci. Technol. B*, vol. 6, no. 6, pp. 2303-2307, November/December 1988.

[37] S. Das, J. Thackeray, M. Endo, J. Langston, and H. Gaw, "A Systematic Investigation of the Photoresponse and Dissolution Characteristics of an Acid Hardening Resist," *Proceedings SPIE: Advances in Resist Technology and Processing VII*, vol. 1262, pp. 60-71, 1990.

[38] H. Fukuda, S. Okazaki, "Kinetic Model and Simulation for Chemical Amplification Resists," *J. Electrochem. Soc.*, vol. 137, no. 2, pp. 675-679, February 1990.

[39] D. Ziger, C. Mack, and R. Distasio, "The Generalized Characteristic Model for Lithography: Application to Negatively Chemically Amplified Resists," *Proceedings SPIE: Advances in Resist Technology and Processing VIII*, vol. 1466, 1991.

[40] R. Dammel, K. F. Dossel, J. Lingnau, J. Theis, H. L. Huber, H. Oertel, "Photocatalytic Novolak-Based Positive Resist for X-Ray Lithography - Kinetics and Simulation," *Microelectronic Engineering*, vol. 6, pp. 502-509, 1987.

[41] E. Barouch, U. Hollerbach, S. Orszag, M. Allen, and G. Calabrese, "Simulation of Advanced Negative I-line Photoresist," *Optical/Laser Microlithography IV*, vol. 1463, 1991.

[42] M. Reuhman-Huisken, A. Tol, R. Visser, J. Dijkstra, and J. O'Neil, "The Formation of Latent Images and Resist Profiles in the DESIRE Process," *Proceedings SPIE: Advances in Resist Technology and Processing VII*, vol. 1262, pp. 401-411, 1990.

[43] L. Bauch, U. Jagdhold, H. Dreger, J. Bauer, W. Hoppner, and J. Erzgraber, "Surface Imaging on the Basis of Phenolic Resin - Experiments and Simulation," *Proceedings SPIE: Advances in Resist Technology and Processing VIII*, vol. 1466, 1991.

[44] W. Oldham, S. Nandgaonkar, A. Neureuther, and M. O'Toole, "A General Simulator for VLSI Lithography and Etching Processes: Part I - Application to Projection Lithography," *IEEE Transactions on Electron Devices*, vol. 26, no. 4, pp. 717-722, April 1979.

[45] P. Berning, "Theory and Calculations of Optical Thin Films," *Physics of Thin Films*, vol. I, ed. G. Hass, Wiley, New York, 1962.

[46] R. Jewett, P. Hagouel, A. Neureuther, and T. Van Duzer, "Line-Profile Resist Development Simulation Techniques," *Polymer Eng. Sci.*, vol. 17, no. 6, pp. 381-384, June 1977.

[47] A. Neureuther, W. Oldham, B. Huynh, K. Toh, R. Ferguson, W. Haller, and D. Sutija, "Test Patterns and Simulation Software for Characterization of Optical Projection Printing," *KTI Microelectronics Seminar - Interface '88*, pp. 113-122, November 1988.

**Figure 2.1:** Chemical structure of the novolac resin used in diazo-type resists

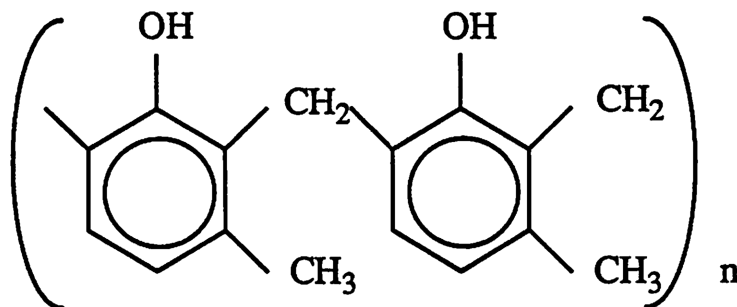


**Figure 2.2:** The photolytic reaction in diazo-type resists converting the photoactive compound (PAC) to indene carboxylic acid (ICA)

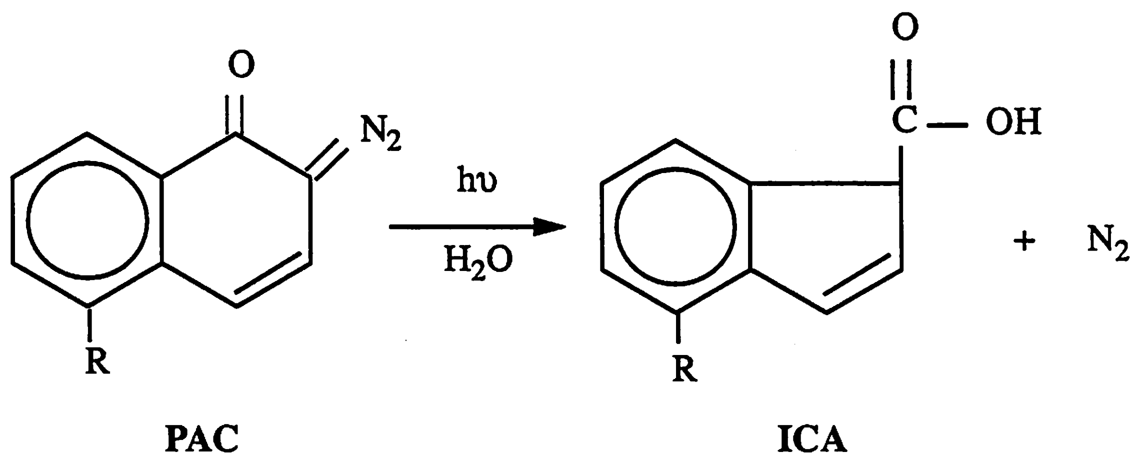

**Figure 2.3:** Simulated transmission characteristic of KTI 820 resist with a film thickness of 1 μm and A = 0.49 $\mu m^{-1}$, B = 0.031 $\mu m^{-1}$, and C = 0.0125 $cm^2/mJ$.

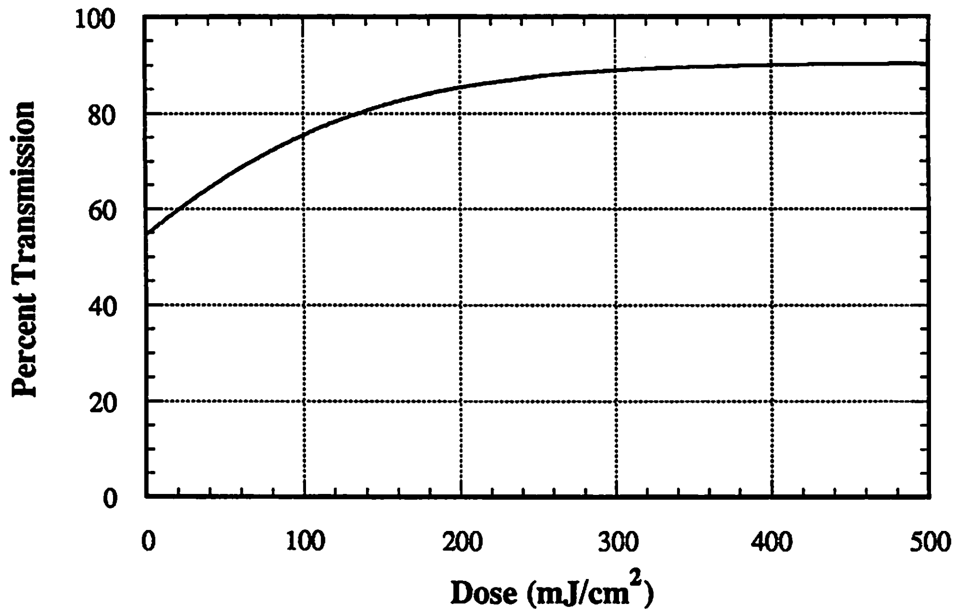


**Figure 2.4:** Comparison of the Kim model with experimental measurements of dissolution rate versus PAC concentration for KTI 820 resist.

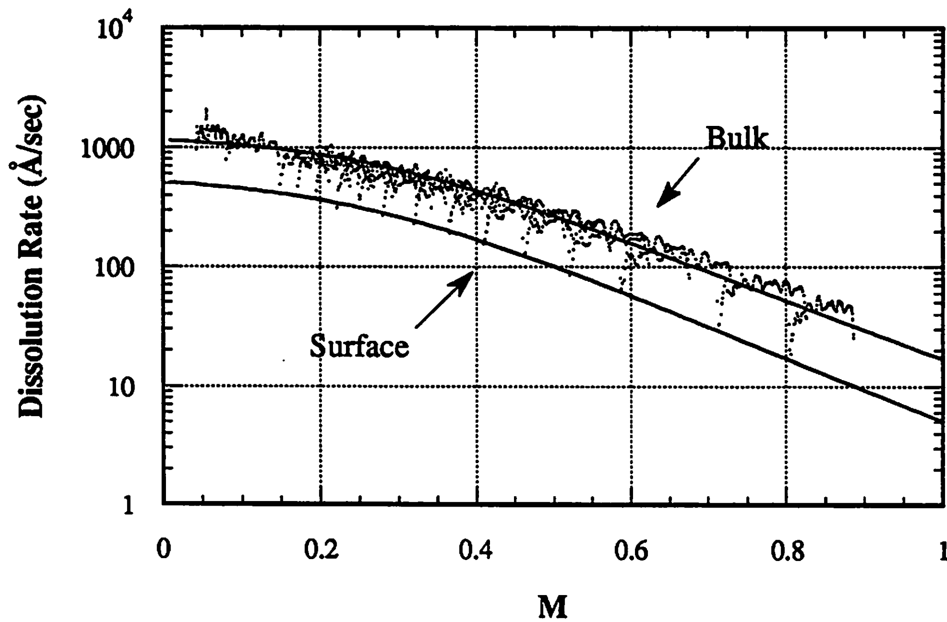

**Figure 2.5:** Configuration of the $i^{th}$ layer in the resist film at time, t, in the *SAMPLE* exposure algorithm.

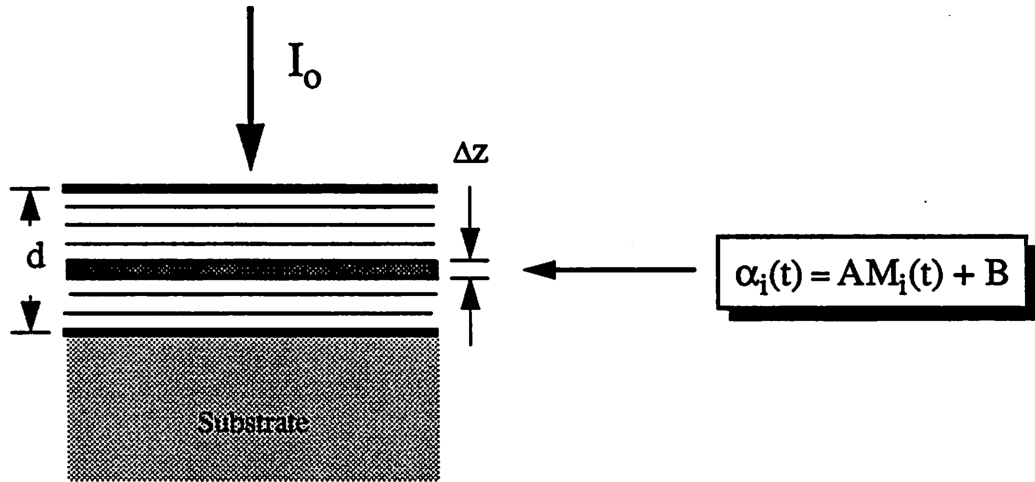


**Figure 2.6:** Contours of constant PAC concentration in KTI 820 resist for a 99 mJ/cm$^2$ exposure dose. The mask pattern is a line-space grating with a 2.6 μm pitch.

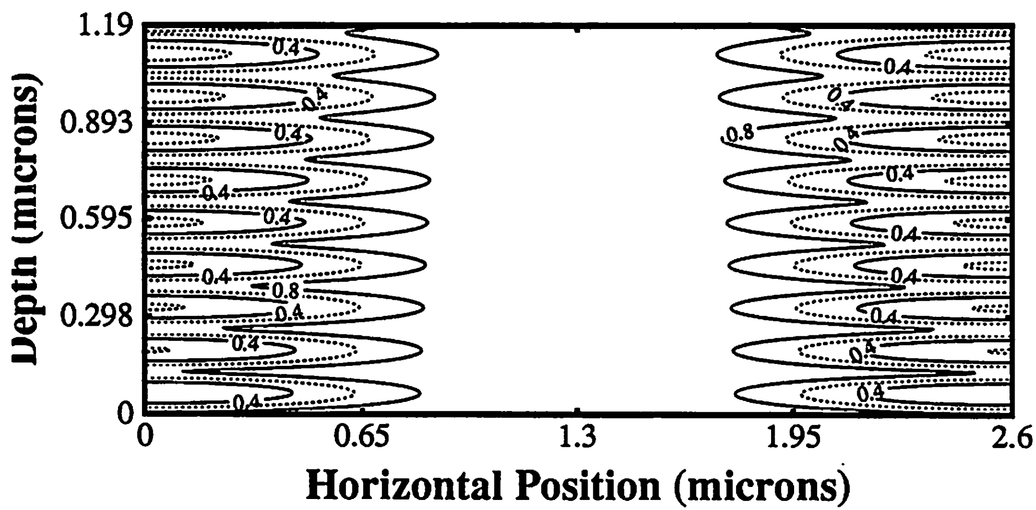

**Figure 2.7:** Depiction of the string algorithm used in the development routine of *SAMPLE*. The points on the string move perpendicular to the resist surface an amount proportional to the dissolution rate at that point.

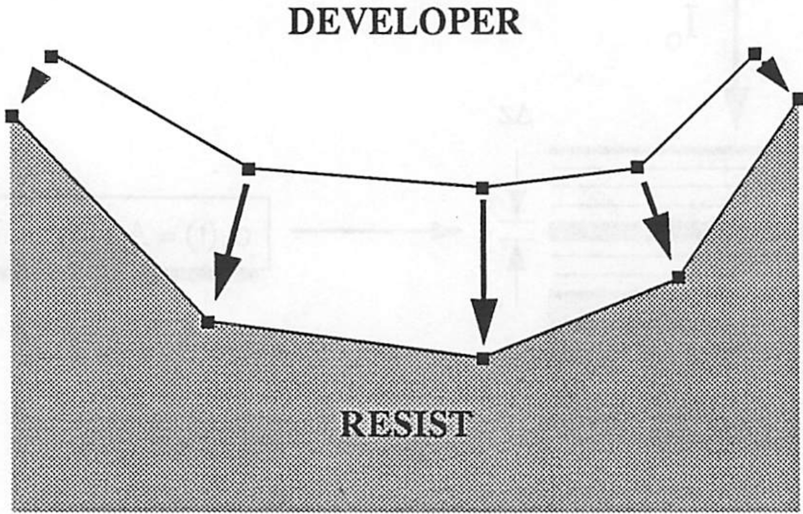


**Figure 2.8:** Simulated development profiles of KTI 820 resist using a line-space grating pattern with a pitch of 2.6 μm. Results are shown for a) a nominal dose of 99 mJ/cm$^2$, b) 22% underexposure, and c) nominal dose with 3 μm defocus.

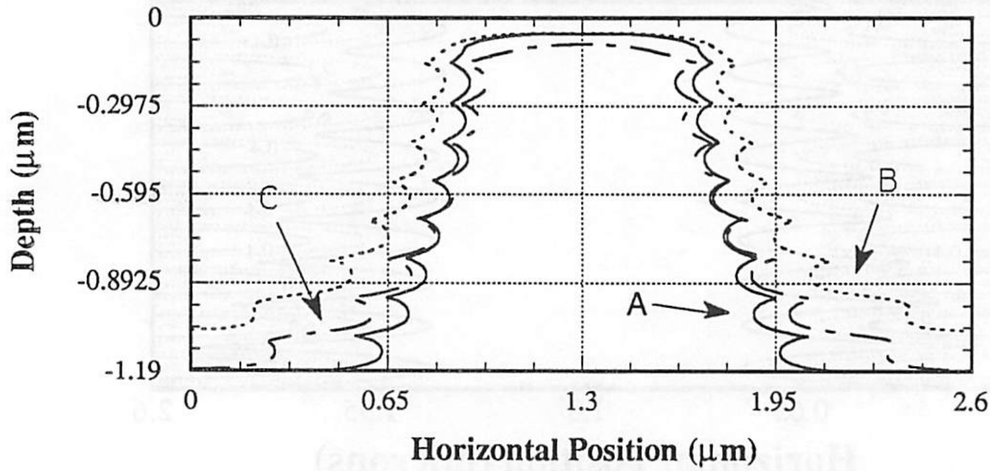

**Figure 2.9:** SEM pictures of KTI 820 resist using a line-space grating pattern with a pitch of 2.6 μm. Results are shown for a) a dose of 99 mJ/cm$^2$, b) 22% underexposure, and c) with 3 μm defocus. Reprinted from reference [47].

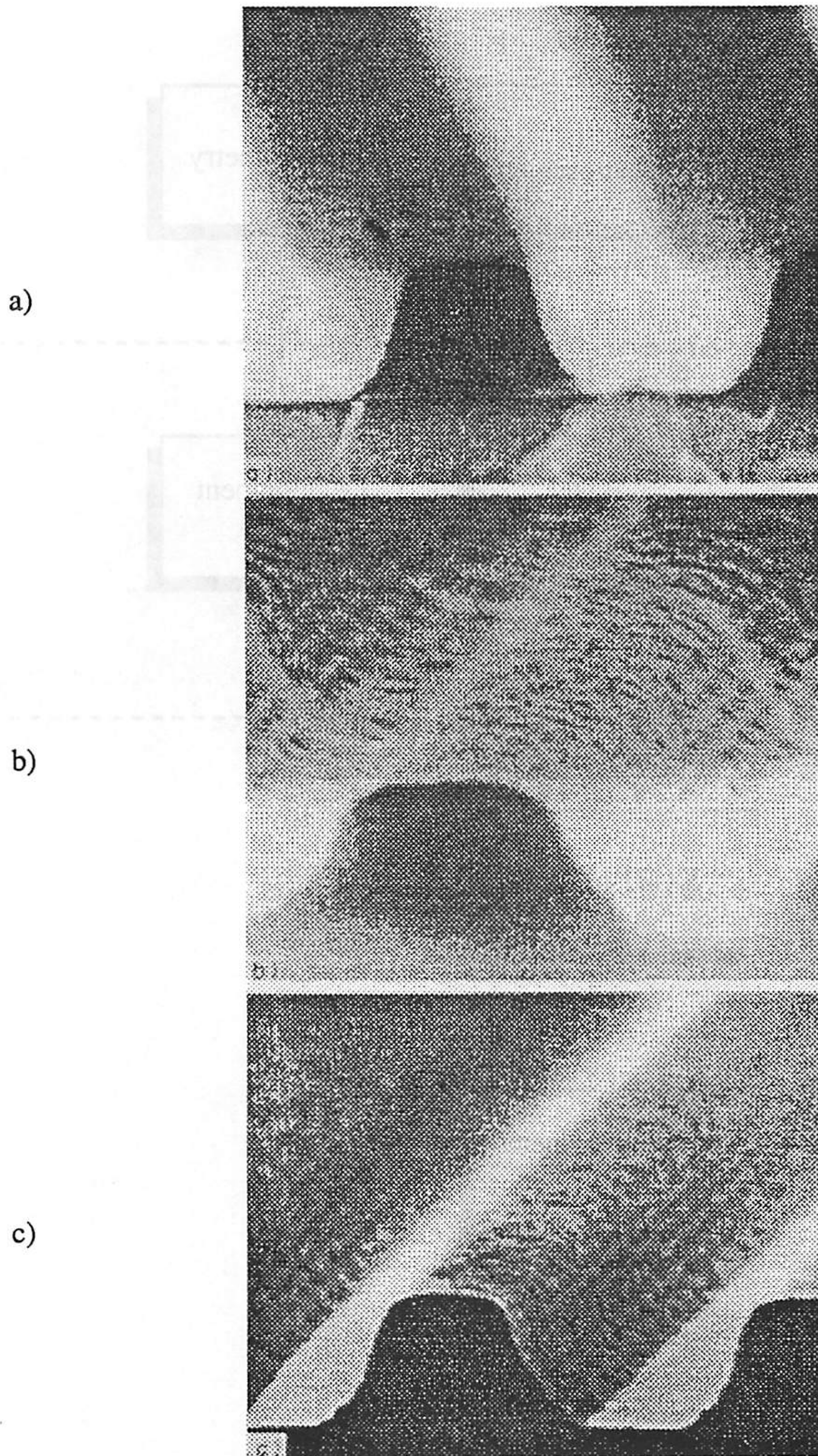

**Figure 2.10:** A general methodology for the characterization, modeling, and simulation of advanced resist technologies.

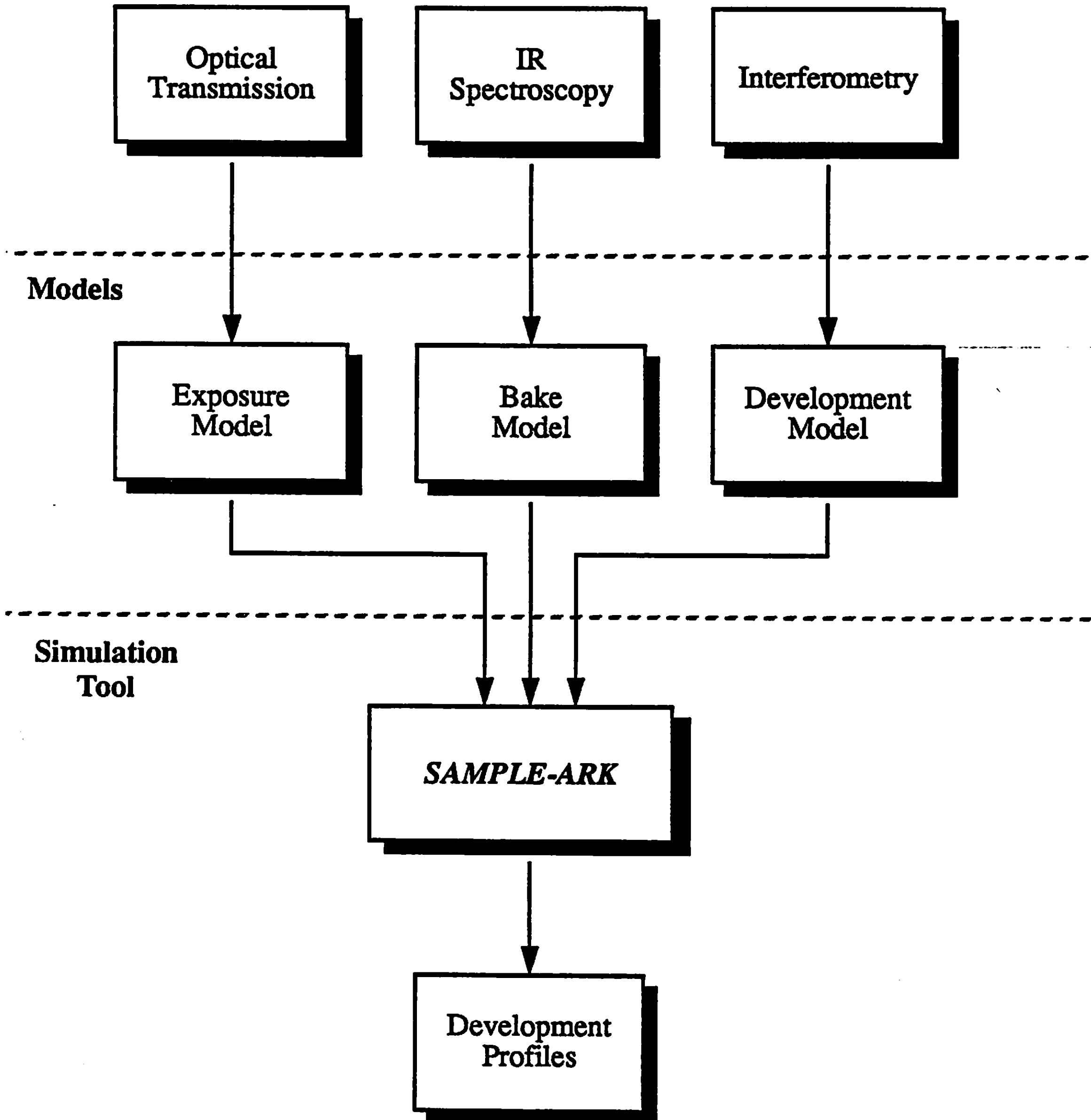

# CHAPTER 3

# THE *SAMPLE-ARK* PROGRAM

A new lithography simulation program, ***SAMPLE-ARK***, has been developed for the simulation of advanced resist technologies. This program, an extension of ***SAMPLE*** [1], simulates the chemical and physical changes that the resist undergoes during post-exposure processing (referred to here as a post-exposure bake). The user describes the post-exposure bake for a particular resist process in terms of the chemical species present within the resist and the basic mechanisms which modify their concentrations such as chemical reactions and diffusion. The program tracks the local concentration of these species as the bake progresses. At the conclusion of the bake, the dissolution rate can be expressed as an algebraic function of any species concentrations within the resist. This new program encompasses a wide variety of new and complex resist processes such as image reversal, chemical amplification, and silylation as will be demonstrated in Chapter 4.

## 3.1 INTRODUCTION

Current simulation tools have not kept pace with the recent influx of new technologies and complex resist materials for photolithography. The successful application of simulation to the understanding and optimization of resist processes such as image reversal, chemical amplification, and silylation requires the extensive modification of current simulation tools to include new and complex models that describe the resist behavior. The nature of these resist models dictate the requirements placed on the simulation tools to achieve the accurate simulation of both present and future resist technologies.

## 3.2 SIMULATION TOOL REQUIREMENTS

Several distinct approaches exist for extending current simulation tools. In perhaps the simplest approach, specific modifications are made to the program for each resist process that requires simulation. While this method can achieve both accurate and reliable results, repeated application for each new process can lead to excessive overlap. In a better strategy for the long term, common process attributes are used to develop a more general tool which can simulate a wider variety of resist processes.

While at a first glance, these new resist technologies differ significantly in many respects, several important similarities do exist between them that provide a strong base for the development of a general simulation program. Many of them follow a common process sequence consisting of exposure, post-exposure processing, and development. During the post-exposure processing, which for simplicity will be referred to here as a *post-exposure bake*, the resist undergoes critical chemical and physical changes which are fundamental to the resist performance. Current simulation tools, as shown previously in Figure 1.1, successfully simulate the exposure and development of diazo-type resists. In general, this simulation capability also applies to the exposure and development of more complex resist processes. Consequently, programs designed for diazo-type resists can be adapted for more advanced resist processes by including the simulation of the changes that occur within the resist during this additional post-exposure bake.

The basic chemical and physical mechanisms which determine the resist behavior during the post-exposure bake are also common to most resist processes. These mechanisms include chemical reactions and diffusion. Therefore, by including the simulation of a post-exposure bake in terms of these basic chemical and physical mechanisms, current simulation tools can be extended to encompass a wide variety of complex resist processes. In addition, by extending in this generalized manner through the use of mechanistic post-exposure bake

models, a simulation tool will not only be applicable to current resist technologies such as chemical amplification, image reversal, and silylation, but will also contain sufficient flexibility to simulate even future resist technologies with little or no change to the program code.

## 3.3 OVERVIEW OF *SAMPLE-ARK*

The approach outlined above has been used in the development of a general resist simulation tool, ***SAMPLE-ARK***, or ***SAMPLE*** with *A*dvanced ***R***esist ***K***inetics. This program, a modification of ***SAMPLE*** [1], simulates the reaction kinetics and diffusion that occur during post-exposure processing of advanced resist technologies. Figure 3.1 shows a schematic of resist simulation using ***SAMPLE-ARK***. The exposure and development routines of ***SAMPLE*** remain intact while a new bake routine has been included for simulation of the post-exposure bake.

### 3.3.1 *SAMPLE-ARK* Capabilities

The additional bake routine tracks the local concentration of up to ten chemical species throughout the resist as the bake progresses.† These species interact with one another through an unlimited number of user-defined chemical reactions. In addition, each of these species may also diffuse within the resist with either a constant or a concentration-dependent diffusion coefficient. Modification to the diffusion boundary conditions results in the ability to diffuse different chemical species into the resist from outside sources. Finally, the program allows for user-defined algebraic manipulation of species concentrations using a variety of mathematical operators. With this capability, dissolution rate models can be provided directly in the input to the program in terms of any chemical species concentrations within the resist.

---

†. A maximum number of ten chemical species was selected since it was felt that this number would be sufficient for simulating most resist processes of interest. This value can be increased quite easily by the user if necessary.

The diversity presented by this mechanistic-based, post-exposure bake description allows for the simulation of a large class of advanced resist processes without program modifications. Chapter 4 demonstrates this flexibility with three different resist examples: image reversal, chemical amplification, and silylation. The general nature of the input description using reactions and diffusion should, in fact, make ***SAMPLE-ARK*** easily extendable to future resist technologies that have yet to be invented.

### 3.3.2 Systems View Of *SAMPLE-ARK*

The operation of the new ***ARK*** bake routine can also be understood from a systems viewpoint. The system is comprised of a number of chemical species within the resist. The concentration of these species are the *state variables* of the system. The concentration of all of the chemical species combine to form the *state vector*, **C**(t), a mathematical description of the *state* of the system at any given time. Different stimuli such as exposure energy and bake temperature drive the system and cause the state of the resist to change. The simulation of a single process step involves the calculation of the resist state following completion of that process step.

Figure 3.2 presents a diagram of this systems viewpoint of ***SAMPLE-ARK*** in terms of the state variables, transitions, and stimuli for the exposure, post-exposure bake, and development simulation in ***SAMPLE-ARK***. The circles in this diagram represent the state variables, or the species concentrations, within the system. The arrows between the circles denote chemical transitions between various state variables which are driven by external stimuli. During the exposure, the illumination energy stimulates the transition between two state variables of a simple photolytic reaction. For a diazo-type resist, these two state variables correspond to the concentrations of PAC and ICA. Alternatively, in an acid catalyzed resist system, they represent the concentrations of the acid generator and the photo-generated acid.

During the post-exposure bake, the state of the resist changes through chemical reactions driven by the bake temperature. Figure 3.2 depicts two of these chemical reactions. The transitions between the state variables are described mathematically by the kinetic equations for these chemical reactions. In Figure 3.2, the reaction on the left corresponds to a simple first-order reaction while the reaction on the right represents a more complex, catalytic reaction. In addition to the chemical reactions, diffusion during the bake modifies the spatial distribution of the state variables. Finally, during development, the dissolution rate is expressed as a function of the state variables within the resist following the bake as shown in Figure 3.2.

### 3.3.3 *SAMPLE-ARK* Operation

Figure 3.3 shows a flow diagram of *SAMPLE-ARK* operation during the simulation of a post-exposure bake process. The simulation begins with the exposure of the resist using the standard *SAMPLE* exposure routine. Following the exposure, *SAMPLE* initiates the *ARK* bake module. At this point in the simulation, the user must provide a complete description of the post-exposure bake. This description begins with the specification of the bake conditions consisting of the temperature and time of the bake. The next step is to establish the initial concentrations of the different chemical species present within the resist. The concentration of a given species may be independent of location within the resist or may have some spatial distribution as a result of the exposure. The chemical and physical changes that the resist undergoes during the bake are then described through a system of chemical reactions and diffusion coefficients specific to the particular resist process under simulation. Following a complete description of the bake, the program converts the user-specified chemical reactions and diffusion coefficients to a system of nonlinear first-order differential equations. A numerical algorithm solves these differential equations for the species concentrations as a function of bake time at each location within the resist.

After simulating the post-exposure bake, two options exist for returning control to the standard dissolution routine of *SAMPLE*. In the first option, the spatial concentration matrix of one of the chemical species within the resist is returned for dissolution simulation using any of the development models provided in *SAMPLE*.† The second option provides a more flexible method for simulating the resist dissolution. In this case, a dissolution rate expression in terms of any species concentrations may be input directly into the program by the user. The *ARK* bake routine uses this dissolution expression to calculate the dissolution rate at each point in the resist and then returns the rate matrix to the *SAMPLE* dissolution routine for simulation of the final development profile.

### 3.3.4 Program Basics

The new post-exposure bake routine of *SAMPLE-ARK* has been written in the C programming language. The program uses the dynamic memory allocation feature in C and thus provides for the efficient use of the computer memory. The largest memory usage occurs when ten diffusing species are present within the resist.‡ This case requires approximately 8.7 Mbytes of memory. However, simulation of simpler examples such as a resist containing four chemical species with no diffusion requires as little as 3.2 Mbytes.* The bake routine is comprised of eight C modules. These modules total approximately 3500 lines of code. In addition, several of the standard *SAMPLE* modules have been modified.

#### 3.3.4.1 Compatibility with *SAMPLE*

With the choice of C for the programming language of the new bake routine, compatibility with the old *SAMPLE* code written in FORTRAN77 becomes a critical issue. The FOR-

---

†. See Chapter 2 for a description of the development models available in *SAMPLE*.

‡. Diffusion requires much more memory in comparison with chemical reactions alone.

*. This memory requirement should, for these cases, be sufficiently small to allow the porting of the program to personal computers with a moderate amount of memory.

TRAN subroutine call for running the C bake routine requires a specialized link that depends upon the specific operating system in use. The present version of the code has been written for use with a UNIX operating system, and the link between the C and the FORTRAN code is transparent to the user. Other operating systems may require further modifications and thus may be somewhat more difficult.

#### 3.3.4.2 Command Format

The post-exposure bake routine contains an input parser that reads in the command lines describing the bake. These commands possess a similar format to those commands used by the standard *SAMPLE* program and are included in the same input file. Each command line begins with a keyword which describes an action, sets a parameter, or specifies a particular model. The command line ends with a semicolon (;). Chapter 4 contains several example input files used for the simulation of complete resist processes.

One important aspect used in the post-exposure bake commands involves the assignment of different names to the chemical species present within the resist. By naming each of the chemical species, the user has the capability of distinguishing between them. The program associates each of these names with a matrix that contains the concentration of that species at each point in the resist. For example, the input command:

- initialize acid 0;

will initialize the local concentration of a chemical species named *acid* to zero.

### 3.4 PROGRAM COMMANDS IN *SAMPLE-ARK*

The following sections describe some of the important commands for the *SAMPLE-ARK* bake routine. The Appendix provides a complete list of all of the commands as well as a description of how to use them.

### 3.4.1 Starting and Ending the Post-Exposure Bake

The **startbake** and **endbake** commands signify the beginning and end of the post-exposure bake description, respectively. The **startbake** command is a keyword that is read in by the standard *SAMPLE* parser that initiates the running of the post-exposure bake routine. Between the **startbake** and **endbake** commands, all remaining commands describe the post-exposure bake and are interpreted by the post-exposure bake input parser. The **endbake** command returns control to the standard *SAMPLE* program.

### 3.4.2 Specifying the Bake Conditions

The **temperature** and **time** commands specify the conditions for the post-exposure bake. The temperature is given in degrees Celsius while the bake time is expressed in seconds. For example, the pair of commands:

- temperature 150;
- time 60;

specify a bake temperature of 150°C for 60 seconds.

### 3.4.3 Initializing Species Concentrations

The **initialize** command is used to initialize the concentration of a chemical species at each point in the resist. The simplest case occurs when the initial concentration at the beginning of the bake is independent of location within the resist. To initialize the concentration in this case, the species name and the concentration follow the **initialize** keyword. For example, the command:

- initialize a 1e15;

initializes the concentration of species A to a value of $1x10^{15}$ at each point in the resist.

The concentration of a chemical species may also be determined by the exposure step, and thus vary with position in the resist. The exposure routine in ***SAMPLE*** was originally written to simulate the destruction of PAC. However, this routine is general enough to simulate any simple photolytic reaction given by:

$$S_1 \xrightarrow{h\nu} S_2 \qquad [3.1]$$

In the case where the exposure determines the species concentration, the *expose* and *expose_inv* parameters of the **initialize** command (see the Appendix) are used to initialize the species concentration to the normalized concentration of species $S_1$ and $S_2$ of equation [3.1], respectively. A multiplicative constant following either of these parameters scales the results. For example, the command:

- initialize C expose_inv 1;

initializes the concentration of species C to the concentration of species $S_2$ in equation [3.1] following exposure and leaves the results normalized to a value of one.

### 3.4.4 Specifying Chemical Reactions

Interaction between the chemical species within the resist occurs through chemical reactions. The chemical reactions are specified using the **reaction** command. The parameters in the **reaction** command define the rate coefficient, the reactants, and the products of the reaction. The user may specify any number of chemical reactions involving up to ten different chemical species by simply listing each reaction with a separate **reaction** command. The specific format for the **reaction** command is given in the Appendix.

The following example illustrates the use of the **reaction** command in specifying a chemical reaction. The hypothetical reaction:

$$2A + B \rightarrow C \qquad [3.2]$$

with a reaction rate coefficient of k = 1, reactants A and B, and product C is expressed in ***SAMPLE-ARK*** with the command:

- reaction k = 1, in = a(2),b out = c ;

The names of the species that follow the *in* parameter of the **reaction** command are the reactants in the reaction while those that follow the *out* parameter are the products. Parentheses delineate the number of molecules of a given species that participate in the reaction when this number is not equal to one.

Through the laws of chemical reaction kinetics, the program converts the input description of a chemical reaction into a system of nonlinear differential equations which describe the time rate of change of each of the chemical species [2]. For example, the chemical reaction of equation [3.2] results in a set of differential equations given by:

$$\frac{\partial [A]}{\partial t} = -2 [A]^2 [B] \qquad [3.3]$$

$$\frac{\partial [B]}{\partial t} = -[A]^2 [B] \qquad [3.4]$$

$$\frac{\partial [C]}{\partial t} = [A]^2 [B] \qquad [3.5]$$

In modeling the kinetics of a chemical reaction, it may sometimes appear that a given chemical species participates in that reaction with a non-integer power.† The model derived

†. This occurs most often when the reaction has not been expressed in terms of the fundamental reaction mechanism. Also, reactions in polymers may not always follow the basic laws of reaction kinetics.

in Chapter 6 for the acid catalyzed crosslinking reaction in Shipley SNR 248 resist presents a prime example of this effect. The photo-generated acid participates kinetically in this crosslinking reaction with a power of 1.42. This type of behavior is easily specified in the **reaction** command, once again, by including this non-integer number in the parentheses following the species name.

The specification of the rate coefficient can take several forms. Listing of the rate coefficient alone using the *k* parameter of the **reaction** command, as demonstrated in the above example, provides an absolute number for the rate coefficient that has no dependence on the bake temperature. Specifying a bake temperature with the **temperature** command, in this case, will not affect the simulation results. However, providing an activation energy with the *ea* parameter (see the Appendix for details) results in a temperature dependence for the rate coefficient given by:

$$k = k_o exp\left(-\frac{E_A}{K_B T}\right) \quad [3.6]$$

where $E_A$ is the activation energy in eV, $k_o$ is a pre-exponential specified with the *k* parameter, $K_B$ is Boltzmann's constant, and T is the bake temperature in degrees Kelvin.

#### 3.4.4.1 Chemical Reaction Data Structure

The program allows the user to input an unlimited number of chemical reactions in terms of up to ten chemical species. The flexibility presented by this input format results from the linked-list data structure used to store the information about the chemical reactions. Each time the user includes a new reaction in the input, the program adds a new element onto the end of this linked list. Each element of the linked list contains entries for the reaction rate coefficient, the reactants, the products, and a pointer to the next element or reaction in the linked list.

Figure 3.4 shows an example of a linked-list data structure containing two reactions. The linked list shown corresponds to the hypothetical reactions:

$$A + B \xrightarrow{k=1} C \qquad [3.7]$$

$$2A \xrightarrow{k=2} C \qquad [3.8]$$

The reactant and product arrays in the linked list specify the number of molecules of each species that participate in the reaction. An entry of zero for a species in both the reactant and product arrays simply denotes that this chemical species was not involved in the chemical reaction. Once all of the reactions have been read into this linked list, the program converts the list into a system of differential equations using the laws of reaction kinetics as described earlier.

### 3.4.5 Specifying Diffusion

The chemical species may also move throughout the resist by diffusion. The diffusion of up to ten chemical species is allowed in the program and may occur simultaneously with any number of chemical reactions. The diffusion is assumed to follow the Fickian diffusion equation (Case I) given by:

$$\frac{\partial C_i}{\partial t} = \nabla \cdot (D_i \nabla C_i) \qquad [3.9]$$

where $C_i$ and $D_i$ are the concentration and the diffusion coefficient of the $i^{th}$ species, respectively [3]. The **diffuse** command is used to specify the diffusion coefficient of any given chemical species.

### 3.4.5.1 Constant Diffusion Coefficient

The simplest case of diffusion occurs with a constant diffusion coefficient. In this case, by moving the diffusion coefficient outside of the divergence of equation [3.9], the diffusion equation simplifies to:

$$\frac{\partial C_i}{\partial t} = D_i \nabla^2 C_i \qquad [3.10]$$

Diffusion with a constant diffusion coefficient as in equation [3.10] is easily specified in the program using the **diffuse** command. The **diffuse** command format is given by:

- diffuse *species_name diffusion_coefficient;*

where the units for the diffusion coefficient are in μm²/sec. For example, the command:

- diffuse a 1e-5;

results in the diffusion of species A with a constant diffusion coefficient of $1\times10^{-5}$ μm/sec².†

In order to solve the diffusion equation on the discrete spatial grid that defines the resist, the program uses a second-order Taylor series approximation for the spatial derivatives in equation [3.10]. The notation $C_i(j,k)$ denotes the concentration of the $i^{th}$ chemical species at point $(x_j,z_k)$ on the discretized grid depicted in Figure 3.5. The approximation for the second derivative in the x dimension is then given by [3]:

$$\frac{\partial^2 C_i}{\partial x^2} \approx \frac{C_i(j+1,k) - 2C_i(j,k) + C_i(j-1,k)}{(\Delta x)^2} \qquad [3.11]$$

†. At this point, the diffusion coefficient is assumed to have no temperature dependence. This can be corrected in the future to include an Arrhenius behavior if necessary.

where $\Delta x$ is the spacing between grid points in the x direction. Using a similar approximation for the z direction term of equation [3.10], the diffusion equation becomes discretized for application to a resist grid with rectangular grid elements.

The approximated diffusion equation has a similar form to the kinetic equations obtained from chemical reactions (see for example equations [3.1] - [3.3]) in that the time rate of change of a species concentration is equated to an expression involving species concentrations only. For the diffusion equation, this expression includes the concentration at the neighboring grid points. Because of this similarity, the same algorithm (see Section 3.5) can be used to solve both the kinetics of the chemical reactions as well as the diffusion equation. When chemical reactions and diffusion occur simultaneously, then the approximation to the right-hand side of equation [3.10] simply provides an additive term to the kinetic equation describing the time rate of change of the $i^{th}$ species concentration.

The diffusion of PAC during the post-exposure bake of a diazo-type resist provides a good example for demonstrating diffusion in ***SAMPLE-ARK***. The post-exposure bake reduces the standing wave pattern in the PAC concentration that results from coherent interference between transmitted and substrate reflected energy during exposure. The reduction in the standing wave pattern subsequently reduces the lateral dissolution of the resist during development providing a more vertical sidewall in the final resist image.

For g-line exposures, a diffusion length of about 0.08 μm completely blurs the standing wave pattern. Since the diffusion length is defined as $2\sqrt{Dt}$, a post-exposure bake for 160 seconds with a diffusion coefficient of $1\text{x}10^{-5}$ $\mu m^2$/sec for the PAC will provide this diffusion length. Figure 3.6 shows the development profiles for KTI 820 resist with and without the post-exposure bake. Use of the post-exposure bake results in the complete removal of the standing wave "fingers" in comparison to the profile obtained with no bake. In addition, the

resist profile demonstrates a slight increase in sidewall angle as a result of PAC diffusion during the post-exposure bake.

### 3.4.5.2 Concentration-Dependent Diffusion

In some cases, the diffusion coefficient may depend upon the concentration of one or more chemical species within the resist. For example, some silylation processes such as the DESIRE process rely on the selective diffusion of silicon containing compounds into the resist. Consequently, the more general diffusion equation [3.9] must be solved in cases involving concentration-dependent diffusion. Equation [3.9] can be rewritten as:

$$\frac{\partial C_i}{\partial t} = D_i \nabla^2 C_i + \nabla D_i \nabla C_i \qquad [3.12]$$

This equation contains the simplified diffusion equation [3.10] plus an additional term resulting from the gradient of the diffusion coefficient. To solve equation [3.12] on the discretized spatial grid, the approximated diffusion equation derived earlier for the constant diffusion case requires some additional terms to account for this concentration dependence.

Using a first-order Taylor series approximation† for the extra concentration-dependent term of equation [3.12], the additional term in the x direction for the approximated diffusion equation on the discretized grid becomes:

$$\text{x-direction term} = \frac{[C_i(j+1,k) - C_i(j-1,k)]\,[D_i(j+1,k) - D_i(j-1,k)]}{4(\Delta x)^2} \qquad [3.13]$$

A comparable term exists as well for the z direction.

†. Because this is a lower order approximation, a higher grid density is required for accuracy when simulating concentration-dependent diffusion.

The concentration-dependent diffusion coefficient is also specified using the **diffuse** command. However, in this case, the diffusion coefficient is given as an algebraic expression in terms of any species concentrations within the resist. For example, if the diffusion coefficient of hypothetical species A depended upon the square of the concentration of species B, then the command would take the form:

- diffuse a b^2;

The rules governing the specification of concentration-dependent diffusion coefficients in the diffuse command follow the guidelines for including algebraic expressions in the define command as described in Section 3.6.6. When using a concentration-dependent diffusion coefficient, the algebraic expression provided in the input description is stored by the program as a character string of algebraic operators and species names and, during each time step, is converted to a specific number for the diffusion coefficient at each location in the resist.

#### 3.4.5.3 Boundary Conditions for Diffusion

As a default, the boundary conditions for diffusion in ***SAMPLE-ARK*** specify that no net flow of any chemical species occurs across the boundaries within the resist. These boundary conditions in the z direction are given mathematically by the equation:

$$\frac{\partial}{\partial z}C_i(x, z) = 0|_{z=0,T} \qquad [3.14]$$

where T is the resist thickness. In using these boundary conditions, the total concentration of any diffusing species within the resist remains constant.

Some processes require alternative boundary conditions at the top surface of the resist. In a silylation process, silicon-containing compounds diffuse into the resist from an outside source. In order to simulate a process such as this, the program allows for the diffusion of species into the resist by forcing the concentration of that species to a constant at the resist surface. This surface concentration is equivalent to the solid solubility of the species within the resist. Mathematically, this boundary condition is given by:

$$C_i(x, z) = C_{ss}|_{z=0} \quad [3.15]$$

where $C_{ss}$ is the solid solubility concentration. The **diffsource** command is used to specify this boundary condition. For example, the diffusion of species A into the resist with a normalized concentration of one at the surface is specified by:

- diffsource a 1;

A silylation example in Chapter 4 will demonstrate diffusion from an outside source using the **diffsource** command. In the future, alternative boundary conditions are needed to simulate other cases such as the out-diffusion of a chemical species from the resist.

### 3.4.6 Algebraic Manipulations with the DEFINE Command

Chemical reactions and diffusion provide physically based methods for manipulating species concentrations in the resist. However, mechanistic models may not always be available or convenient for describing the post-exposure bake. Therefore, the program also allows the user to define the concentration of a given species through an algebraic expression in terms of other species concentrations within the resist. The **define** command is used to input this algebraic expression into *SAMPLE-ARK*. For example, relating the concentration of hypothetical species C to the average of the concentration of species A and B is done with the **define** command by:

- define c (a+b)/2;

Table 3.1 gives a complete list of the operators that can be used in the **define** command.

| Operator | Description |
|---|---|
| + | Addition |
| - | Subtraction |
| * | Multiplication |
| / | Division |
| ^ | Raise to power |
| ( ) | Parentheses |
| exp( ) | $e^x$ |
| log( ) | Log (base 10) |
| ln( ) | Natural Log |

**Table 3.1:** Table of operators for use with the **define** command.

### 3.4.7 Specifying Dissolution Functions

Two methods exist for specifying the dissolution rate in *SAMPLE-ARK*. The first method uses previously hardwired dissolution rate functions in the program code itself to express the dissolution rate in terms of a single chemical species concentration. The second method, a much more powerful approach, takes advantage of the flexibility presented by the **define** command to input a dissolution rate function directly into the program input itself in terms of any species concentrations within the resist.

The first, more conventional, method makes use of the **return** command in generating the local dissolution rate in the resist. This command returns the concentration matrix of a given species to the standard dissolution routine in ***SAMPLE***. The returned matrix replaces the "M" matrix which usually stores the normalized PAC concentration of diazo-type resists. With the selection of one of the standard dissolution equations provided in ***SAMPLE***, the program converts the local concentration in the "M" matrix to a dissolution rate and then, using the string algorithm described in Chapter 2, calculates the final development profile. With this method, if the user requires a new dissolution rate equation not provided by the program, the ***SAMPLE*** code must be modified to include it.

The flexibility associated with the **define** command presents a more powerful approach for specifying a dissolution rate equation in ***SAMPLE-ARK***. This alternative approach, in contrast to the first method, requires no modification to the program source code. The dissolution function is described through the **define** command which contains an algebraic expression relating the dissolution rate to the concentration of any chemical species within the resist. This command creates a matrix containing the dissolution rate itself at each point in the resist. This rate matrix is then returned to the standard ***SAMPLE*** development routine using the **return** command. Since the dissolution rate is then known at each point in the resist, the final development profile is easily calculated.

The type of dissolution rate function that can be defined in this manner is only limited by the constraints placed on the algebraic expression in the **define** command. The dissolution model developed for SNR 248 resist in Chapter 6 provides a good example for using this powerful feature. The expressions derived in equations [6.9] and [6.13] are not included amongst the standard development models available in ***SAMPLE***. However, by using the following input lines in ***SAMPLE-ARK***:

- define ce 15*cas^2 - 20*cas^3 + 15cas^4 - 6*cas^5 + cas^6
- define rate 350 * (1 - ce/6.3) ^ 6.5
- return rate

a matrix containing the local dissolution rate can be returned to the standard dissolution routine for development.

### 3.4.8 Running the Bake

After the complete specification of the post-exposure bake in terms of the chemical reactions, diffusion coefficients, initial species concentrations, and bake conditions, the program solves for the concentration of all of the chemical species at each point in the resist. The program performs this calculation when the **bake** command is given by the user. The numerical algorithm contained in ***SAMPLE-ARK*** which solves for the species concentrations during the bake is presented in the following section.

## 3.5 SOLVING THE SYSTEM OF DIFFERENTIAL EQUATIONS

The program converts the information concerning the chemical reactions and diffusion coefficients to a system of differential equations as described earlier. In general, this system of differential equations is given by:

$$\frac{\partial C_1}{\partial t} = f_1(C_1, \ldots, C_n) \qquad [3.16]$$

$$\vdots$$

$$\frac{\partial C_n}{\partial t} = f_n(C_1, \ldots, C_n)$$

*SAMPLE-ARK* solves this system of nonlinear first-order differential equations for the concentration of all of the chemical species at each location within the resist. In order to pro-

vide the generality needed to solve a wide range of such differential equations, a rigorous numerical routine is used to perform these calculations. While the differential equations are of a similar nature for both chemical reactions and diffusion as discussed earlier, the inclusion of diffusing species does require some modification in solving these equations since the concentration at any one point in the resist depends upon the concentration in the surrounding area.

The following section describes the numerical algorithm used to solve the system of differential equations given in [3.15] for a post-exposure bake in which only chemical reactions occur. Section 3.7.2 details the modifications to the numerical solution when diffusion is present within the resist as well.

### 3.5.1 The Numerical Algorithm

In order to solve the set of differential equations given by [3.16], a numerical algorithm must estimate the concentration of each of the chemical species at discrete points in time as the bake progresses. The simplest method for doing this is referred to as a one-step method in which the current concentrations are estimated from the concentrations calculated at the previous time step [5]. Mathematically, the one-step method is described by:

$$C_i(t+\Delta t) = C_i(t) + \Delta t \cdot \phi(C_i(t), \ldots, C_n(t); \Delta t) \qquad [3.17]$$

The type of one-step method selected determines the form of the increment function, $\phi$, as well as the step size, $\Delta t$.

A variable step algorithm that employs a pair of fourth and fifth order Runge-Kutta methods for the increment function, $\phi$, was chosen to solve the differential equations [5]. In this algorithm, a comparison between the solutions obtained using the two high order methods provides a measure of the error associated with each time step. This estimate of the error is

then used to adjust the step size, $\Delta t$, during each time increment such that a given overall accuracy is achieved in the final solution. This sophisticated variable step approach solves the differential equations more efficiently than a fixed step method which may become exceedingly slow when the step size is too small or grossly inaccurate when the step size is too large. While this method does require additional calculations in evaluating the step size, the increase in efficiency more than makes up for the increased computation time associated with performing these calculations.

While this algorithm provides an accurate solution within reasonable computation times for most of the systems of differential equations studied thus far, the implementation of faster or more advanced algorithms may become desirable in the future. For this reason, the routine has been written in a modular fashion such that it can be easily replaced with an alternative differential equation solver at a later time.

The concentrations of each of the chemical species within the resist at the start of the bake provide the initial conditions for the differential equations. Since, in general, each location within the resist, as defined by the grid points of the concentration matrices, begins the bake with different initial concentrations, the differential equations must be solved at each grid location individually. For example, simulating the bake for a resist defined by a grid with 50 horizontal points and 200 vertical points requires that the differential equations be solved 10,000 times. For a bake defined in terms of chemical reactions only, the differential equations at a single grid point do not depend on the surrounding grid and can thus be solved independently. Consequently, the step size can be optimized for each individual grid point to minimize computation time.

### 3.5.2 Modifications For Diffusion

When diffusion occurs during the bake, the differential equations at a single location in the resist depend upon the concentration of the neighboring grid points. Therefore, the equations must be solved throughout the resist simultaneously. In this case, the step size for the numerical solution is determined by the one grid point that requires the smallest time increment for accuracy. The inefficiency that results from using a single step size for the entire resist grid leads to an increase in computation time when simulating diffusion. For example, solving the reaction kinetics without diffusion at each grid point individually for the acid catalyzed crosslinking reaction in Shipley SNR 248 deep-UV resist (see Chapter 6) took 66 CPU seconds on a DECstation 3100. However, solving the same kinetics at each grid point simultaneously using a single step size for the entire grid required 651 CPU seconds, or almost an order of magnitude increase in computation time.

When the chemical reactions are the dominant mechanism during the bake, a sequential solution of the reaction-diffusion equations can sometimes be used to reduce the computation time. In this sequential approach, a spatial redistribution of the diffusing species through an initial application of the diffusion equation alone precedes the solution of the reaction kinetics. The benefits of this approach can be demonstrated for the Shipley SNR 248 resist where the acid catalyzed crosslinking reaction occurs simultaneously with the diffusion of the photo-generated acid (see Chapter 6). Figure 3.7 shows the simulated development profiles for SNR 248 obtained through both the simultaneous and the sequential solution† of the reaction-diffusion equations, respectively. The sequential solution of the equations provides a good approximation to the more exact solution with a 95% savings in computation time. It is

---

†. The sequential solution required a reduction in the diffusion coefficient to achieve similar results since the crosslinking did not occur simultaneously.

expected, however, that as the diffusion coefficient becomes larger, the approximate solution will become less accurate.

### 3.6 SUMMARY

A new lithography simulation program, ***SAMPLE-ARK,*** has been developed for the simulation of advanced resist technologies such as image reversal, chemical amplification, and silylation. The program expands upon the exposure and dissolution routines of ***SAMPLE*** to include additional post-exposure processing in which a resist may undergo critical changes that are fundamental to the resist process. Simulation of this post-exposure bake is performed in terms of the basic chemical and physical mechanisms occurring within the resist including chemical reactions and diffusion.

The ability to simulate a wide variety of resist processes is derived from the flexibility associated with the input description of the post-exposure bake. A linked-list data structure provides the means for simulating an unlimited number of user-specified chemical reactions during the bake. Diffusion of chemical species within the resist can occur with either constant or concentration-dependent diffusion coefficients. Modification to the boundary conditions at the resist surface can result in the diffusion of chemical species into the resist from an outside source. After specification of the bake, the program converts the chemical reactions and diffusion coefficients to a set of nonlinear differential equations. These equations are solved for the local concentration of each species as the bake progresses with a Runge-Kutta numerical algorithm which uses an automatic time-step adjustment for efficiency. Following the numerical solution, the user can provide an arbitrary algebraic expression defining the local dissolution rate in terms of any species concentrations within the resist. With the inclusion of these powerful features, it is expected that ***SAMPLE-ARK*** will have the ability to simulate both present and future resist technologies with little or no modification to the program code.

## REFERENCES


[1] W. Oldham, S. Nandgaonkar, A. Neureuther, and M. O'Toole, "A General Simulator for VLSI Lithography and Etching Processes: Part I - Application to Projection Lithography," *IEEE Transactions on Electron Devices*, vol. ED-26, no. 4, pp. 717-722, April 1979.

[2] see for example D. Oxtoby and N. Nachtrieb, *Principles of Modern Chemistry*, Philadelphia, PA: Saunders College Publishing, 1986.

[3] J. Crank, *The Mathematics of Diffusion*, New York, NY: Oxford University Press, 1975.

[4] F. Coopmans and B. Roland, "DESIRE: A Novel Dry Developed Resist System," *Proceedings SPIE: Advances in Resist Technology and Processing III*, vol. 631, pp. 34-39, 1986.

[5] L. Johnson and R. Riess, "Numerical Analysis," Reading, MA: Addison-Wesley Publishing Company, 1982.

**Figure 3.1:** A modified schematic of optical lithography simulation with *SAMPLE-ARK*.

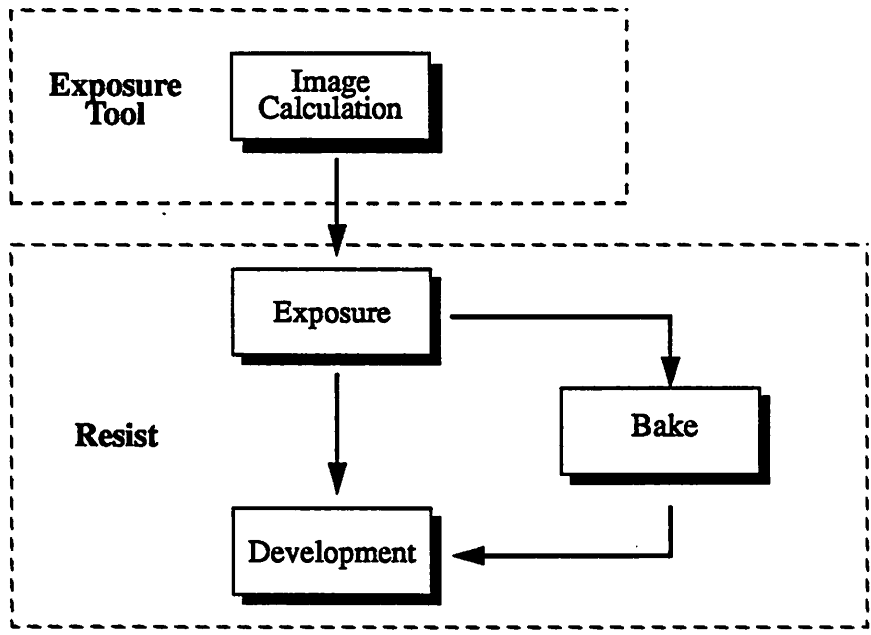

**Figure 3.2:** A state diagram of the exposure, post-exposure bake, and development steps in *SAMPLE-ARK* from a systems perspective. The diagram includes state variables (species concentrations) represented by circles, transitions between state variables, and stimuli that drive the transitions.

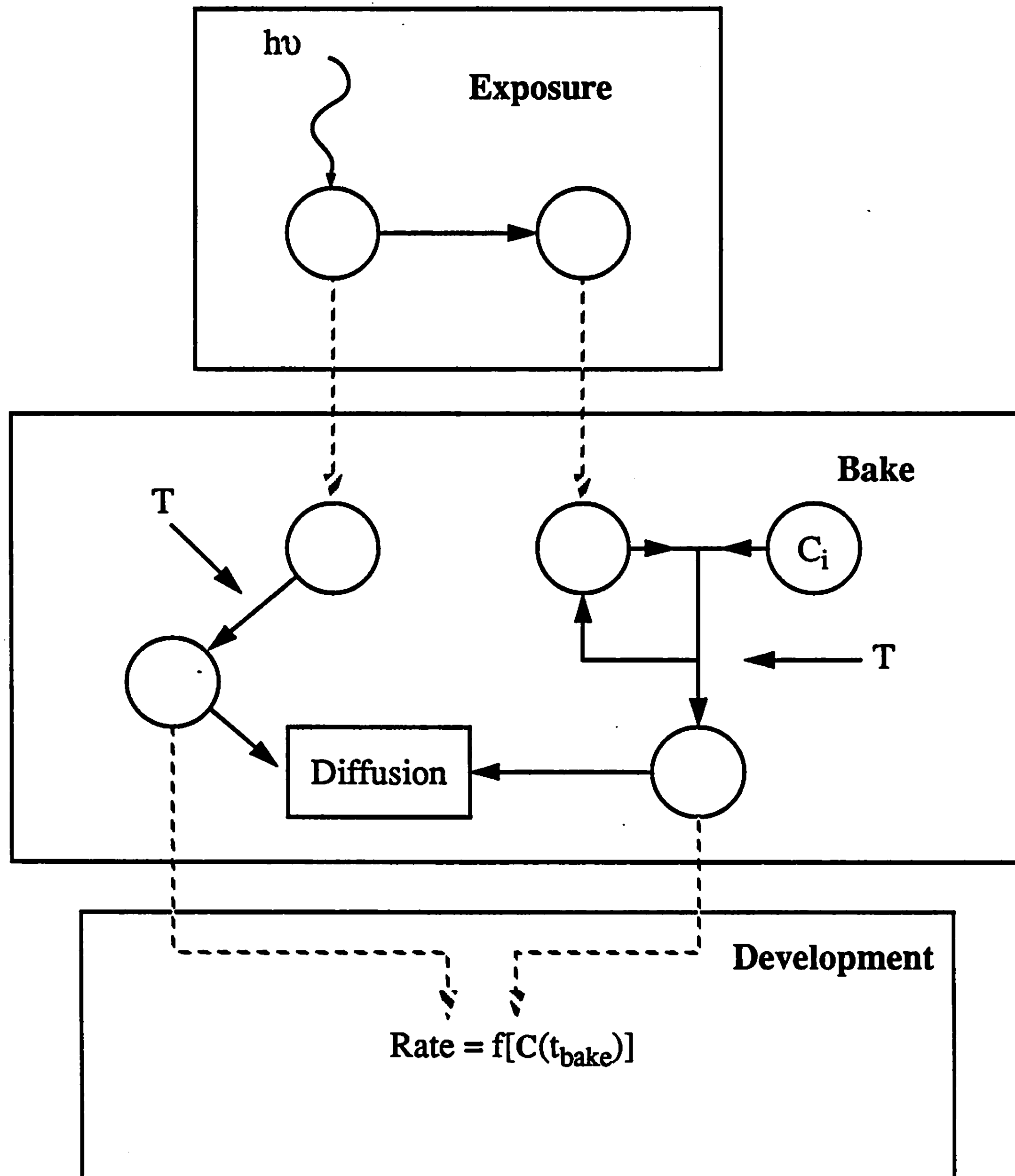

**Figure 3.3:** A flow chart of post-exposure bake simulation with *SAMPLE-ARK*.

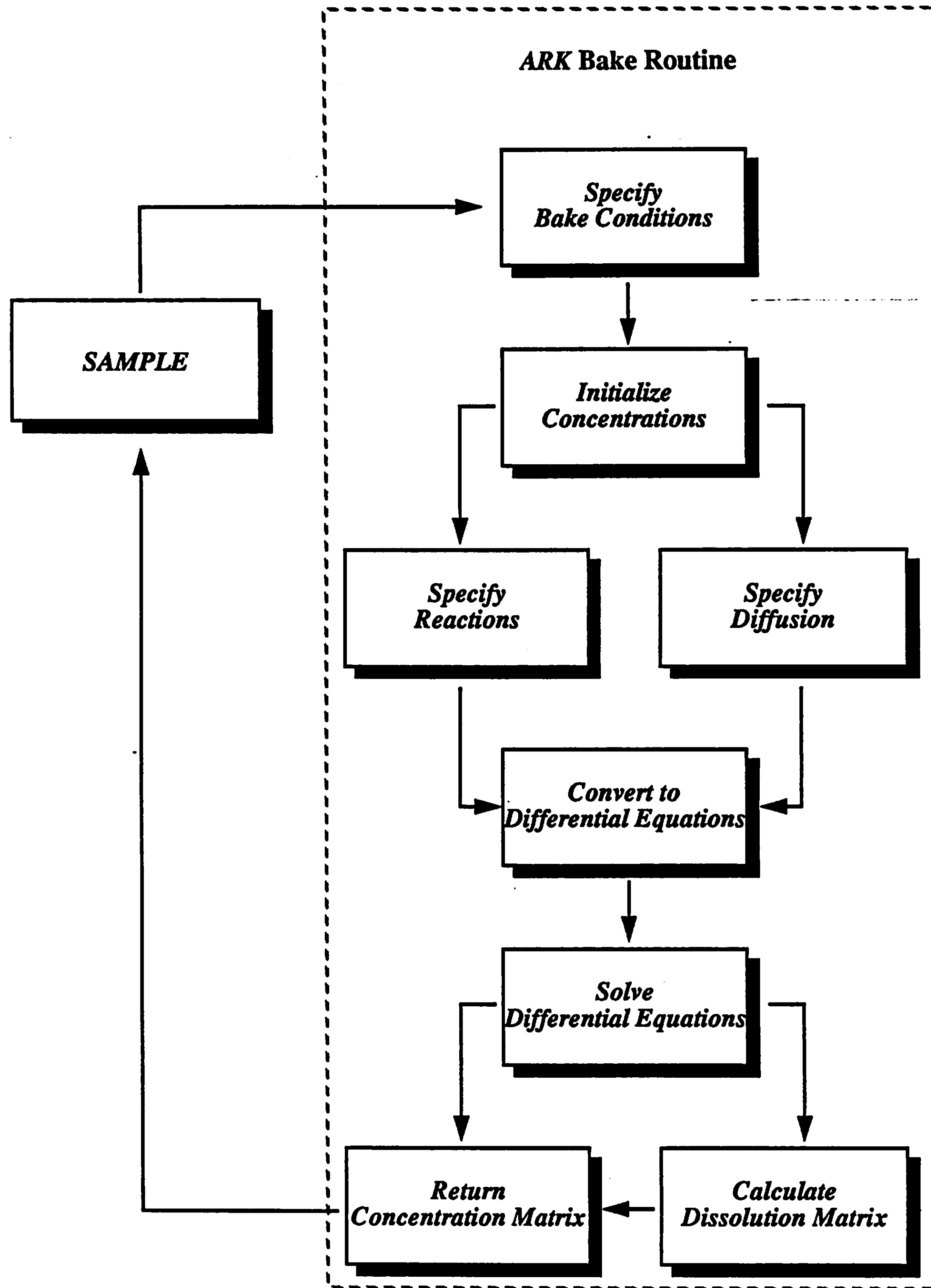

**Figure 3.4:** An example of the linked list data structure for chemical reactions in *SAMPLE-ARK.*

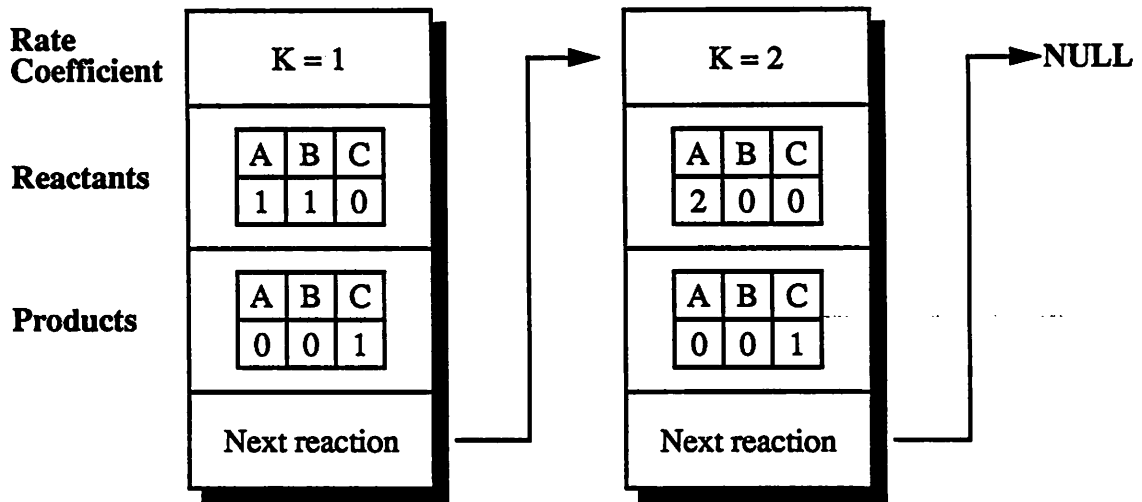


**Figure 3.5:** A diagram of the spatial grid that defines the resist during the post-exposure bake.

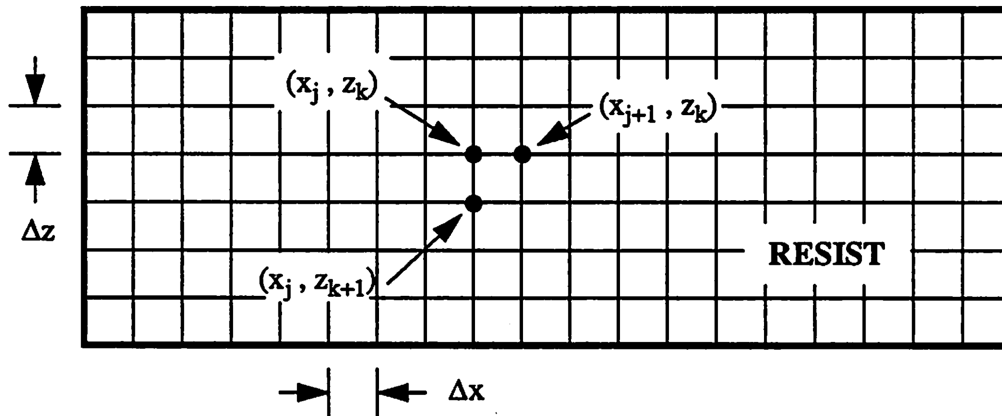

**Figure 3.6:** Resist development profiles of KTI 820 resist a) with a post-exposure bake and b) without a post-exposure bake.

a)

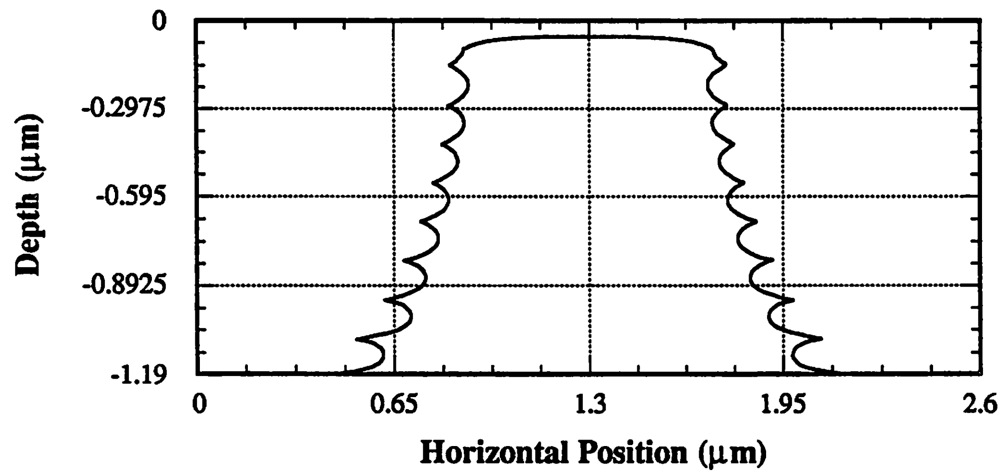


b)

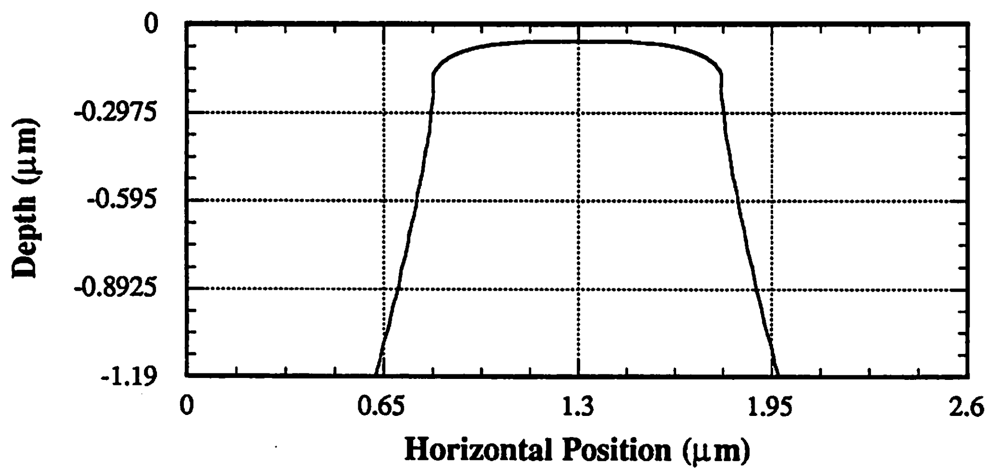

**Figure 3.7:** Development profiles for SNR 248 resist simulated with a) simultaneous diffusion and reaction and b) sequential diffusion and reaction.

a)

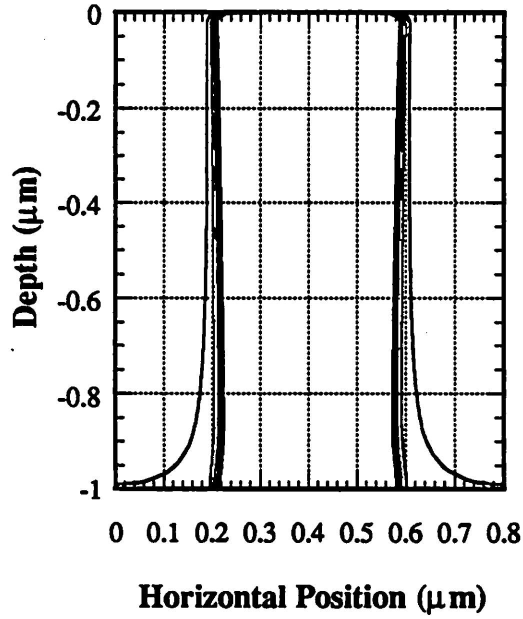


b)

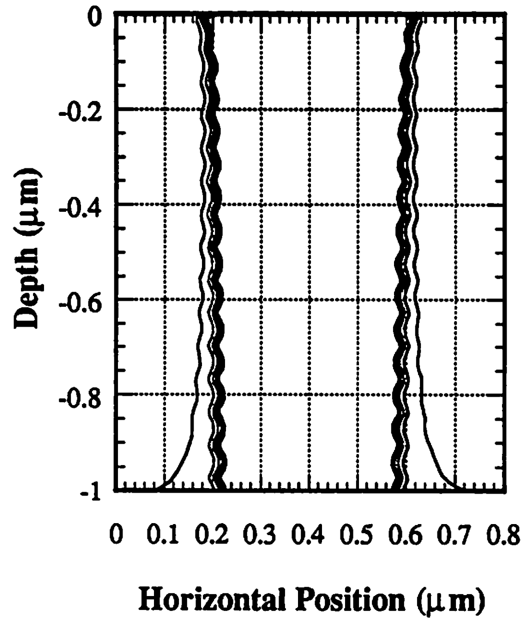

# CHAPTER 4

# EXAMPLES USING *SAMPLE-ARK*

The power and flexibility of the *SAMPLE-ARK* program are demonstrated through the simulation of three advanced resist technologies: image reversal, chemical amplification, and silylation. The general nature of the input description in terms of fundamental chemical and physical mechanisms provides for the investigation of basic issues for each of these three processes. Through the variation of process parameters, resist properties, and the fundamental mechanisms occurring during processing, the importance of *SAMPLE-ARK* as a useful tool in the optimization and comparison of these as well as other complex resist technologies is clearly demonstrated.

## 4.1 INTRODUCTION

The *SAMPLE-ARK* program described in Chapter 3 simulates complex resist processes in terms of the basic chemical and physical mechanisms that determine the resist behavior. Consequently, with this general approach, the program has the breadth needed to simulate a wide spectrum of resist processes without modification to the program code. This flexibility is demonstrated in this chapter through the simulation of three advanced technologies that have received much attention in recent years: image reversal, chemical amplification, and silylation.

## 4.2 IMAGE REVERSAL

### 4.2.1 Chemistry and Processing of Image Reversal Resists

Image reversal was first proposed by Moritz and Paal in 1978 [1]. The image reversal process converts the tone of diazo-type resists from positive to negative. This innovation

allows for the selection of the resist tone based upon the specific mask pattern in use (dark or light field). Near vertical development profiles can be achieved by adjusting the process parameters to balance absorption during exposure with resist development [2]. In addition, image reversal tends to balance the biases associated with the positive resist process. Consequently, optimization of the image reversal process can lead to improved linewidth control [3].

Figure 4.1 depicts a general process flow for image reversal consisting of four basic process steps. In the first step, exposure of the resist converts the photoactive compound (PAC) to indene carboxylic acid (ICA). Since the PAC acts as a dissolution inhibitor, development of the resist at this point would produce a positive resist image. However, for image reversal, a bake step follows the exposure which converts the ICA to indene through a base catalyzed reaction [4]. This reaction results from either including a basic additive such as monazoline in the resist itself [1] or by baking the resist in an ammonia atmosphere [5]. The indene also acts as a dissolution inhibitor in aqueous alkaline developer. Therefore, by destroying the remaining PAC during a flood exposure, development of the resist occurs only in the unexposed regions of the resist leading to a negative-tone resist process.

#### 4.2.2 Simulation of Image Reversal Resists

A standard positive resist process will result when the post-exposure bake and flood exposure steps are not included. Simulation of this case provides a useful comparison for the image reversal process. Figure 4.2 shows simulated resist profiles for several development times using a 0.8 μm equal lines and spaces mask pattern (0.8λ/NA) with g-line exposure. This simulation was performed using the standard exposure and development routines in ***SAMPLE*** (see Chapter 2). The region in the center of Figure 4.2 where the resist remains corresponds to the dark area or the line on the mask. The sloped sidewalls are typical of a positive resist process.

Figure 4.3 shows an example input file for the simulation of an image reversal process. The sections of Figure 4.3 that define the exposure, bake, and development of the resist are clearly indicated.† By assuming that the flood exposure completely destroys all remaining PAC within the resist, simulation of this process step is not required. The model for the post-exposure bake in Figure 4.3 assumes that the conversion of indene carboxylic acid to indene goes to completion during the bake. In other words, the normalized concentration of indene is related to the photoactive compound concentration by:

$$[\text{Indene}] = 1 - [\text{PAC}] \qquad [5.1]$$

The **initialize** command is used in the input file of Figure 4.3 to perform this simple calculation. The matrix containing the indene concentration is then returned to the standard *SAMPLE* dissolution routine with the **return** command. Since the indene acts as a dissolution inhibitor in a similar manner to the PAC, Dill's development model (see Chapter 2) is used to describe the resist dissolution in terms of the normalized indene concentration.‡

The simulation results from the input file of Figure 4.3 are shown in Figure 4.4. The 0.8 μm mask pattern used previously for simulation of the standard positive resist process is once again used to generate the image reversal development profiles. The resist remains where exposed thus producing a negative tone image of the mask pattern. Since absorption during exposure tends to balance the dissolution properties, the image reversal process produces a steeper sidewall angle in comparison to Figure 4.2 with a slight inversion in the profile shape. While this simulation provides valuable qualitative information, a more complete evaluation of the exposure and development parameters is still needed in order to perform a full simulation study of this image reversal process.

---

†. Refer to the *SAMPLE* manual for a complete description of the standard *SAMPLE* commands.

‡. Since no known dissolution rate parameters describing an image reversal process were available, as an approximation, the parameters from the positive resist process shown earlier were used.

The example of Figure 4.4 assumes the complete conversion of ICA to indene during the post-exposure bake. However, *SAMPLE-ARK* provides the means for examining the case in which an insufficient bake results in this reaction not reaching completion. Figure 4.5 shows an example input file for addressing this issue. A single chemical reaction, defined by the **reaction** command, describes the production of indene during the post-exposure bake. In this reaction, the reaction rate coefficient has been chosen in conjunction with the bake time such that only 86% of the ICA is converted to indene.

This *SAMPLE-ARK* input file produces the development profiles shown in Figure 4.6. A comparison of these development profiles with Figure 4.4 indicates that the space width increases as a result of the incomplete conversion of ICA to indene. This increase occurs because less indene is present in the resist following the bake to inhibit the resist dissolution. In this case, in order to equalize the line and space widths, a higher exposure dose is needed. However, while the incomplete conversion during the bake does cause a loss in sensitivity, the resist sidewall angle remains essentially constant. The sidewall angle does not change because the indene concentration is reduced by the same amount (in this case 14%) at every point in the resist.

### 4.3 CHEMICAL AMPLIFICATION

Reduction of the exposure wavelength in photolithography can lead to an increase in resolution. However, as the trend in lithography continues towards deep-UV wavelengths (248 and 193 nm for example), new resist materials and techniques are required to overcome the high absorption and low sensitivity of diazo-type resists. With the use of a novel approach commonly referred to as chemical amplification, several resists have demonstrated sensitivities less than 50 mJ/cm$^2$ in the deep-UV [6]-[8].

### 4.3.1 Chemistry and Processing of Chemical Amplification Resists

All chemical amplification resists rely on the same basic principles. Exposure of the resist produces an acid through a photolytic reaction. This photo-generated acid catalyzes a second chemical reaction during the subsequent post-exposure bake.† The extent of this bake reaction determines the dissolution rate during development. The nature of the catalytic reaction during the bake and the developer type fix the tone of the resist (positive or negative). Figure 4.7 demonstrates a general process flow for a chemical amplification resist consisting of the exposure, post-exposure bake, and development steps.

Two distinct classes of chemical amplification resists have received a considerable amount of attention. The first type of chemical amplification resist, referred to as an acid hardening resist, relies on an acid catalyzed crosslinking reaction during the post-exposure bake to achieve a highly-sensitive, negative-tone resist [6]. In a second class of chemical amplification resists, the photo-generated acid catalyzes the removal of a t-BOC protecting group from a poly(t-BOC styrene) resin [7][8]. With the removal of the protecting group, the resist becomes soluble in aqueous alkaline developer and thus acts as a positive-tone resist process. A thorough description of both the chemistry and the modeling of these two types of chemical amplification resists is presented in Chapters 6 and 7. The following section demonstrates the simulation of a chemical amplification resist with ***SAMPLE-ARK*** using a simple generic example.

†. In a pure catalytic reaction, the catalyst increases the rate of the reaction without undergoing any permanent chemical change.

### 4.3.2 Simulation of Chemical Amplification Resists

The catalytic reaction during the post-exposure bake provides the foundation for the chemical amplification process. For illustrative purposes, this section assumes a simple catalytic reaction given by:

$$acid + A \rightarrow B + acid \quad [5.2]$$

In this reaction, the photo-generated acid catalyzes the conversion of species A to species B. The concentration of the acid remains unaffected as expected for a catalytic reaction.† By assuming that species A acts as a dissolution inhibitor, then the destruction of A during the bake causes the resist to develop in the regions where exposed resulting in a positive-tone resist process.

Dill's ABC model [9] can be used to simulate the generation of acid during the exposure through a simple photolytic reaction. For the actual acid generators studied, the exposure dose required to completely convert the acid generator to acid is much larger than typical operating doses (see Chapter 7). Therefore, the local concentration of acid is expected to be linearly proportional to the absorbed exposure energy. This situation can be simulated by choosing a small value for the rate coefficient of acid generation, C (in this case C = 0.001 $mJ/cm^2$).

Figure 4.8 shows an example ***SAMPLE-ARK*** input file used to simulate a chemical amplification resist with the above assumptions. In this input file, the **reaction** command specifies the catalytic reaction of equation [5.2] while the **return** command sends the concentration matrix of the dissolution inhibitor, A, to the ***SAMPLE*** dissolution routine for development. Figure 4.9 shows the resulting development profile obtained when using an exposure dose of 50 $mJ/cm^2$ and a bake time of 10 seconds.

---

†. Chapters 6 and 7 provide examples in which the acid is actually consumed in an alternate reaction during the bake.

An increase in the bake time drives the catalytic reaction of equation [5.2] further towards completion. Therefore, by increasing the bake time, higher sensitivity can be obtained from this chemical amplification process. It is easily shown that for this simple example the dose scales with the bake time according to expression:

$$D \propto \frac{1}{t} \qquad [5.3]$$

where D is the exposure dose and t is the bake time. According to equation [5.3], if an increase of 5 in the sensitivity is needed, the bake time must also be increased by a factor of 5. Figure 4.10 shows the resulting development profile obtained using the same chemical amplification process as in Figure 4.9, but with a reduced exposure dose of 10 $mJ/cm^2$ and a bake time of 50 seconds. While the sensitivity increased by a factor of 5, the development profile remained essentially identical. This result indicates that by taking advantage of the catalytic bake reaction, chemical amplification processes can achieve a high sensitivities without affecting the resist contrast.†

## 4.4 SILYLATION

### 4.4.1 Chemistry and Processing of Silylated Resists

In a silylation process, silicon-containing compounds are selectively introduced into the resist following exposure [10]. During a subsequent oxygen plasma etch or dry development, the silicon forms an $SiO_2$ barrier which prevents further etching. Therefore, the resist remains in the regions containing silicon. Figure 4.11 depicts a general process flow for a silylation process. Because only a thin layer of silicon-containing resist is required at the resist surface to obtain selectivity during the etch, this type of process is often referred to as a surface imaging resist. Consequently, since only the surface of the resist requires

†. Eventually, the resist contrast will be limited by lateral diffusion of the acid during the bake.

exposure, this type of process can lead to improved depth-of-focus as well as higher tolerance to substrate topography and reflectivity.

The incorporation of silicon in the resist depends upon the diffusion of the silylating agent into the resist followed by the reaction of the agent with the phenolic group of the resin. Two basic methods based upon these mechanisms exist for achieving selective silicon uptake. In the first method, the diffusion coefficient of the silylating agent in the resist is modified through exposure [10]-[13]. Much work has been done in studying the mechanisms involved in this diffusion-controlled process [14]-[17]. A second approach relies on the variation in the availability of the phenolic sites to obtain selectivity. This can be achieved through the chemically amplified removal of a t-BOC group from poly(para-hydroxy styrene)-based resins [18][19]. The ***SAMPLE-ARK*** program, as demonstrated in the following section has the capability to simulate both of these basic silylation processes.

#### 4.4.1.1 Simulation of Silylated Resists

A complete simulation of a silylation process would consist of simulating the exposure, the silicon uptake during the bake, and the oxygen plasma dry development. Simulation of the site-controlled silylation processes must also include the post-exposure bake in which the deprotection reaction creates the phenolic sites on the resin. Currently, the **SAMPLE** etch routine cannot incorporate position-dependent etch rate models necessary for simulating the dry development step. In addition, quantitative models describing the oxygen plasma etch are lacking. For these reasons, the results presented in this section are shown in terms of the silicon uptake during the post-exposure processing. While this approach does not lead to the simulation of the final resist images, good qualitative information can nonetheless be obtained.

In the first basic type of silylation process, exposure of the resist modifies the diffusion coefficient of the silylating agent resulting in selective silicon uptake. The DESIRE process using the Plasmask resist was the first commercially available silylation process based upon this approach [11]. Bauch *et al.* have shown that the diffusion coefficient in the Plasmask resist is related to the PAC concentration by:

$$D(M) = 3.5 \cdot \exp\left[\frac{1-M}{0.1414}\right] \ \mathrm{nm^2/sec} \qquad [5.4]$$

where D is the diffusion coefficient and M is the normalized concentration of PAC [17].

Figure 4.12 shows an input file in which silicon is incorporated into the resist based upon equation [5.4]. The resist is exposed at 248 nm with a 0.5 μm equal lines and spaces pattern (0.8λ/NA). The **diffuse** command specifies the dependence of the diffusion coefficient on the PAC concentration while the **diffsource** command alters the surface boundary conditions such that the diffusion occurs from an outside source (see Chapter 3). This input file does not take into account the reaction of the silylating agent with the available phenolic sites on the resin which is assumed to be rapid in comparison with the diffusion process. Figure 4.13 shows the contours of relative silicon concentration in the resist as a result of using the input file of Figure 4.12 in ***SAMPLE-ARK***. The exposure occurred in the center of the plot which enhanced the diffusion coefficient of the silylating agent resulting in increased silicon uptake. If an oxygen plasma etch followed this bake step, the resist would remain in the regions of high silicon uptake producing a resist profile in the center of the plot.

In the second type of silylation process, the selective incorporation of silicon into the resist occurs through a variation in the number of reactive sites as a result of a chemically amplified deprotection reaction prior to the silylation step. Spence *et al.* have shown that, in this case, the silylating agent diffuses rapidly through the resist to react with all available phenolic sites [19]. Therefore, in order to simulate this type of silylation process, only the

acid catalyzed removal of the t-BOC protecting group needs to be considered. As a result, the input description for this type of silylation process in ***SAMPLE-ARK*** is similar to the input file shown in Figure 4.8 for the chemical amplification example. Chapter 7 provides a complete description of the modeling process for t-BOC chemical amplification resists.

Figure 4.14 shows the contours of relative silicon concentration for this site-controlled silylation process. Once again, the resist is exposed at 248 nm with a 0.8λ/NA equal lines and spaces mask pattern. The largest amount of available phenolic sites occurred in the center of the plot where the acid catalyzed deprotection reaction was driven further towards completion. In this case, because of the resin transparency, the silicon uptake extends throughout the resist thickness as compared to Figure 4.13. This uniformity tends to increase the sensitivity to substrate topography and reflectivity and thus does not lead to a surface imaging resist process. However, by increasing the resin absorption or by including a dye in the resist, the affect of the substrate on the silicon uptake can be significantly reduced. Figure 4.15 shows the resulting silicon concentration contours for a 390% increase in the absorption coefficient. In this example, the silicon concentration no longer extends uniformly throughout the resist thickness. Consequently, the final developed resist images will have less dependence upon the underlying substrate. The examples demonstrated for both the diffusion and site-controlled silylating resists indicates that ***SAMPLE-ARK*** provides an excellent tool for comparing the fundamental resolution and process latitude of these two basic silylation processes.

## 4.5 SUMMARY

***SAMPLE-ARK*** has been used to simulate image reversal, chemical amplification, and silylation resist processes. This simulation capability has been used to explore some key issues that determine the resist performance. The processes were described in the program in terms of the fundamental chemical and physical mechanisms which determine the resist

behavior during each individual process step. Changes to both the process parameters as well as to the overall process description have lead to an additional understanding of the factors that affect important performance criteria such as resolution and sensitivity.

For image reversal, the use of an additional post-exposure bake and flood exposure leads to the reversal of the resist tone as well as an increase in sidewall angle. Incomplete conversion of ICA to indene during the bake reduces the sensitivity of the image reversal process, but does not affect the resist resolution. In chemical amplification, the trade-offs between the exposure and bake have been explored. When a simple catalytic reaction occurs during the bake, the sensitivity scales directly with the bake time. The silicon uptake for both a diffusion and a site-controlled silylation process have been compared. Further study with ***SAMPLE-ARK*** can lead to a more complete understanding of the benefits and drawbacks of each basic process type.

## REFERENCES


[1] H. Moritz and G. Paal, U.S. Patent 4 104 070, 1978.

[2] H. Klose, R. Sigush, and W. Arden, "Image Reversal of Positive Photoresist: Characterization and Modeling," IEEE Trans. Electron Devices, vol. ED-32, no. 9, pp. 1654-1661, September 1985.

[3] R. Gijsen, H. Kroon, F. Vollenbroek, and R. Vervoordeldonk, "A Quantitative Assessment of Image Reversal, A Candidate for a Submicron Process with Improved Linewidth Control," *Proceedings SPIE: Advances in Resist Technology and Processing III*, vol. 631, pp. 108-116.

[4] S. MacDonald, R. Miller, C. Willson, G. Feinberg, R. Gleason, R. Halverson, W. McIntire, M. Motsiff, Kodak Microelectronics Seminar - Interface '82, San Diego, CA, 1982.

[5] D. Ziger and J. Reightler, "Analysis of Processing Factors Affecting Ammonia Catalyzed Image Reversal," *KTI Microelectronics Seminar - Interface '87*, pp. 13-25, 1987.

[6] J. Thackeray, G. Orsula, E. Pavelchek, D. Canistro, L. Bogan, A. Berry, and K. Graziano, "Deep UV ANR Photoresists for 248 nm Excimer Laser Photolithography," *Proceedings SPIE: Advances in Resist Technology and Processing VI*, vol. 1086, pp. 34-47, 1989.

[7] C. Willson, H. Ito, J. Frechet, T. Tessier, and F. Houlihan, "Approaches to the Design of Radiation-Sensitive Polymeric Imaging Systems with Improved Sensitivity and Resolution," *J. Electrochem. Soc.*, vol. 133, no. 1, pp. 181-187, January 1986.

[8] R. Tarascon, E. Reichmanis, F. Houlihan, A. Shugard, and L. Thompson, "Poly(t-BOC-styrene sulfone)-Based Chemically Amplified Resists for Deep-UV Lithography," *Polymer Engineering and Science*, vol. 29, no. 13, pp. 850-855, Mid July, 1989.

[9] F. Dill, W. Hornberger, P. Hauge, and J. Shaw, "Characterization of Positive Photoresist," *IEEE Trans. Electron Devices*, vol. ED-22, no. 7, pp. 445-452, July 1975.

[10] G. Taylor, L. Stillwagon, and T. Venkatesan, "Gas-Phase Functionalized Plasma-Developed Resists: Initial Concepts and Results for Electron-Beam Exposure," *J. Electrochem. Soc.* vol. 131, p. 1658, 1984.

[11] F. Coopmans and B. Roland, "DESIRE: A Novel Dry Developed Resist System," *Proceedings SPIE: Advances in Resist Technology and Processing III*, vol. 631, pp. 34-39, 1986.

[12] M. Hartney, R. Kunz, D. Ehrlich, and D. Shaver, "Silylation Processes for 193-nm Excimer Laser Lithography," *Proceedings SPIE: Advances in Resist Technology and Processing VII*, vol. 1262, pp. 119-130.

[13] E. Pavelchek, J. Bohland, J. Thackeray, and G. Orsula, "Silylated Acid Hardened Resist Process - A Deep Ultraviolet Surface Imaging Technique," *J. Vac. Sci. B*, vol. 8, no. 6, pp. 1497-1501, Nov/Dec 1990.

[14] R. Visser, J. Schellekens, M. Reuhman-Huisken, and L. Van Ijzendoorn, "Mechanism and Kinetics of Silylation of Resist Layers from the Gas Phase," *Proceedings SPIE: Advances in Resist Technology and Processing IV*, vol. 771, pp. 111-117, 1987.

[15] B. Roland, J. Vandendriessche, R. Lombaerts, B. Denturck, and C. Jakus, "Thermal Crosslinking by Unexposed Naphthoquinone Diazides as Diffusion Inhibition Mechanism in the DESIRE Process," *Proceedings SPIE: Advances in Resist Technology and Processing V*, vol. 920, pp. 120-127, 1988.

[16] G. Misium, M. Douglas, C. Garza, and C. Dobson, "Silicon Diffusion Characteristics of Different Surface Imaging Resists," *Proceedings SPIE: Advances in Resist Technology and Processing VII*, vol. 1262, pp. 74-83, 1990.

[17] L. Bauch, U. Jagdhold, H. Dreger, J. Bauer, W. Hoppner, and J. Erzgraber, "Surface Imaging on the Basis of Phenolic Resin - Experiments and Simulation," *Proceedings SPIE: Advances in Resist Technology and Processing VIII*, vol. 1466, 1991.

[18] S. MacDonald, H. Ito, H. Huraoka, and C. Willson, "A New Oxygen Plasma-Developable UV-Sensitive Resist," *SPE Proceedings Tech. Conf. Photopolymers - Principles, Processes, and Materials*, p. 177, 1985.

[19] C. Spence, S. MacDonald, and H. Schlosser, "Silylation of Poly (t-BOC) Styrene Resists: Performance and Mechanisms," *Proceedings SPIE: Advances in Resist Technology and Processing VII*, vol. 1262, pp. 344-357, 1990.

**Figure 4.1:** A general process flow for an image reversal resist process.

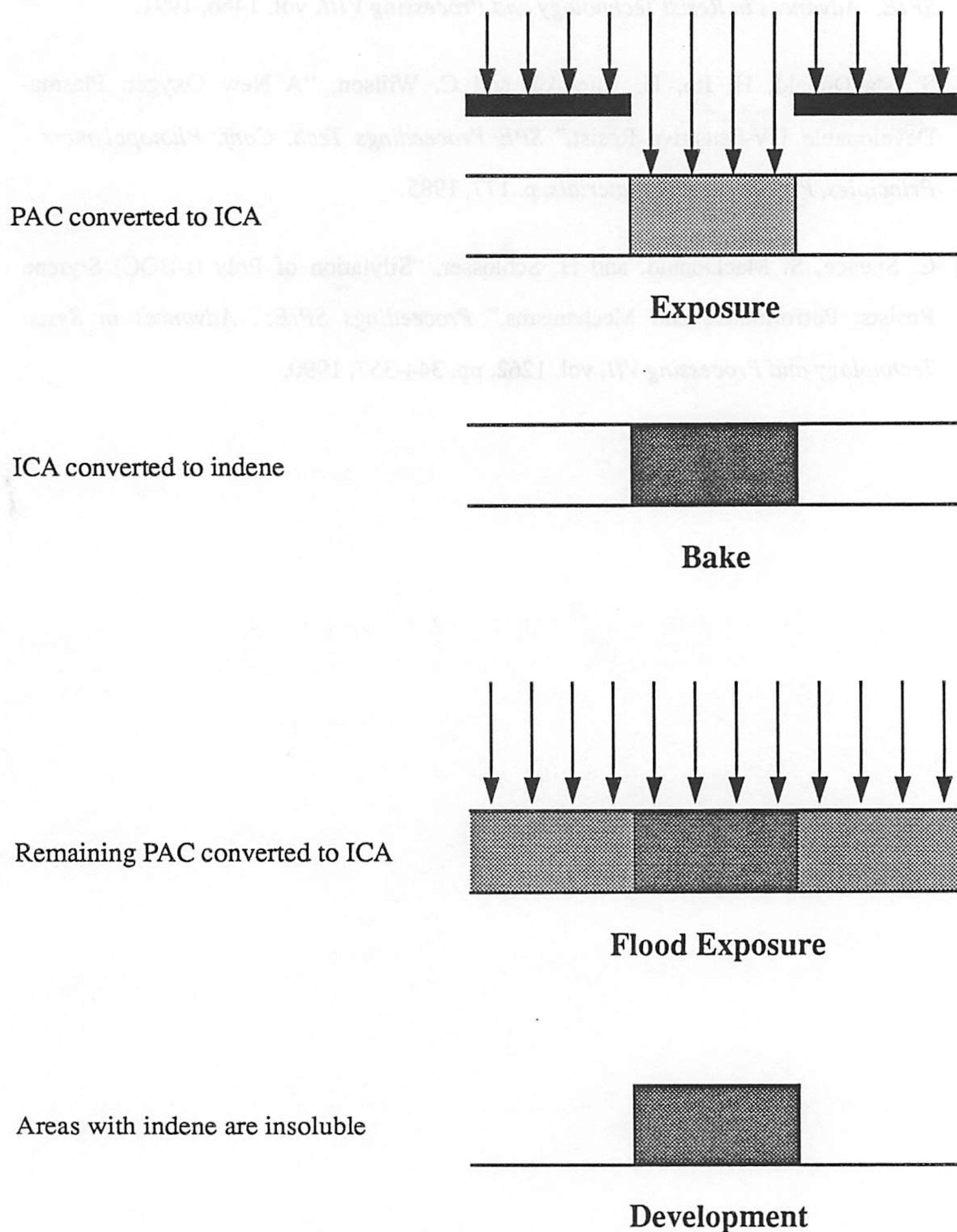

**Figure 4.2:** Resist development profiles for a standard positive resist without image reversal.

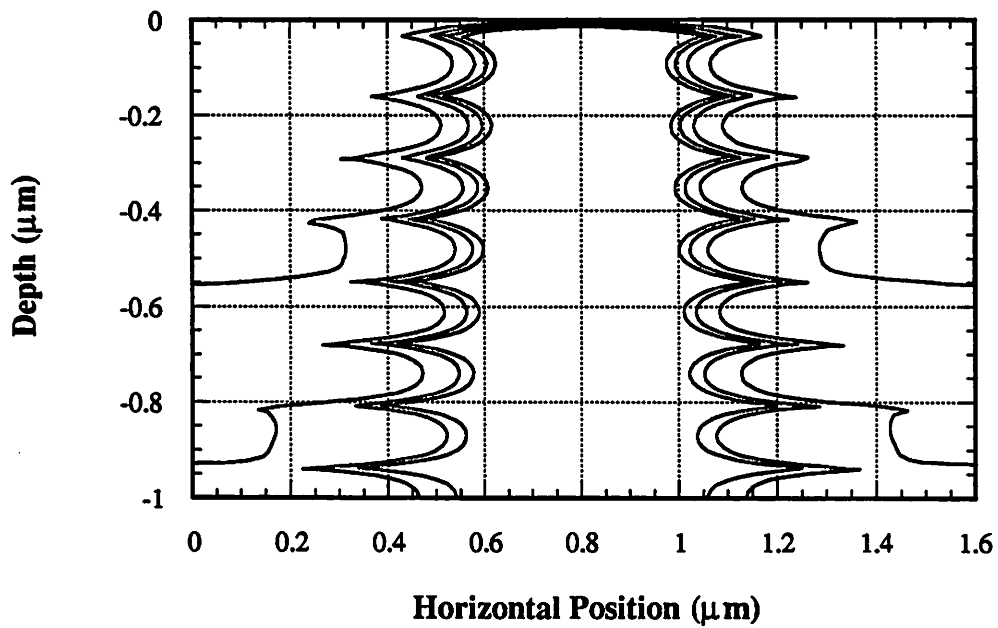

**Figure 4.3:** *SAMPLE-ARK* input file for an image reversal process with complete conversion of ICA to indene during the post-exposure bake.

```
lambda 0.4358                              ;  \
proj 0.42                                  ;   |
linespace 0.80 0.80                        ;   |
parcohdef 0 0.7 0.0                        ;   |
horwindow 1.6 1.2                          ;   |
imagerun                                   ;   |
resmodel ((0.4358))                            |
         (0.551, 0.058, 0.010)                  >  Exposure
         (1.68, ((-0.02))) (1.0000)        ;   |
layers (4.73,-0.136)                           |
     (1.47,0.0,0.0741)                     ;   |
dose 2000†                                 ;   |
exposerun                                  ;  /
startbake                                  ;  \
initialize indene expose_inv 1             ;   |
return indene                              ;    >  Bake
endbake                                    ;  /
heatdiffus 0.02 1                          ;
devrate 1 (5.63, 7.43, -12.6)              ;  \
devtime 15 60 4                            ;    >  Development
developrun                                 ;  /
```

†. Image reversal typically requires higher doses than standard diazo-type resists.

**Figure 4.4:** Resist development profiles for an image reversal process using the input file in Figure 4.4.

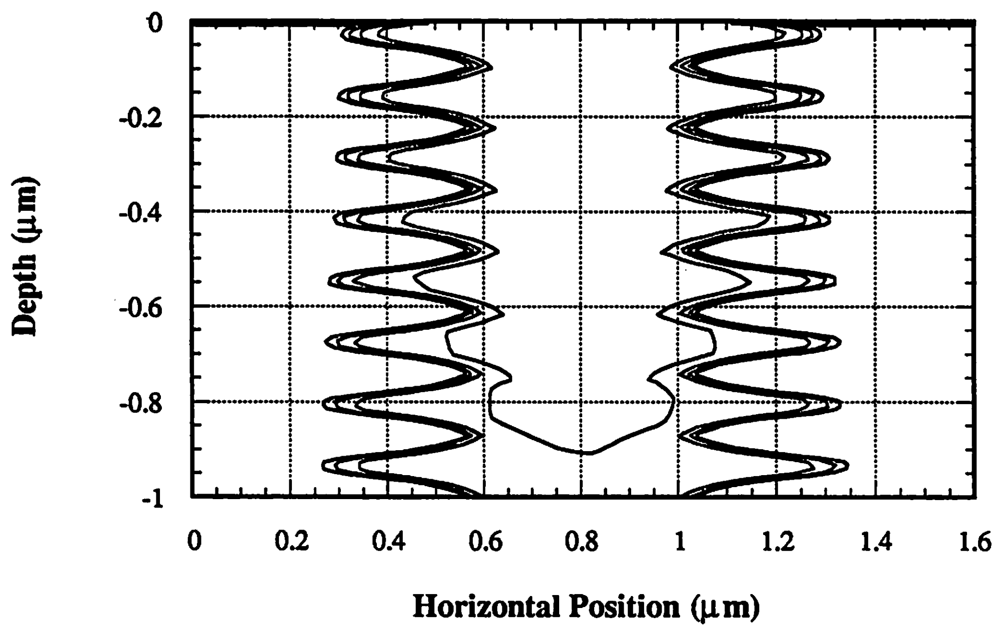

**Figure 4.5:** ***SAMPLE-ARK*** **input file for an image reversal process with incomplete conversion of ICA to indene during the post-exposure bake.**

```
lambda 0.4358                                  ;  )
proj 0.42                                      ;  |
linespace 0.80 0.80                            ;  |
parcohdef 0 0.7 0.0                            ;  |
horwindow 1.6 1.2                              ;  |
imagerun                                       ;  |
resmodel ((0.4358))                               |
          (0.551, 0.058, 0.010)                   > Exposure
          (1.68, ((-0.02))) (1.0000)           ;  |
layers (4.73,-0.136)                              |
     (1.47,0.0,0.0741)                         ;  |
dose 2000                                      ;  |
exposerun                                      ;  )
startbake                                      ;  )
time 2                                         ;  |
reaction k = 1 in = ica out = indene           ;  |
initialize ica expose_inv 1                    ;  > Bake
initialize indene 0                            ;  |
bake                                           ;  |
return indene                                  ;  |
endbake                                        ;  )
heatdiffus 0.02 1                              ;
devrate 1 (5.63, 7.43, -12.6)                  ;  )
devtime 15 60 4                                ;  > Development
developrun                                     ;
```

**Figure 4.6:** Resist development profiles for an image reversal process using the input file from Figure 4.5.

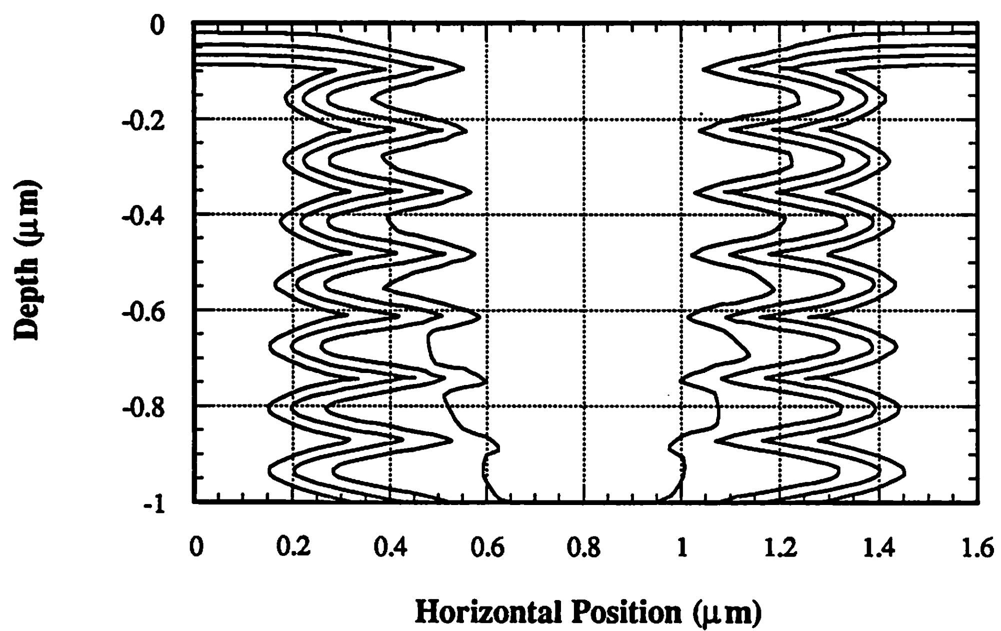

**Figure 4.7:** A general process flow for a chemical amplification resist.

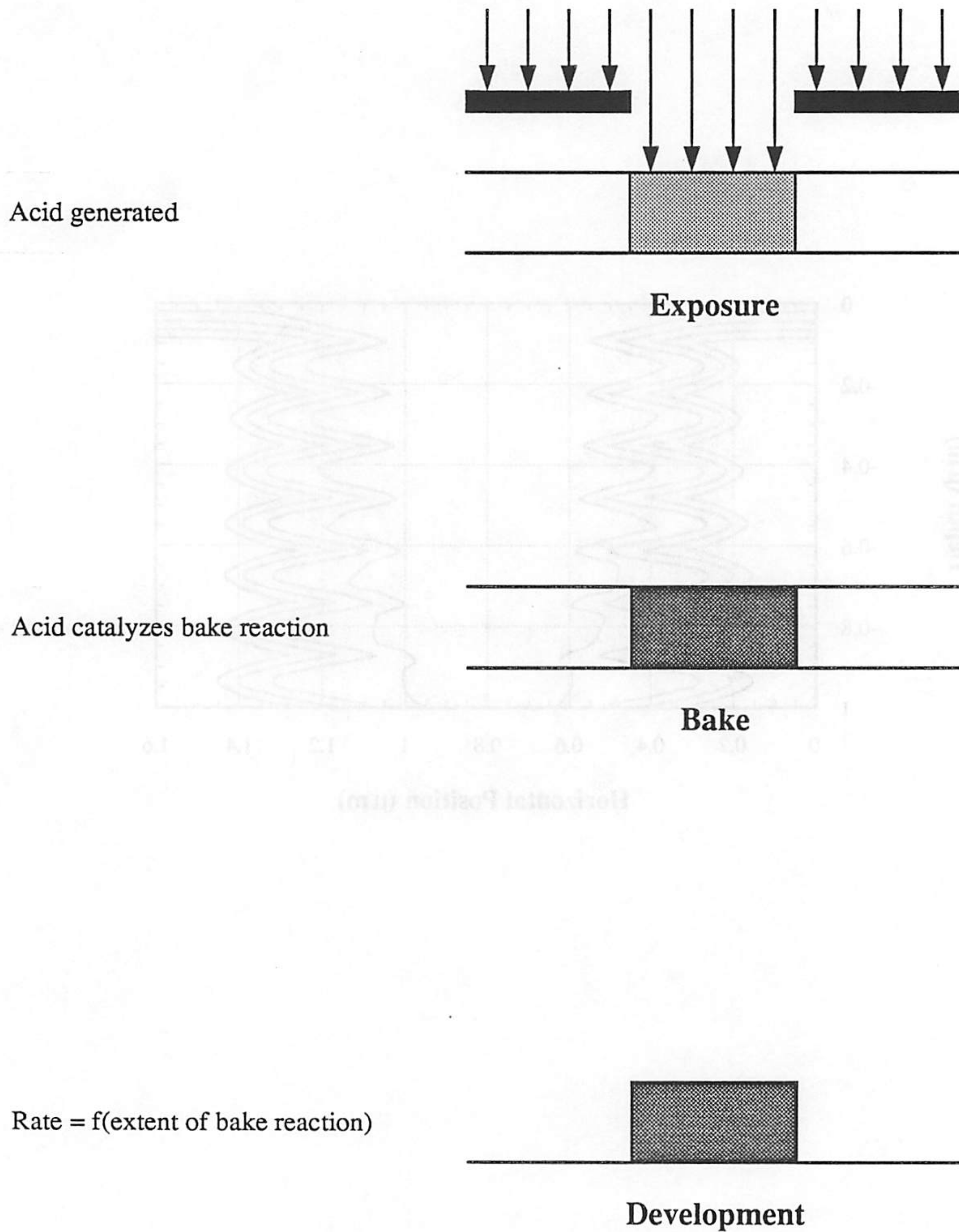

**Figure 4.8:** A *SAMPLE-ARK* input file for a chemical amplification resist.

```
lambda 0.248                                          ;  \
proj 0.42                                             ;   |
linespace 0.5 0.5                                     ;   |
parcohdef 0 0.5 0.8                                   ;   |
vertrespts 200                                        ;   |
horwindow 1.0 0.75                                    ;   |
imagerun                                              ;   |
resmodel ((0.248))                                        > Exposure
          (0.000, 0.600, 0.001)                           |
       (1.68, ((-0.02))) (1.0000)                     ;   |
layers (1.70,-3.38)                                   ;   |
dose 50.0                                             ;   |
exposerun                                             ;  /
heatdiffus 0.02 1                                     ;  \
startbake                                             ;   |
time 10                                               ;   |
reaction  k = 1.25  in = acid,a  out = b,acid         ;   |
initialize acid expose_inv 1                          ;   > Bake
initialize a 1                                        ;   |
initialize b 0                                        ;   |
bake                                                  ;   |
return a                                              ;  /
endbake                                               ;  \
devrate 1 (5.63, 7.43, -12.6)                         ;   > Development
devtime 60                                            ;  /
developrun                                            ;
```

**Figure 4.9:** Development profile for a chemical amplification resist using the input file in Figure 4.8. The profile was obtained using an exposure dose of 50 mJ/cm$^2$ and a bake time of 10 seconds.

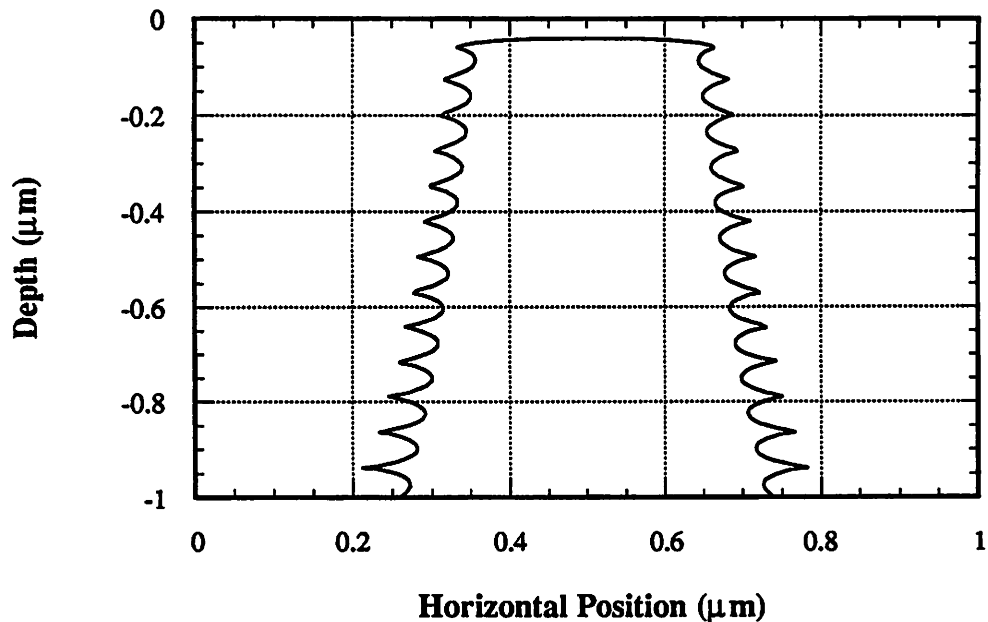


**Figure 4.10:** Development profile for the chemical amplification resist of Figure 4.9, but with an exposure dose of 10 mJ/cm$^2$ and a bake time of 50 seconds.

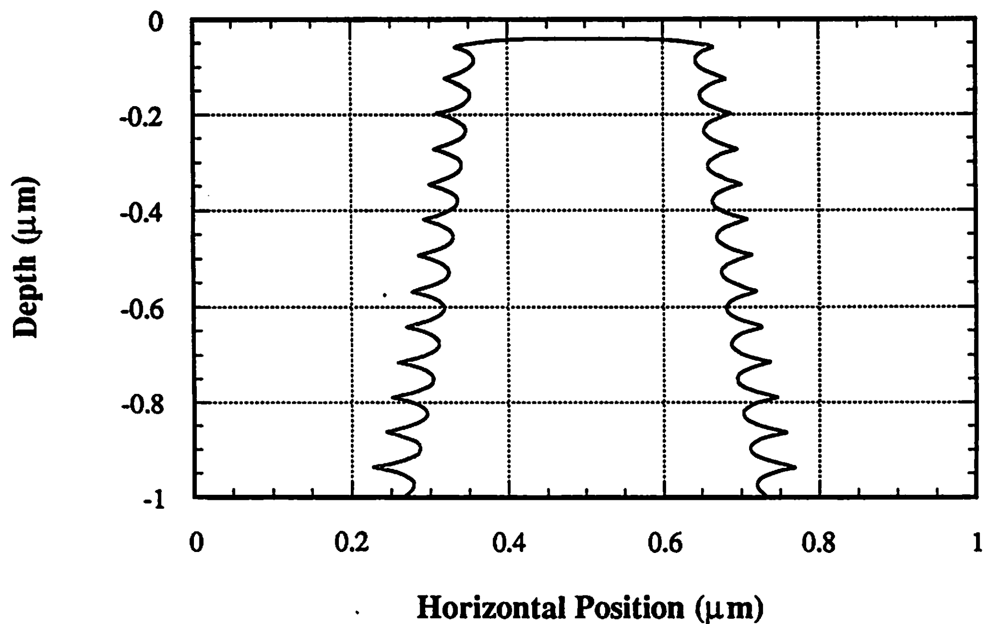

**Figure 4.11:** A general process flow for a silylation process.

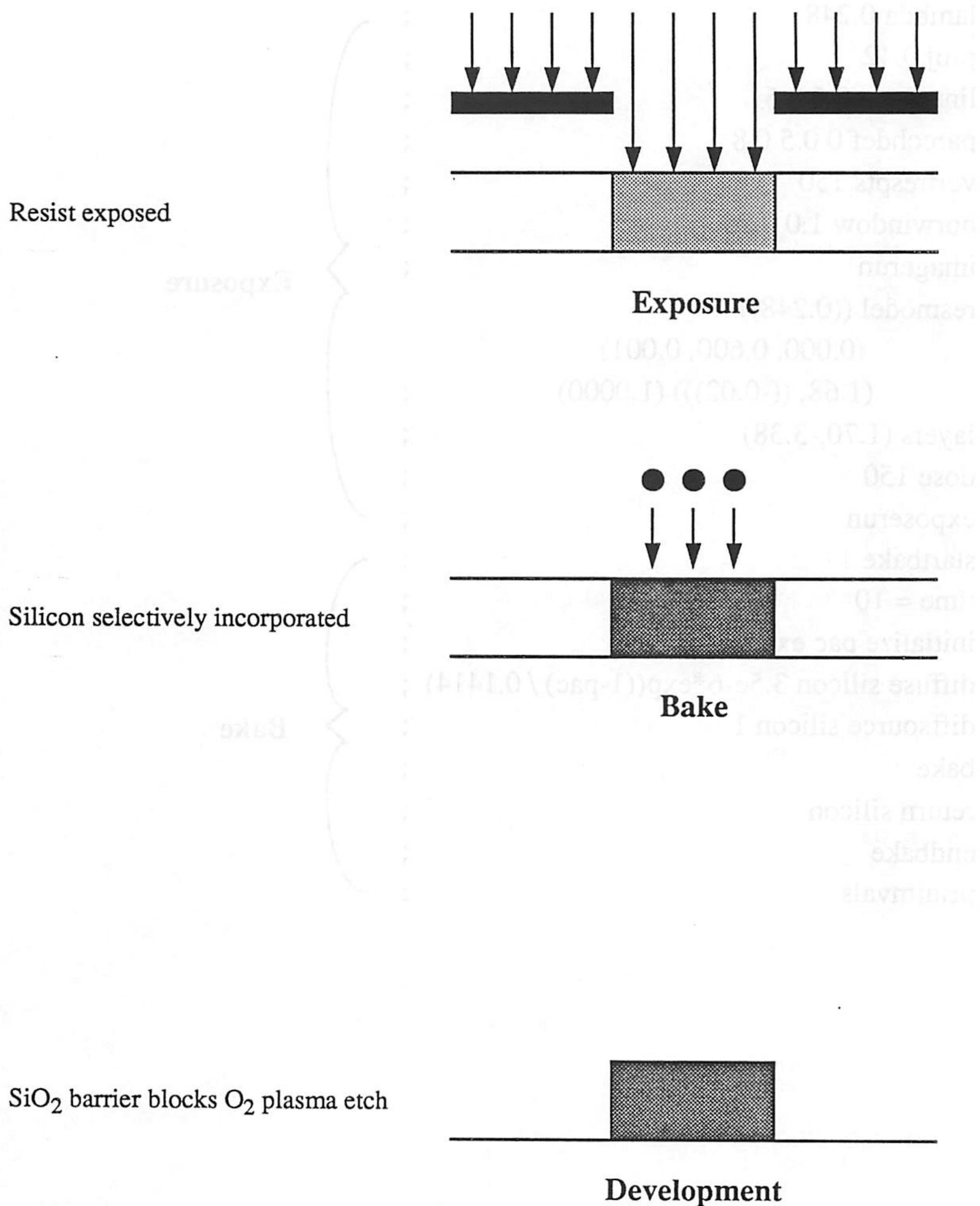

**Figure 4.12:** A *SAMPLE-ARK* input file for a silylation process based upon DESIRE and the Plasmask resist.

```
lambda 0.248                                  ;  \
proj 0.42                                     ;   |
linespace 0.5 0.5                             ;   |
parcohdef 0 0.5 0.8                           ;   |
vertrespts 150                                ;   |
horwindow 1.0 0.25                            ;   |
imagerun                                      ;    > Exposure
resmodel ((0.248))                                |
          (0.000, 0.600, 0.001)                   |
          (1.68, ((-0.02))) (1.0000)          ;   |
layers (1.70,-3.38)                           ;   |
dose 150                                      ;   |
exposerun                                     ;  /
startbake 1                                   ;  \
time = 10                                     ;   |
initialize pac expose 1                       ;   |
diffuse silicon 3.5e-6*exp((1-pac) / 0.1414)  ;   |
diffsource silicon 1                          ;    > Bake
bake                                          ;   |
return silicon                                ;   |
endbake                                       ;   |
printmvals                                    ;  /
```

**Figure 4.13:** Contours of silicon uptake for a diffusion-controlled silylation process based upon DESIRE using the input file of Figure 4.12 in ***SAMPLE-ARK.***

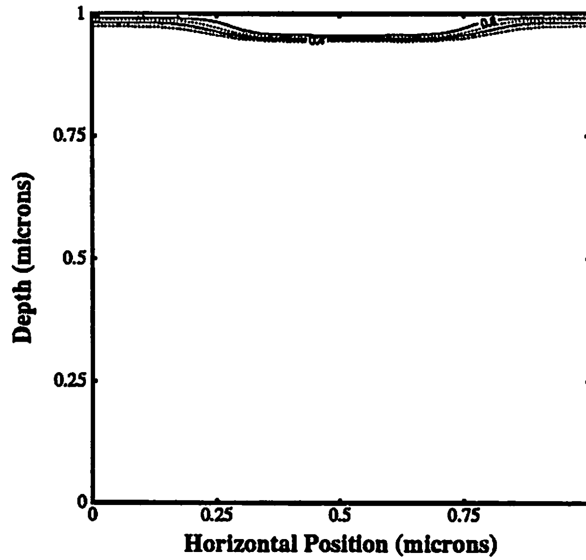


**Figure 4.14:** Contours of silicon uptake for a site-controlled silylation process using a t-BOC chemical amplification.

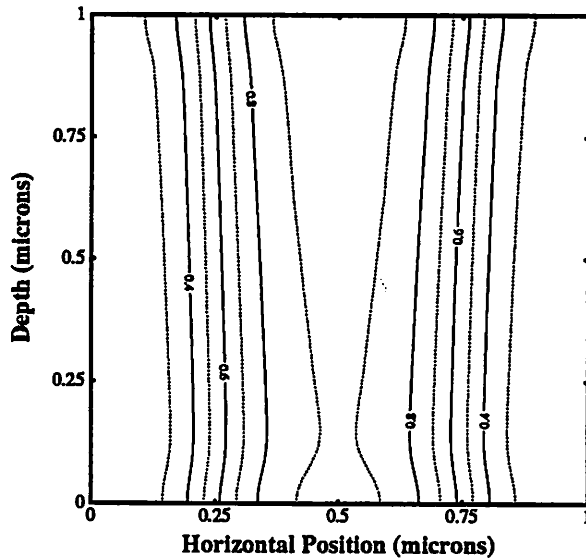

**Figure 4.15:** Contours of silicon uptake for a site-controlled silylation process using a t-BOC chemical amplification with a 390% increase in the resin absorption coefficient.

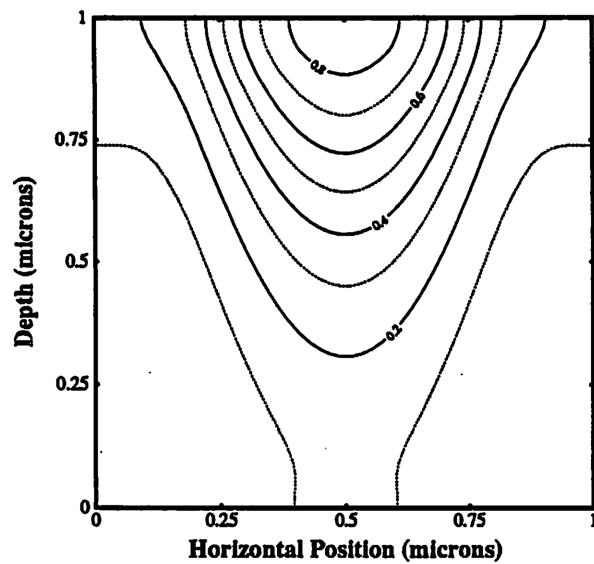

# CHAPTER 5

# CHARACTERIZATION AND MODELING TECHNIQUES

A comprehensive set of materials characterization techniques and modeling software is established in this chapter for the development of mechanistic models describing the behavior of advanced resist technologies. The basic characterization methods proposed in the general methodology of Chapter 2--optical transmission measurements, IR spectroscopy, and interferometry--are refined for use in monitoring the chemical and physical changes that occur during the processing of spin-coated resist materials. Alternative experimental methods are also suggested for increasing data acquisition rates or to provide a supporting role when the basic characterization techniques fail.

Newly developed software tools simplify the generation of mechanistic models from the experimental data. A quantitative FTIR analysis program automates the extraction of chemical species concentrations from characteristic absorption bands in the IR spectrum. Other programs use nonlinear least squares methods to fit kinetic models and to calculate reaction rate coefficients from experimental exposure and bake data.

## 5.1 INTRODUCTION

The collection of reliable quantitative data is essential for developing models that accurately describe the behavior of a resist during processing. With the push to achieve mechanistic models to gain a better understanding of the resist performance, characterization techniques must provide information about the basic chemical and physical changes occurring within the resist during each individual process step.

Several basic requirements have a significant impact on the experimental measurement techniques selected for resist characterization. The use of standard processing procedures (spin-coated resists, for example) during characterization helps ensure that the experimental data are consistent with the actual resist behavior during processing. In addition, in-situ measurement techniques are preferred for their rapid data acquisition rates in real time. Some experimental methods, whether in-situ or not, are desirable because they directly measure specific changes occurring within the resist (such as the concentration of a specific chemical species). These techniques contrast with experimental measurements which establish only an indirect relationship with the specific chemical or physical change of interest. Unfortunately, trade-offs often exist between in-situ data collection and the direct observation of specific resist changes. All of these factors must be balanced during each individual process step in order to achieve an optimized data collection process.

## 5.2 EXPOSURE CHARACTERIZATION AND MODELING

### 5.2.1 Optical Transmission Measurements

Dill's ABC model, as described in Chapter 2, has been used successfully to describe the exposure of diazo-type resists [1]. The Dill model is given by:

$$\alpha(z,t) = AM(z,t) + B \quad [5.1]$$

$$\frac{\partial}{\partial t}M(z,t) = -I(z,t)M(z,t)C \quad [5.2]$$

where $\alpha$ is the absorption coefficient, I is the local illumination intensity, M is the normalized concentration of PAC, z is the depth into the resist, t is the exposure time, A and B are the bleachable and nonbleachable parts of the absorption coefficient, respectively, and C is the bleach rate.

This model actually applies to any simple photolytic reaction in which the rate of the reaction is proportional to the illumination intensity. This simple photolytic reaction is described by:

$$S_1 \xrightarrow{h\nu} S_2 \qquad [5.3]$$

where $S_1$ and $S_2$ are the reactant and product species involved in the reaction. In the generalized Dill model, M represents the normalized concentration of $S_1$† and C becomes the reaction rate coefficient. In fact, this general Dill model can be applied to any system of independent photolytic reactions occurring during the exposure. For example, Shacham-Diamand fit two sets of ABC parameters to the deep-UV transmission of diazo-type resists: one corresponding to the PAC destruction and the other corresponding to resin darkening [2].

The change in the absorption coefficient, as seen in equation [5.1], affects the resist transmission during exposure. Dill *et al.* found that by monitoring the transmission of diazo-type resists, they could determine the extent of PAC destruction that occurred during exposure by fitting the ABC parameters to the experimental results [1]. In theory, this experimental technique also applies to the exposure of more complex resist processes. Based upon this principle, Drako *et al.* devised an experimental system for monitoring resist transmission when using a pulsed excimer laser in the deep-UV at 248 nm [3]. A schematic of the experimental system is shown in Figure 5.1 (other aspects of this system will be described later). To monitor the transmission, the resist is spin coated onto a quartz substrate which is transparent in the deep-UV. The wafer sits on the wafer stage. The detector located behind the quartz wafer monitors the resist transmission. The beam splitter situated in front of the wafer stage sends part of the exposure energy to a second optical detector for use as a reference signal.

†. 1 - M is the concentration of $S_2$.

The quartz substrate plays an important role in the resist transmission measurements. Ideally, the refractive index of the quartz should match with the resist refractive index to prevent reflections of the illumination energy back into the resist material. An anti-refection coating is needed at the quartz/air interface as well to prevent coherent reflections back into the resist.† Figure 5.2a depicts this ideal configuration. Unfortunately, the quartz refractive index does not match typical refractive index values for resists in the deep-UV. For example, while quartz has a refractive index of 1.5 at 248 nm, Shipley SNR 248, a resist for the deep-UV, has a refractive index of about 1.79. In addition, the current quartz wafers used for exposure modeling in Chapters 6 and 7 do not have an anti-reflection coating. Figure 5.2b depicts the realistic configuration of these wafers currently in use for the transmission measurements including reflections from the resist/quartz and the quartz/air interfaces. Fortunately, these reflections can be accounted for when fitting the ABC parameters to the resist transmission (see Section 5.2.2).

Figures 5.3 and 5.4 show experimental transmission results for two different deep-UV resists. Figure 5.3 shows the transmission versus exposure dose for Shipley SNR 248 resist. This chemical amplification resist uses an acid catalyzed crosslinking reaction during the bake to achieve high sensitivity [4] (see Chapter 6 for more details). The catalytic acid is generated upon exposure. The transmission curve of Figure 5.3 show a definite exponential behavior typical of a simple photolytic reaction. However, as will be demonstrated in Chapter 6, the change in transmission results from an alternate reaction in the resist during the exposure, and not the acid generation. Nonetheless, this ABC model does provide a method for modeling both the resist absorption coefficient as well as the local concentration of acid within the resist (see Section 5.2.4).

†. The excimer laser used in this system has a coherence length that is much longer than the quartz substrate thickness.

Figure 5.4 shows the transmission versus exposure dose measurements for a second chemical amplification resist for the deep-UV. In this resist, the photo-generated acid catalyzes the removal of a t-BOC protecting group from the base resin [5]. The unusual behavior of the resist transmission in Figure 5.4 is typical of a resist with multiple photolytic reactions. For this resist, three distinct regions are visible which seems to indicate that at least three chemical reactions occur during exposure. Consequently, in this case, the resist transmission measurements alone do not provide sufficient information to determine which region of the curve corresponds to the acid generation reaction (see Section 5.2.3).

### 5.2.2 Fitting the ABC Model

The ABC parameters are determined from the transmission data. Numerical techniques are required to perform the fitting because of the complications resulting from the interface reflections depicted in Figure 5.2b. As a result, a program that uses a nonlinear least squares fitting algorithm [6] has been developed to determine the ABC parameters. The program has its basis in the ***SAMPLE*** exposure routine [7]. This routine, described in Chapter 2, determines the intensity and the subsequent PAC distribution throughout the resist as the exposure progresses. The input to the program includes both the refractive index of the resist and the quartz substrate. By summing the energy absorbed throughout the entire resist thickness, the transmission for a given set of ABC parameters is easily calculated. The nonlinear fitting routine proposed by Marquardt [8] iterates to find the ABC parameters that minimize the mean square error. Figure 5.5 shows the fit obtained with this program to the transmission data for the SNR 248 resist. The best fit to the data occurred using $A = -0.71\ \mu m^{-1}$, $B = 1.16\ \mu m^{-1}$, and $C = 0.0023\ cm^2/mJ$.

The program can also fit to the transmission data for resists in which multiple chemical reactions occur simultaneously. However, the uniqueness of the fitted parameters may depend on the specific nature of the transmission curve and needs further examination.

Figure 5.6 shows the results obtained from fitting two sets of ABC parameters to the t-BOC transmission curve of Figure 5.4. The initial decrease in transmission was not included in the fit because the changes occurred too rapidly for accurate simulation of the transmission within a reasonable time period. The best fit occurred with $A_1 = 0.38\ \mu m^{-1}$, $B_1 = 0.68\ \mu m^{-1}$, $C_1 = 0.0044\ cm^2/mJ$, $A_2 = -0.38\ \mu m^{-1}$, $B_2 = 0.57 \mu m^{-1}$, and $C_2 = 9.3 \times 10^{-4}\ cm^2/mJ$.

When using this program, any number of the parameters may be held constant during the fitting. The usefulness of this feature was demonstrated for a second version of the t-BOC resist using an onium salt as the acid generator. In this resist, the ABC parameters associated with the resin alone were held constant when determining the parameters for the acid generation reaction. This approach is described in more detail in Chapter 7.

### 5.2.3 FTIR Spectroscopy Measurements

The optical transmission measurements provide only an indirect measure of the exact chemical changes occurring within the resist. In some resists, such as the t-BOC resist with the corresponding transmission curve of Figure 5.4, a more direct method is needed for the individual measurement of the multiple photolytic reactions during exposure. One such method, Fourier transform infrared (FTIR) spectroscopy, has the capability to perform this differentiation. The peaks obtained in an IR spectrum correspond to the vibrational frequencies of specific bonds within the resist material. The position, height, and shape of these peak are determined by the specific chemistry of the bond, the number of bonds present, and the local chemical and physical environment. By determining the size of a peak, the number of bonds and thus the concentration of a given chemical species can be quantified.

The diagram of Figure 5.1 includes the configuration of the FTIR measurement system. The FTIR system scans over a range of wavelengths from 2.5 μm to 25 μm.† The resist

sample is located on the wafer stage. This stage can be moved to allow for the measurement of various locations on the same sample. The entire experimental system of Figure 5.1 was enclosed in a plexiglass box to control the atmospheric environment. The samples are prepared by spin coating the resist on a silicon wafer. Since silicon is transparent in the IR, these samples can be measured in the transmission mode. The silicon wafers are polished on both sides to reduce the scattering associated with surface roughness.

The t-BOC resist that produced the transmission curve of Figure 5.4 provides an example of the successful use of FTIR spectroscopy in the monitoring of resist exposure. In this resist, the transmission curve of Figure 5.4 provides no particular information about the rate of acid generation. However, the FTIR difference spectrum of Figure 5.7 taken before and after exposure shows a distinct peak at 1540 $cm^{-1}$ which was attributed to the acid generation reaction. By measuring the size of this peak at various exposure doses, the concentration of acid, and thus the rate coefficient of acid generation, $C = 0.0045$ $cm^2/mJ$, was determined as shown in Figure 5.8. FTIR spectroscopy, however, does not provide a foolproof method for monitoring the resist exposure. In both the Shipley SNR 248 resist and in the t-BOC resist with the onium salt acid generator, no discernible peaks in the FTIR spectrum could be attributed to the acid generation reaction.

### 5.2.4 Comments on the Exposure of Chemical Amplification Resists

The experimental techniques described thus far have met with somewhat limited success in modeling the acid generation during exposure for some chemical amplification resists such as Shipley SNR 248 resist. In modeling the exposure, two components must be considered: the absorption coefficient and the local concentration of acid. Measuring of the resist transmission and fitting Dill's model to the results will, by definition, include an

†. This wavelength range corresponds to a range of 4000 $cm^{-1}$ to 400 $cm^{-1}$ in wavenumbers.

accurate description of the absorption coefficient. In fact, for all of the chemical amplification resists studied thus far, the change in transmission over lithographically useful doses is sufficiently small such that a constant absorption coefficient can be assumed.

The problem with modeling the exposure concerns the accurate simulation of the local acid concentration. For the SNR 248 resist, no legitimate tag for the acid was found in either the transmission or FTIR measurements. Although methods were developed for monitoring acid generation in the t-BOC resist for both acid generators (see Chapter 7 for details), considerable effort was required. Fortunately, the nature of chemical amplification resists in the deep-UV provides for a simplifying assumption that alleviates some of the problems associated with modeling the acid generation. The catalytic reaction during the bake of these resists provides high sensitivity such that typical exposure doses convert only a small fraction of the acid generator to acid. In this case, the local acid concentration is linearly proportional to the energy absorbed at that point. Therefore, by accurately modeling the absorption coefficient of the resist alone, the local acid concentration is known to within a multiplicative constant. Since this error is a constant factor throughout the resist, modeling the exposure in terms of the absorption coefficient alone does not seriously affect the overall accuracy of the final model for chemical amplification resists.

## 5.3 BAKE CHARACTERIZATION AND MODELING

### 5.3.1 FTIR Spectroscopy

FTIR spectroscopy provides a direct measurement technique for monitoring the concentration of a given chemical bond within the resist during the post-exposure bake. The tracking of a single chemical species concentration with FTIR spectroscopy was already demonstrated in determining the rate coefficient of acid generation during the exposure of a t-BOC chemical amplification resist in the previous section. When using FTIR spectroscopy

to monitor the chemical changes occurring during the bake, the important peaks must be identified and associated with the appropriate chemical bond. The size of the peak must then be quantified to determine the chemical concentration.

#### 5.3.1.1 FTIR Measurement Techniques

The techniques required to successfully obtain quantitative information from FTIR spectroscopy depend strongly on the resist material under study. The following section details the variety of these techniques through several relevant examples.

Figure 5.9 shows an FTIR spectrum for the t-BOC chemical amplification resist discussed earlier. This resist provides an ideal spectrum for characterization of the bake. In this resist, photo-generated acid removes a t-BOC protecting group from the resin [5]. The characteristic peak at 1760 $cm^{-1}$ provides a direct measure of this deprotection reaction. This peak, in addition to being significantly larger than any noise present within the measurement, is well isolated from other peaks allowing for the easy extraction of quantitative peak size information.

For other resists, the chemical changes occurring during the bake produce no discernible peaks in the raw FTIR spectrum for quantitative analysis. In cases where subtle changes in the FTIR spectrum are not observable in the raw data, a difference spectrum, in which the measurements before the bake are subtracted from the measurements after the bake, can often provide useful information. In this type of difference spectrum, downward peaks correspond to the disappearance of a bond during the bake while an upward peak corresponds to the creation of a bond.

Figure 5.10 shows difference spectra obtained for the post-exposure bake of Shipley SNR 248 resist in which an acid catalyzed crosslinking reaction occurs. The peaks at 1070 $cm^{-1}$ and 990 $cm^{-1}$ can be attributed to the crosslinking reaction. The need for using a

difference spectrum in this case becomes obvious upon examination of the magnitude of the absorbance changes in Figure 5.10 which are two orders of magnitude smaller than the absorbance values in the raw spectrum of the t-BOC resist in Figure 5.9. In order to obtain quantitative information from such small absorbance changes, the measurement noise must be minimized.

The loss of spinning solvent during the post-exposure bake must be accounted for when using difference spectra to obtain quantitative concentration values. Solvent bake-out may produce significant peaks in an FTIR difference spectrum. The loss of solvent during the bake for SNR 248 resist can be easily observed by taking a difference spectrum for an unexposed region of the resist where no crosslinking occurs. The resulting spectrum, shown in Figure 5.11, contains two peaks at 1240 $cm^{-1}$ and 1090 $cm^{-1}$ which nearly coincide with the characteristic crosslinking peaks of Figure 5.10. To remove this solvent bake-out effect so that the crosslinking can be accurately quantified, the solvent loss spectrum must be subtracted from any measurements taken in the exposed regions of the resist where both crosslinking and solvent bake-out occur. Mathematically, this process is given by:

$$F = [E_A - E_B] - [U_A - U_B] \qquad [5.4]$$

where F is the final difference spectrum, E and U are spectra obtained in the exposed and unexposed regions of the resist, and the subscripts B and A correspond to spectra obtained before and after the bake, respectively. The second term of this equation represents the solvent bake-out spectrum. The subtraction process described by equation [5.4] produced the crosslinking spectra of Figure 5.10.

### 5.3.1.2 Extracting Data from FTIR Spectra

The size of a peak in an FTIR spectrum determines the number of associated chemical bonds within the resist. Measurement of the peak size can thus lead to a quantitative value for the concentration of a given chemical species. Several analytical methods provide quantitative peak size information. In the most rigorous approach, the area of the spectrum beneath the peak is integrated. If the shape of the peak remains constant during the bake, then evaluation of the maximum peak height represents an alternative measure for the peak area.

A user-oriented software tool has been written for extracting quantitative data from FTIR spectra based on these peak measurement techniques. In most cases, evaluation of the peak size requires the calculation of a baseline. This baseline follows the shape the spectrum would follow without the absorbing peak present. The program fits a polynomial baseline to any user-specified region of the curve. Figure 5.12 demonstrates the fitting of an eighth order polynomial baseline to the FTIR spectrum for the t-BOC resist in the region surrounding the characteristic deprotection peak at 1760 $cm^{-1}$. By selecting among a list of available options, the user may request either the integration of the area between the spectrum and the baseline or, more simply, evaluation of the maximum displacement between the two curves.

For difference spectra such as that shown for SNR 248 in Figure 5.10, calculation of a consistent baseline becomes difficult when absorbance changes are on the same order as the noise. However, in the difference spectra of SNR 248, the characteristic crosslinking peaks at 990 $cm^{-1}$ and 1070 $cm^{-1}$ increase in size at a proportional rate. In cases such as this, the program is capable of quantifying the post-exposure bake reaction by calculating the maximum peak-to-peak difference between the two peaks such that no baseline fitting is required.

The large number of techniques available in this program for determining chemical species concentrations from FTIR spectra combine to provide a powerful tool for streamlining the data extraction process. Once the method for extracting the relevant data for a given resist has been established, the program can produce an entire set of data from FTIR measurements taken at a single bake temperature. Figure 5.13 shows a complete data set obtained at various exposure doses and bake times for the t-BOC resist using the baseline fitting approach described earlier. Each data point in this set corresponds to the measurement of one FTIR spectrum.

### 5.3.2 Interferometric Measurements

While FTIR spectroscopy provides a direct measurement of the chemical changes occurring within the resist, obtaining a full set of data necessary for complete characterization can be a long and tedious process. For some resists, however, FTIR measurements are ideally suited for correlation with other indirect, but in-situ, measurement techniques to produce rapid data collection in real time.

For the t-BOC chemical amplification resists, Spence *et al.* have shown that the resist shrinks during the post-exposure bake, and that the extent of the thickness loss is linearly proportional to the amount of deprotection as shown in Figure 5.14 [9]. By monitoring the thickness change during the bake, the extent of deprotection in this resist can be indirectly measured.

Interferometry is a commonly used technique for the in-situ measurement of thickness change in thin films. The Perkin-Elmer Development Rate Monitor (DRM)† is a commercially available interferometric tool for monitoring resist dissolution [10]. The DRM was modified to measure thickness loss of the t-BOC resist during the bake by replacing the

†. See section 5.4 for a more detailed description of the DRM.

development tank with a hot plate [9]. When the exposed wafer is placed in contact with the hot plate through a vacuum chuck, the interferometric measurement system is activated. The DRM can monitor several exposure zones simultaneously leading to rapid data acquisition. A plot of deprotection (thickness loss) as a function of bake time for several exposure doses on a single wafer is shown in Figure 5.15. The rate of data acquisition (200 seconds + set-up time) compares favorably with the time required to obtain the set of data using FTIR spectroscopy in Figure 5.13 which took approximately two hours to complete.

### 5.3.3 Kinetic Modeling of Bake Data

The derivation of a model describing the post-exposure bake of a resist requires the conversion of the species concentration information to a kinetic description of the resist behavior. Obviously, this conversion depends upon the type of resist and the kind of reactions occurring within the resist during the bake. However, some issues involved in determining the kinetic bake model are applicable to most resist systems and thus merit further discussion.

The characterization methods described thus far can be classified as bulk measurement techniques. In other words, the species concentrations obtained when using these methods actually correspond to an average value over the entire resist thickness. Any attempt to model the data must take this bulk averaging into account. By using the ***SAMPLE-ARK*** program described in Chapter 3, different kinetic models can be compared with experimental data by solving the kinetic equations at each point in the resist and then averaging the results over the resist thickness. Ideally, an automated fitting routine could determine the optimum kinetic model and evaluate the reaction rate coefficients. However, at present, a trial-and-error method is still required to produce a kinetic model in most cases.

Sometimes the differential equations which describe the resist kinetics have an analytic solution. This, in fact, occurs for both of the acid catalyzed resist systems discussed in Chapters 6 and 7. For these chemical amplification resists, a least squares fitting routine has been developed for modeling the resist kinetics. This program, which is similar to the ABC fitting program described earlier, calculates the reaction rate coefficients that provide the best fit to the experimental data. Figure 5.16 shows the resulting fit to the modified DRM data for the t-BOC resist using the simple catalytic model:

$$\text{Deprotection Rate} = k[T]\,[A]^m \qquad [5.5]$$

where [T] is the concentration of t-BOC groups, [A] is the concentration of photo-generated acid, k is the rate coefficient, and m is the acid concentration power term.

### 5.3.4 Measuring the Diffusion Coefficient

At this point, no fast and reliable technique that is consistent with standard resist processing has been found to measure diffusion coefficients accurately. Determination of the diffusion coefficient becomes especially difficult when the diffusion coefficient depends upon chemical species concentrations within the resist. The accurate determination of diffusion coefficients within the resist is an issue that must be addressed in the future in order to obtain a complete understanding of some of the more important resist technologies available today such as chemical amplification and silylation.

## 5.4 DEVELOPMENT CHARACTERIZATION AND MODELING

To model the resist development, the dissolution rate must be related to the chemical species concentrations within the resist following the bake. Dill *et al.* first used this technique in expressing the dissolution rate of diazo-type resists in terms of the normalized PAC concentration [1]. Modeling the development of complex resist materials requires both

an experimental measurement system for monitoring the dissolution rate as well as a powerful software package for fitting various dissolution rate models to the experimental data.

### 5.4.1 Dissolution Rate Measurements with the DRM

Interferometric techniques were first pioneered by Dill *et al.* for monitoring resist dissolution [1]. Since that time, the Perkin-Elmer Development Rate Monitor (DRM) has become the primary instrument for high-speed, dissolution rate data acquisition. The DRM uses optical reflectivity at a nonexposing wavelength to monitor thin film thickness variations. A photodiode array provides the ability to track multiple zones on a single wafer simultaneously. Figure 5.17 shows a typical interferometric signal obtained from the DRM for SNR 248 resist. From this raw data, the resist dissolution rate can be calculated. Figure 5.18 shows the resulting plot of the dissolution rate in SNR 248 resist as a function of depth in the resist for several different exposure doses.

### 5.4.2 Parameter Extraction with *PARMEX*

The dissolution parameter extraction program ***PARMEX*** developed at the University of California at Berkeley provides a powerful tool for correlating the dissolution rate with the chemical state of the resist following the bake [11]. Initial versions of ***PARMEX*** could be used to fit various dissolution rate models describing the development of diazo-type resists in terms of the PAC concentration. In a more recent version of ***PARMEX*** developed by Chiu [12], the dissolution rate can be correlated with chemical species concentrations from kinetic bake models as calculated by ***SAMPLE-ARK***. For example, Figure 5.19 plots the dissolution rate of SNR 248 resist versus the concentration of two different species following the post-exposure bake. In Figure 5.19a, two distinct curves result when plotting the dissolution rate as a function of photo-generated acid concentration at two different bake temperatures. This

result indicates that the acid concentration does not uniquely determine the dissolution rate. However, when the dissolution rate is plotted as a function of activated crosslinking site concentration, a good measure of the crosslinking reaction (see Chapter 6), a single-valued function is obtained as seen in Figure 5.19b.

## 5.5 SUMMARY

A set of resist characterization techniques has been explored for monitoring the chemical and physical changes that occur within resist materials during processing. Emphasis has been placed on achieving rapid data acquisition rates in a manner consistent with standard resist processing. The methods discussed in this chapter include optical transmission, FTIR spectroscopy, and interferometric measurements. FTIR spectroscopy provides a powerful tool for directly monitoring specific chemical bonds within the resist during the exposure and bake. However, FTIR spectroscopy does not provide real-time data acquisition. Alternative in-situ techniques such as optical transmission during the exposure and interferometry during the bake (for t-BOC resists) indirectly monitor the chemical changes in real time but must be correlated with more direct measurements such as FTIR spectroscopy.

Newly developed simulation tools provide a useful aid in generating mechanistic models from experimental data. One program designed for quantitative FTIR analysis provides a variety of techniques for calculating chemical species concentrations within the resist from FTIR spectra. These techniques include baseline fitting and peak size evaluation through integrated area, maximum height, or peak-to-peak calculations. Other programs based on least squares algorithms accurately determine fitting parameters from experimental data. One such program performs a rigorous simulation of the resist/quartz stack in modeling optical transmission data in terms of one or more photolytic reactions using Dill's ABC parameters. Another program designed for chemical amplification resists can evaluate rate

coefficients for acid catalyzed bake reactions given a complete set of chemical species concentrations.

## REFERENCES


[1] F. Dill, W. Hornberger, P. Hauge, and J. Shaw, "Characterization of Positive Photoresist," *IEEE Transactions on Electron Devices*, vol. ED-22, no. 7, pp. 445-452, July 1975.

[2] Y. Shacham-Diamand, "Modeling of Novolak-Based Positive Photoresist Exposed to KrF Excimer Laser UV Radiation at 248 nm," *IEEE Trans. Semicond. Manufact.*, vol. 3, no. 1, pp. 37-44, May 1990.

[3] D. Drako, W. Partlo, W. Oldham, and A. Neureuther, "A Characterization System for Deep Ultra-Violet (UV) Resists," *Proceedings SPIE: Advances in Resist Technology and Processing VI*, vol. 1086, 1989.

[4] J. Thackeray, G. Orsula, E. Pavelchek, D. Canistro, L. Bogan, A. Berry, and K. Graziano, "Deep UV ANR Photoresists for 248 nm Excimer Laser Photolithography," *Proceedings SPIE: Advances in Resist Technology and Processing VI*, vol. 1086, pp. 34-47, 1989.

[5] R. Tarascon, E. Reichmanis, F. Houlihan, A. Shugard, and L. Thompson, "Poly(t-BOC-styrene sulfone)-Based Chemically Amplified Resists for Deep-UV Lithography," *Polymer Engineering and Science*, vol. 29, no. 13, pp. 850-855, Mid July, 1989.

[6] W. Press, B. Flannery, S. Teukolsky, and W. Vetterling, "Numerical Recipes - The Art of Scientific Computing," Cambridge University Press, pp. 521-528, 1986.

[7] W. Oldham, S. Nandgaonkar, A. Neureuther, and M. O'Toole, "A General Simulator for VLSI Lithography and Etching Processes: Part I - Application to Projection Lithography," *IEEE Transactions on Electron Devices*, vol. ED-26, no. 4, pp. 717-722, April 1979.

[8] D. Marquardt, "An Algorithm for Least-Squares Estimation of Nonlinear Parameters," *J. Soc. Indust. Appl. Math*, vol. 11, no. 2, pp. 431-441, June 1963.

[9] C. Spence and R. Ferguson, "Some Experimental Techniques for Characterizing Photoresists," *Proceedings SPIE: Advances in Resist Technology and Processing VIII*, vol. 1466, 1991.

[10] A. McCullough and S. Grindle, "Resist Characterization Using a Multichannel Development Rate Monitor," *Proceedings Sixth International Technical Conference on Photopolymers*, Ellenville, New York, 1982.

[11] W. Bell II, P. Flanner III, C. Zee, N. Tam, and A. Neureuther, "Determination of Quantitative Resist Models from Experiment," *Proceedings SPIE: Advances in Resist Technology and Processing V*, vol. 920, pp. 382-389, 1988.

[12] A. Chiu, "PIX (Program User Interface in X)", *Master's Thesis*, U. of California, Berkeley, 1991.

**Figure 5.1:** A diagram of the experimental system used for resist characterization [3].

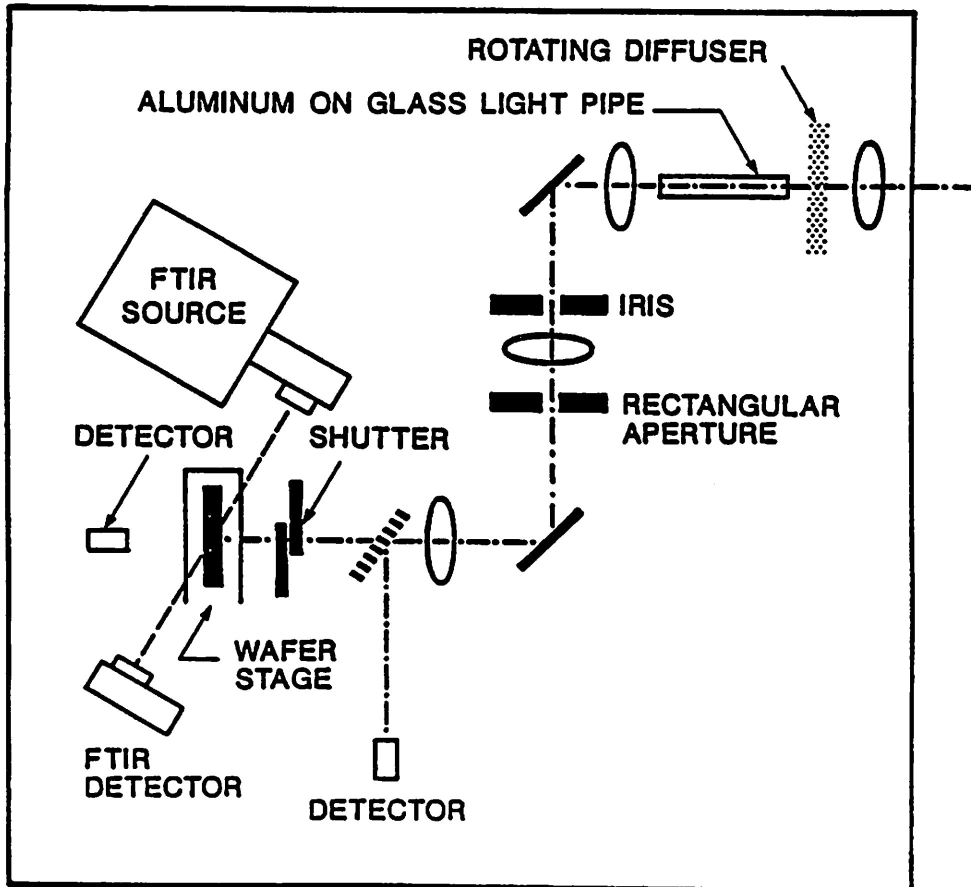

**Figure 5.2:** Schematic of the resist/quartz substrate stack for optical transmission measurements showing the reflections occurring at various boundaries for a) an idealistic configuration and b) the configuration used currently.

a)

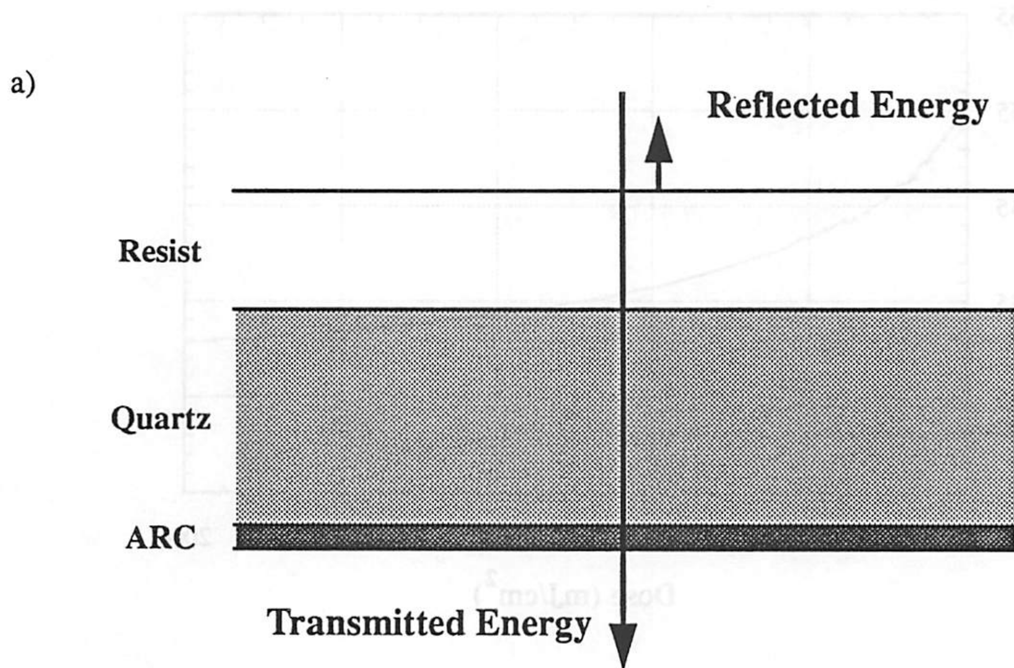


b)

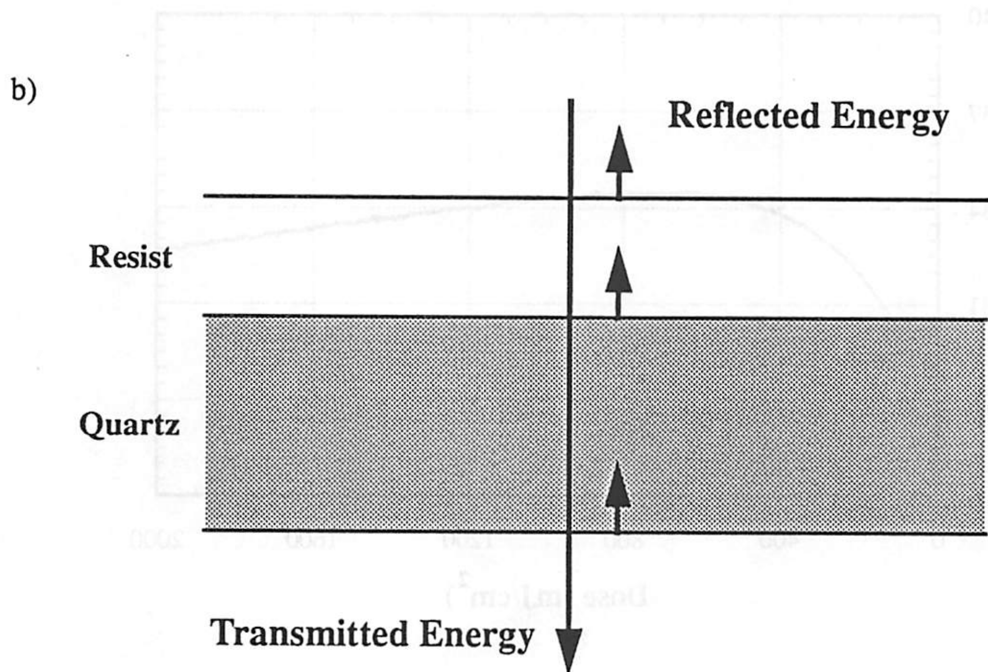

**Figure 5.3:** Transmission versus exposure dose for Shipley SNR 248 resist.

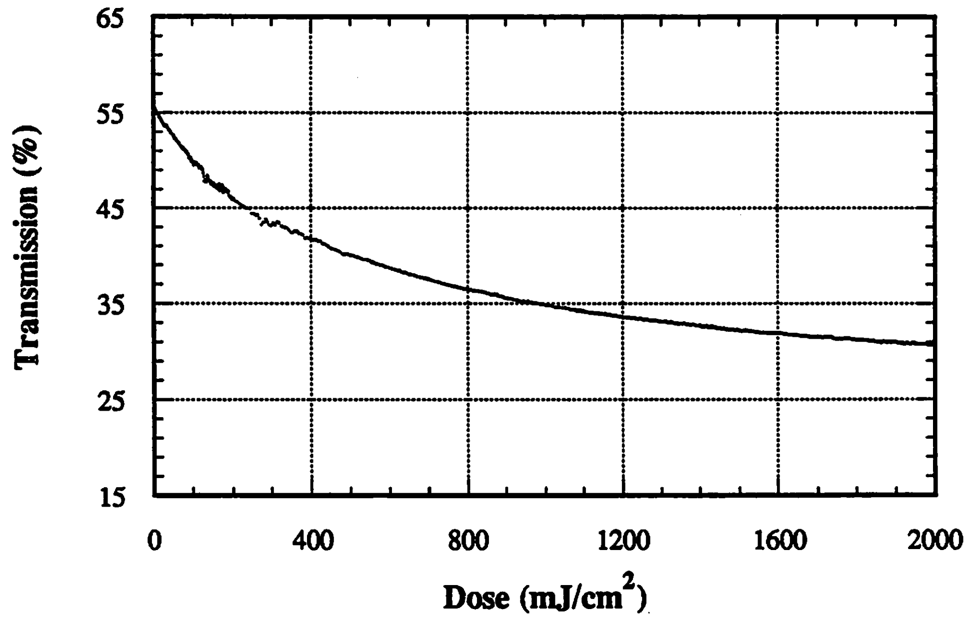


**Figure 5.4:** Transmission versus exposure dose for a t-BOC chemical amplification resist.

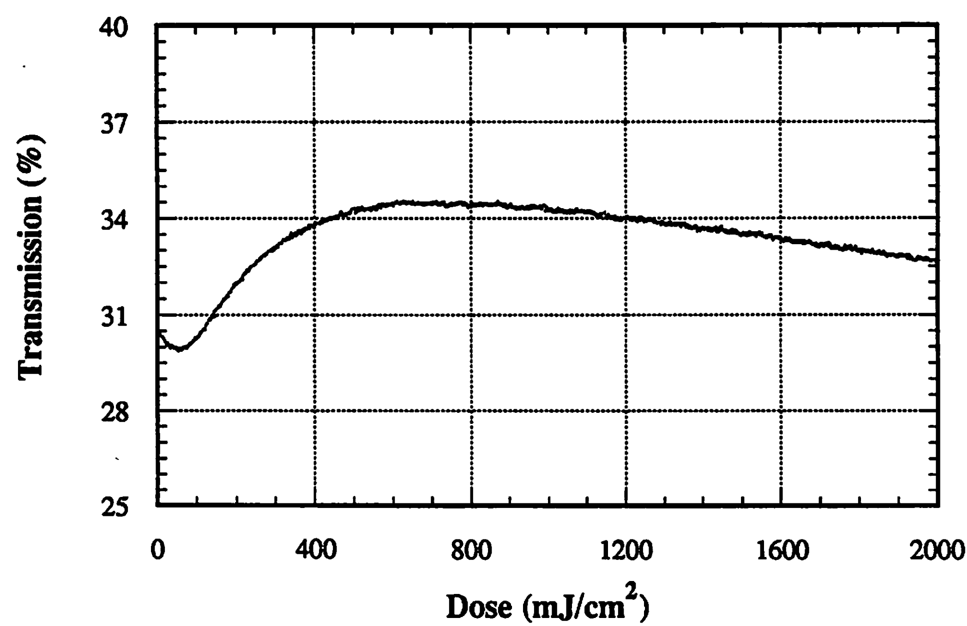

**Figure 5.5:** Comparison of Dill's ABC model calculated using the ABC fitting program with experimental transmission data for SNR 248 resist.

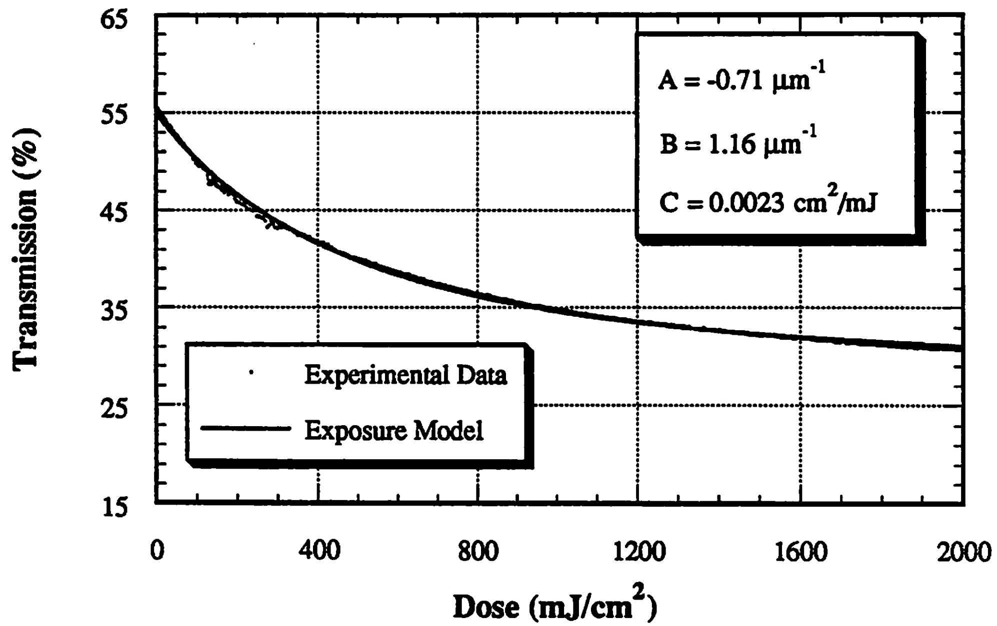


**Figure 5.6:** Comparison of Dill's ABC model calculated using the ABC fitting program and two sets of ABC parameters with experimental transmission data for a t-BOC resist.

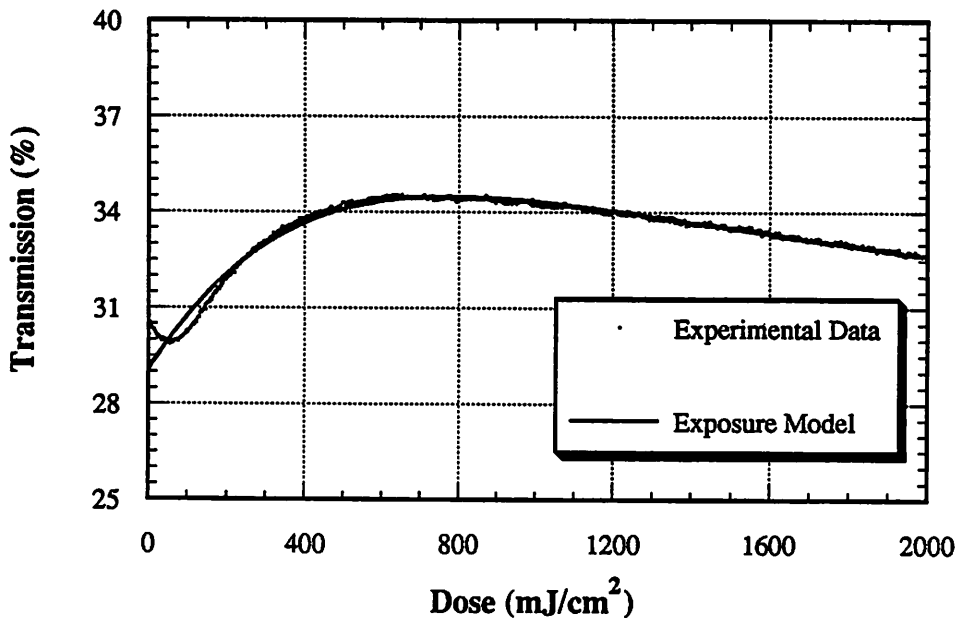

**Figure 5.7:** FTIR difference spectrum of exposed t-BOC resist with the peak at 1540 $cm^{-1}$ indicative of acid generation.

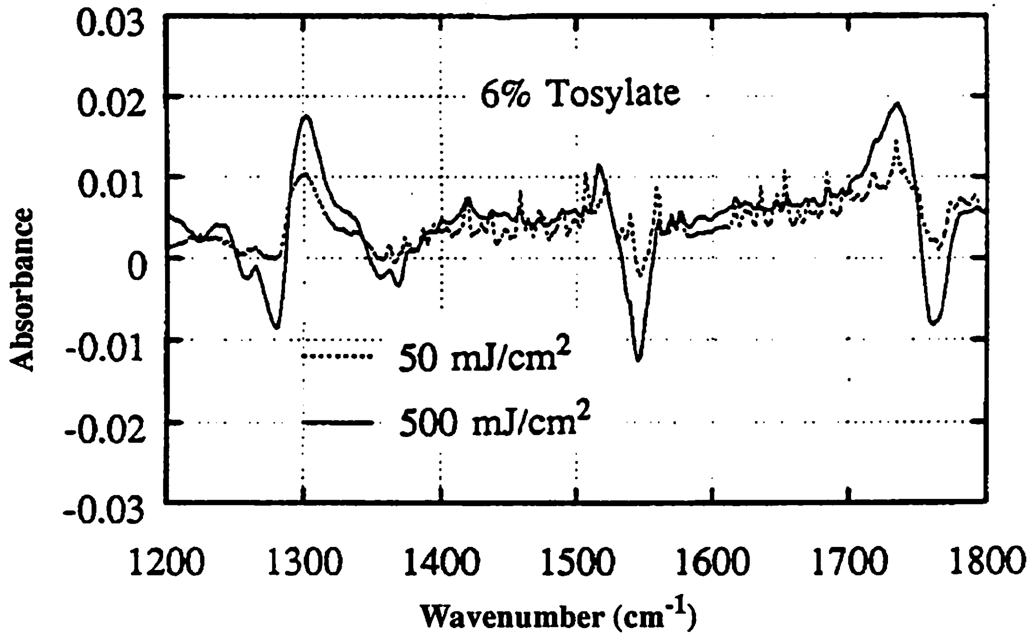


**Figure 5.8:** Plot of acid concentration as measured by FTIR spectroscopy versus exposure dose. Simulated curve corresponds to a rate coefficient of $C = 0.0045$ $cm^2/mJ$.

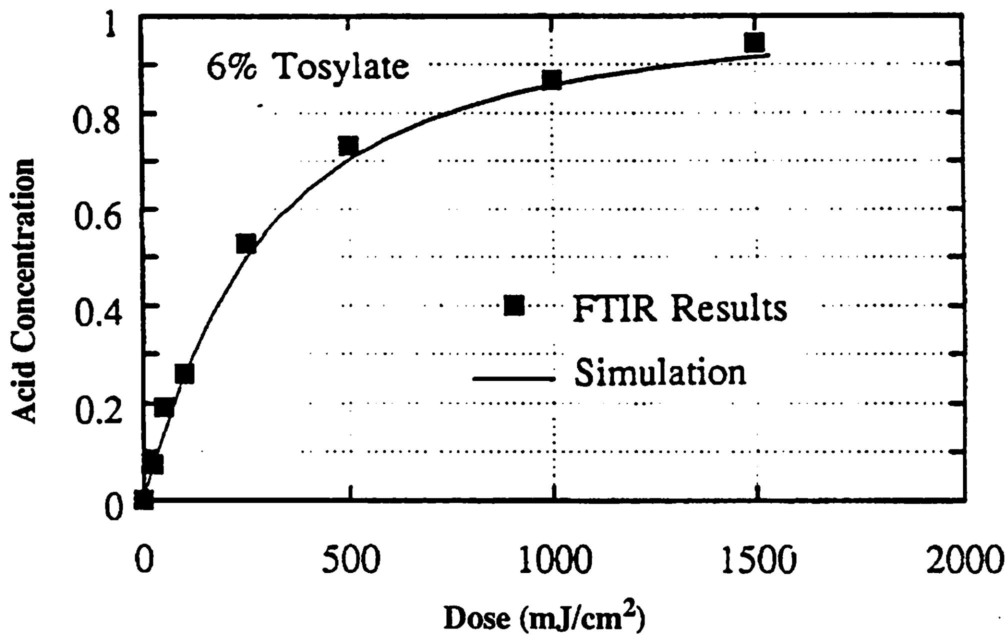

**Figure 5.9:** FTIR spectra of a t-BOC resist. The peak at 1760 $cm^{-1}$ provides a measure of the deprotection reaction.

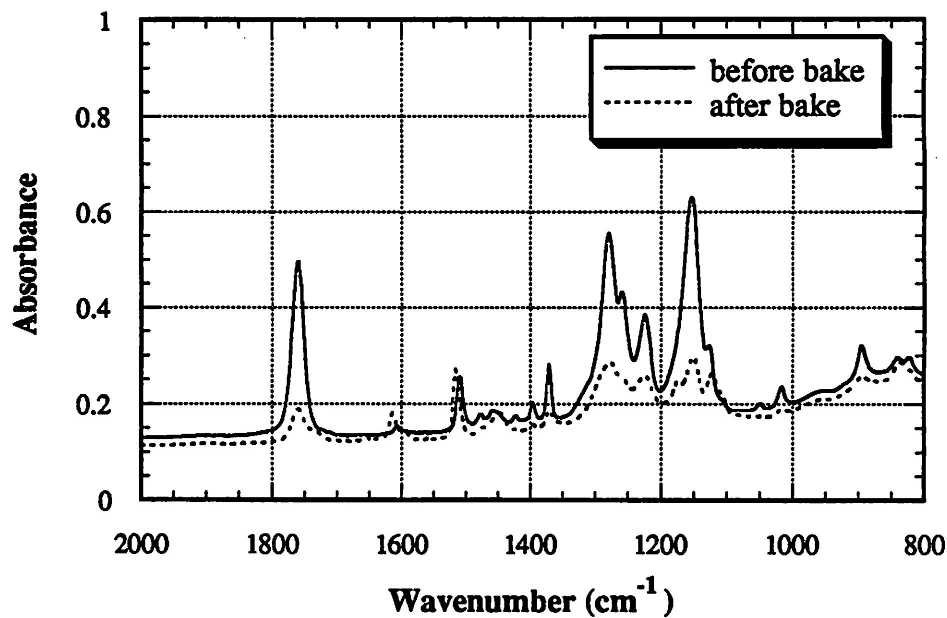


**Figure 5.10:** FTIR difference spectra for SNR 248 resist. Peaks at 990 $cm^{-1}$ and 1070 $cm^{-1}$ provide a measure of the crosslinking reaction.

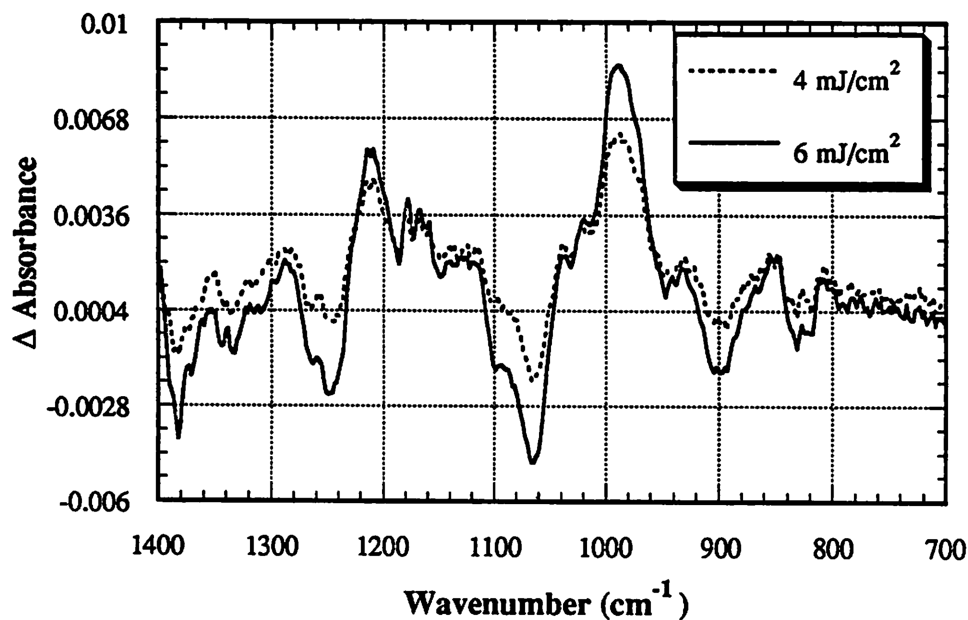

**Figure 5.11:** FTIR difference spectrum of solvent bake-out in SNR 248 resist.

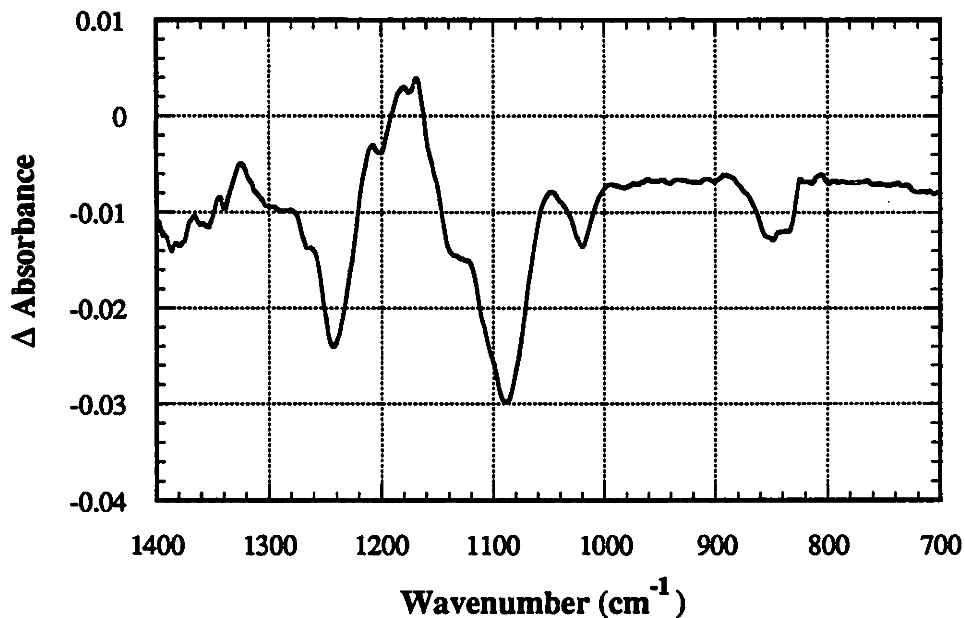


**Figure 5.12:** FTIR spectrum of a t-BOC resist including an eighth-order polynomial baseline fit in the region of the characteristic deprotection peak at 1760 $cm^{-1}$.

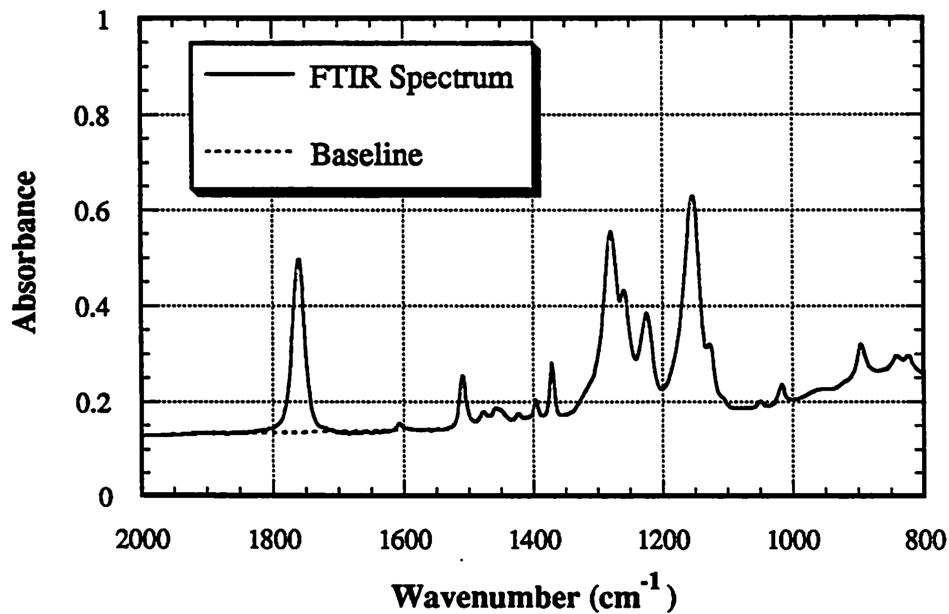

**Figure 5.13:** Complete set of deprotection data for a t-BOC resist for a single bake temperature calculated using the FTIR data extraction software.

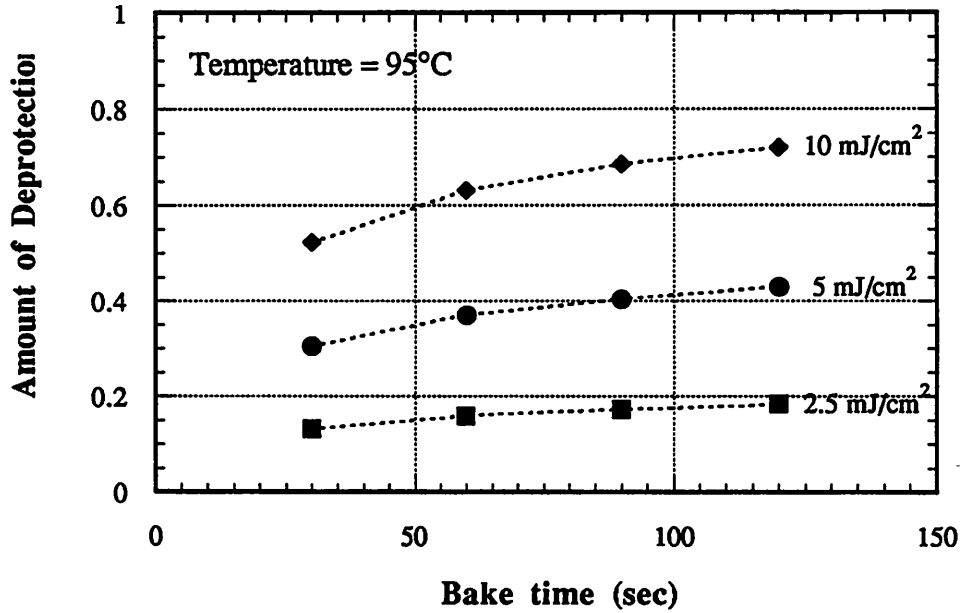


**Figure 5.14:** Plot of thickness change versus the extent of deprotection during the post-exposure bake of a t-BOC resist. The curve follows a linear relationship.

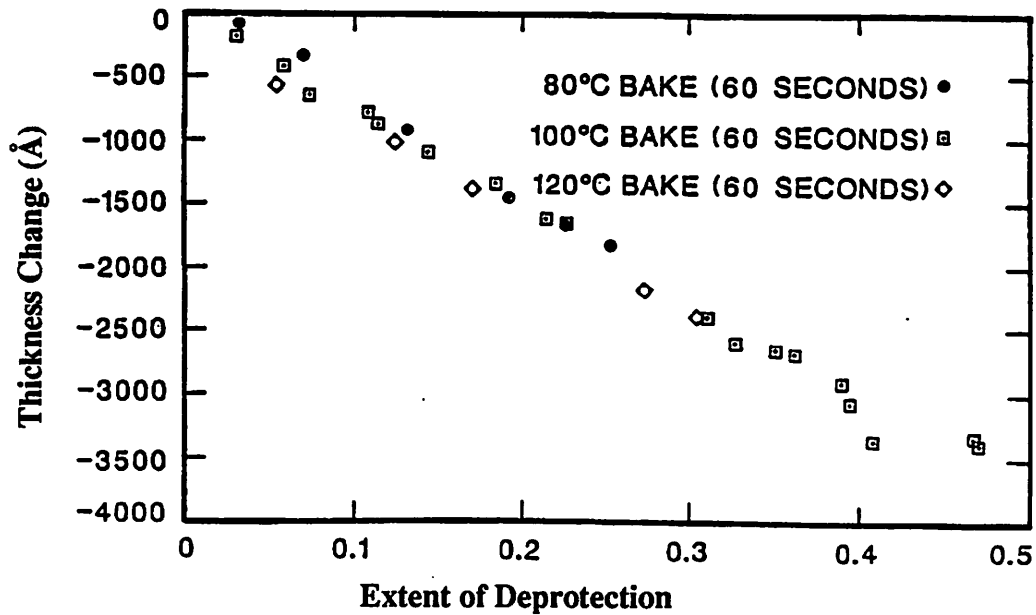

**Figure 5.15:** Extent of deprotection versus bake time for a t-BOC resist as measured by the modified DRM.

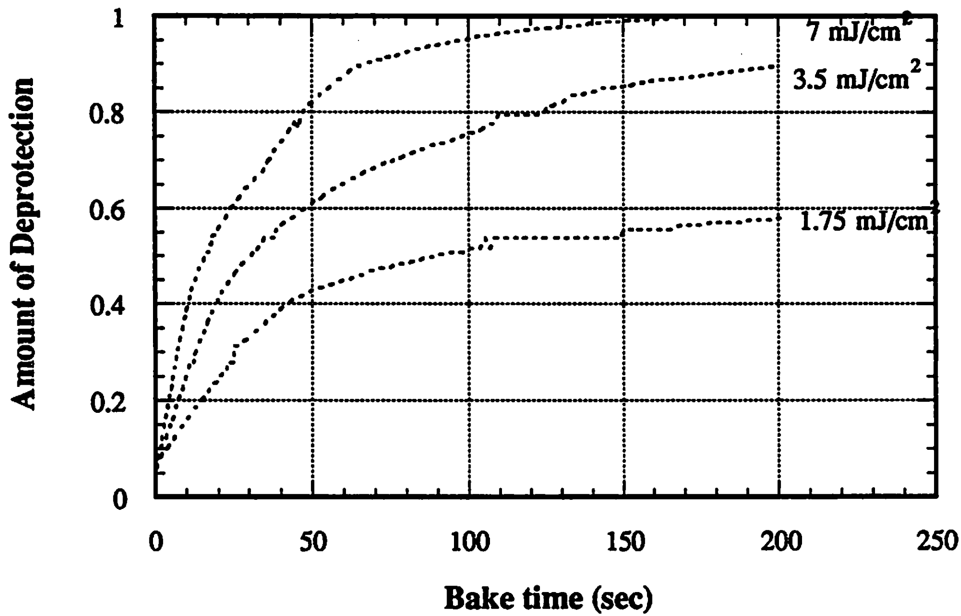


**Figure 5.16:** Kinetic model for the t-BOC deprotection data measured on the modified DRM. The model was calculated using the automated fitting software.

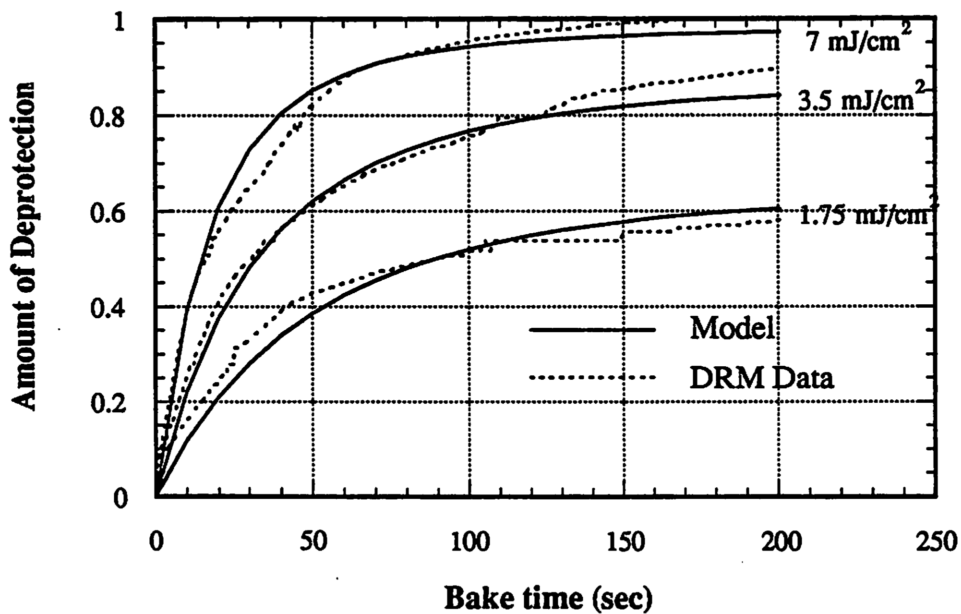

**Figure 5.17:** Raw interferometric signal from the DRM for the development of SNR 248 resist.

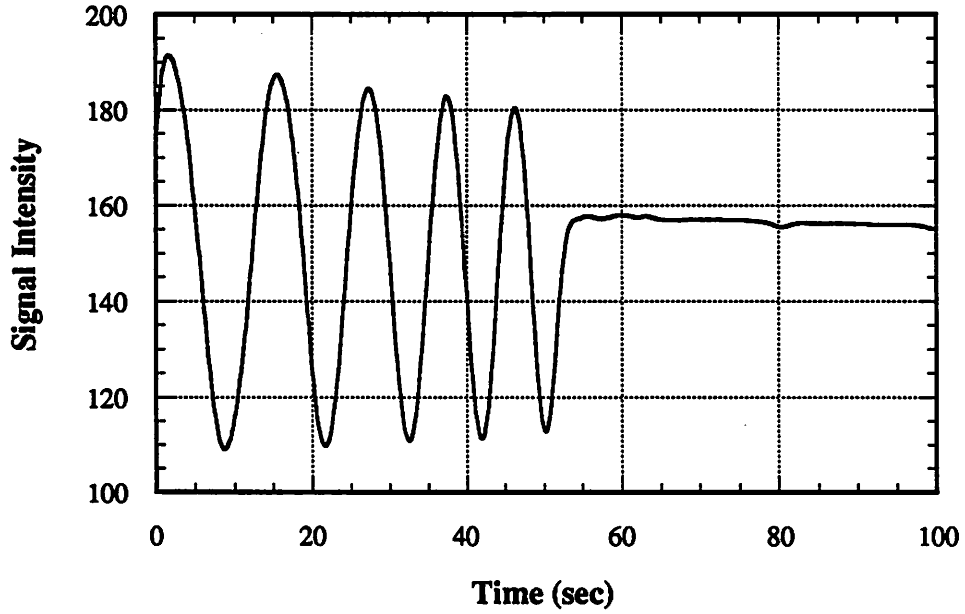


**Figure 5.18:** Dissolution rate of SNR 248 resist versus thickness for several exposure zones as measured on the DRM.

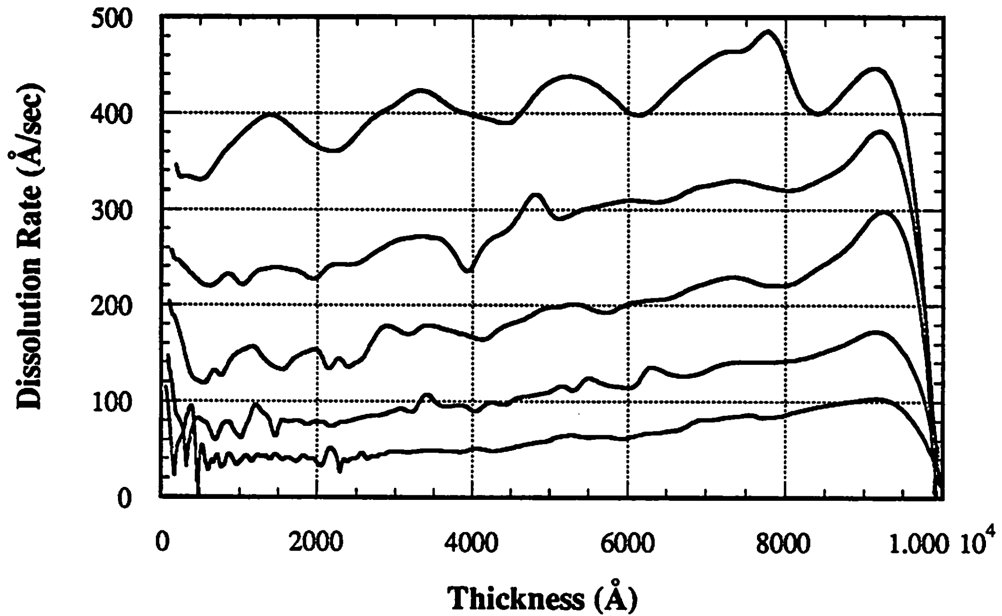

**Figure 5.19:** Correlation of the dissolution rate of SNR 248 resist with a) acid concentration and b) concentration of activated crosslinking sites (extent of crosslinking) as calculated by ***PARMEX.***

a)

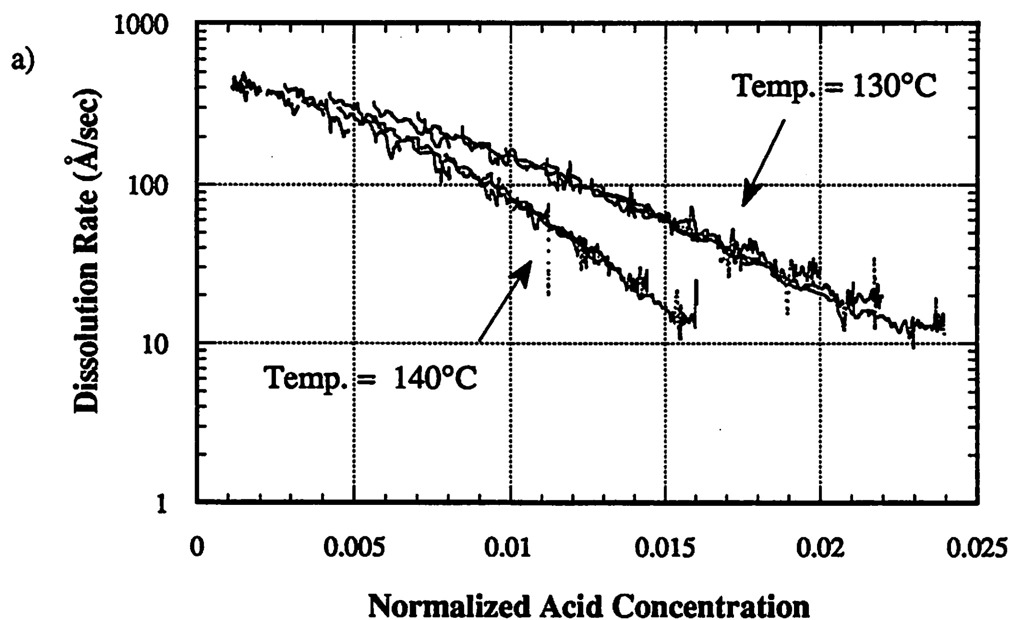


b)

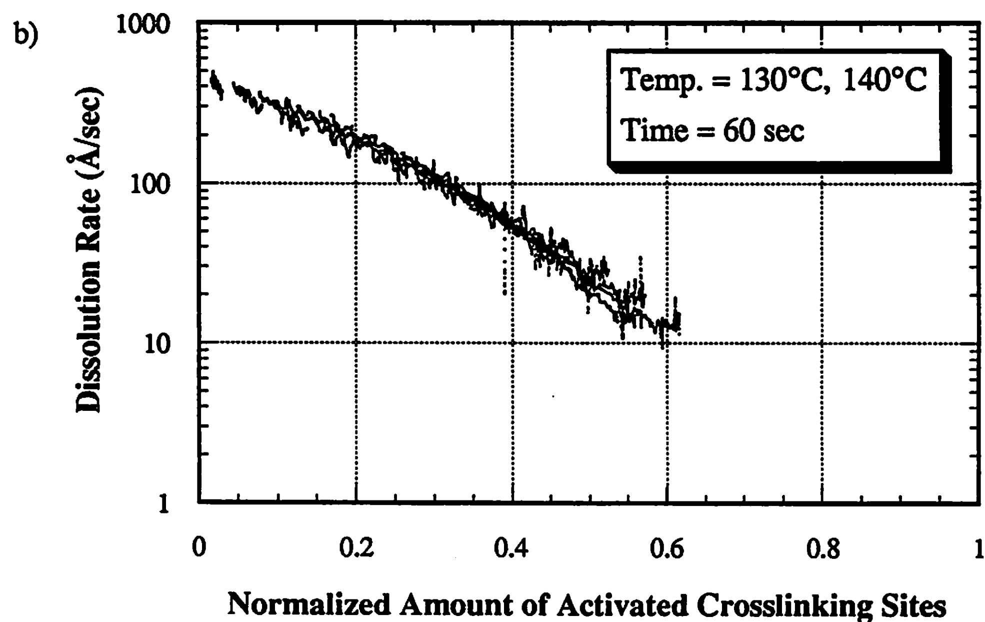

# CHAPTER 6

# MODELING OF AN ACID HARDENING RESIST

A modeling methodology for a class of resist materials that rely on the acid catalyzed crosslinking of the resin matrix during a post-exposure bake is presented. This methodology is used to derive a complete and quantitative model for a production worthy state-of-the-art deep-UV resist, Shipley SNR 248 [1]. The model is based on the chemical and physical mechanisms which determine the resist behavior during the exposure, post-exposure bake, and development processes.

Results of the modeling study suggest that both the nature of the acid catalyzed crosslinking reaction as well as the crosslinking agent structure strongly influence the resist behavior. The crosslinking reaction during the bake is monitored through the characteristic IR absorption bands at 990 $cm^{-1}$ and 1070 $cm^{-1}$. In deriving a kinetic model for the acid catalyzed crosslinking during the bake, an additional acid loss reaction is necessary to successfully explain the dose-dependent saturation of the crosslinking data. A dissolution rate model based upon the crosslinking agent structure and crosslinking-induced molecular weight changes is found to fit the experimentally measured dissolution data quite well. Simulation results using ***SAMPLE-ARK*** are compared with experiments. Good correlation is obtained between simulated development profiles and experimental results over a range of post-exposure bake conditions and mask patterns.

## 6.1 INTRODUCTION

As photolithography moves towards deep-UV exposure wavelengths, new resist materials are required to overcome the low sensitivity and high absorption of standard g-line resist technologies. Resists with chemical amplification have shown both high sensitivity and con-

trast in the deep-UV [1][2][3]. In these resists, photo-exposure first generates an acid within the resist. During the subsequent post-exposure bake, the resist undergoes an acid catalyzed reaction which determines the resist solubility during development. Although much work has been done to improve the performance of these resists, many of the mechanisms that determine the resist performance are still not well understood. Detailed studies of the resists based upon the chemical reaction kinetics and physical mechanisms of the exposure, bake and development steps can lead to both an improved understanding of these mechanisms and to resist models which can accurately simulate the resist behavior under a variety of processing conditions.

In one class of chemical amplification resists, acid catalyzed crosslinking during the post-exposure bake leads to a negative tone resist image [1]. Mechanistic approaches to the modeling of this resist have demonstrated promise in understanding resist behavior. Seligson *et al.* combined the exposure dose, bake temperature, and bake time into an effective dose parameter required to generate resist patterns [4]. This work was extended to a more recent version of this resist, Shipley SNR 248, in the work of Das *et al.* [5]. Fukuda and Okazaki used resist dissolution measurements to model the kinetics of the crosslinking reaction [6]. Recently, Ziger *et al.* proposed a general model for chemical amplification resists and then extracted modeling parameters from characteristic curves of thickness remaining versus exposure dose for the SNR 248 resist [7].

While all of these models use mechanistic approaches which account for the changes that occur within the resist during processing, none of them provide a direct measure of these changes during the individual processing steps. Unfortunately, this type of insight is invaluable in attaining a complete understanding of the resist behavior. The general modeling methodology proposed in Chapter 2 provides such a means for directly measuring these changes during the exposure, post-exposure bake, and development of the resist. In this

chapter, the application of this methodology to Shipley SNR 248 resist results in the development of a mechanistic based working model for the simulation of resist development profiles over a range of post-exposure bake conditions for this state-of-the-art deep-UV resist material.

## 6.2 RESIST CHEMISTRY, PREPARATION, AND PROCESSING

Shipley SNR 248 resist consists of a poly(p-vinyl phenol) resin†, a melamine crosslinking agent, and a photo-acid generator [1]. The structure of the poly (p-vinyl phenol) resin is shown in Figure 6.1a. Figure 6.1b shows the chemical structure of the melamine crosslinking agent. Upon exposure, the acid generator produces hydrobromic acid. During the subsequent post-exposure bake, the photo-generated acid catalyzes a crosslinking reaction between the melamine crosslinking agent and the resin. The extent of this crosslinking determines the dissolution rate in aqueous alkaline developer during the development. The resist becomes insoluble in the regions where the crosslinking has occurred resulting in a negative tone image of the mask pattern.

The resist samples for the modeling experiments were prepared by first spin coating the resist on a substrate at a speed of 4000 rpm for 30 seconds. The resist was spun onto quartz substrates for the transmission experiments, double-polished silicon wafers for the FTIR measurements, and standard silicon wafers for the dissolution rate measurements on the DRM. A pre-exposure bake of 100°C for 1 minute followed the spin to remove excess solvent. A KrF excimer laser was used to perform the exposures of the resist at the deep-UV wavelength of 248 nm. Following the exposure, the resist was baked on a hot plate at temperatures ranging from 130°C to 150°C to drive the crosslinking reaction. The resist was developed in 0.135N MF312 developer at 21°C.

---

†. This resin is also known as poly(p-hydroxystyrene).

## 6.3 MODELING THE EXPOSURE

The exposure of diazo-type resists has typically been modeled by fitting Dill's ABC parameters to measurements of resist transmission as a function of exposure dose as discussed in Chapter 2 [8]. An accurate exposure model for SNR 248 resist should account for both the absorption coefficient of the resist as well as the local acid concentration. Resist transmission measurements for SNR 248 were made in order to model the absorption coefficient using the techniques described earlier in Chapter 5. ABC parameters corresponding to a single photolytic reaction were determined by fitting the experimental transmission data with modified ***SAMPLE*** simulations of the resist/quartz substrate stack transmission using a refractive index of 1.79 for the resist (see Chapter 5). Figure 6.2 compares the experimental measurements with simulation using the fitted parameters of $A = -0.71\ \mu m^{-1}$, $B = 1.16\ \mu m^{-1}$, and $C = 0.0023\ cm^2/mJ$. With these parameters, the Dill model fits the experimental data quite well. The negative value obtained for the A parameter accounts for the resist darkening observed experimentally.

The reaction rate coefficient for the acid generation reaction is needed to determine the local acid concentration as a function of the exposure dose. In measuring the resist transmission, it was hoped that the C value obtained in fitting the Dill model to the experimental data would correspond to this rate coefficient. However, other reactions may occur simultaneously that affect the resist transmission as well. For this reason, FTIR spectroscopy was used in conjunction with the optical transmission measurements to monitor the exposure related chemical changes. While no changes occurred in the IR spectrum that could be attributed to acid generation, the peak at 1560 $cm^{-1}$, characteristic of the melamine crosslinking agent, decreased at a similar rate to the resist transmission as shown in Figure 6.3. As a result, an alternate reaction in the melamine unrelated to the crosslinking, rather than acid generation, may account for the observed darkening.

Further evidence derived from measurements on a version of SNR 248 resist with three times the amount of acid generator supports this conclusion. Figure 6.4 plots the transmission versus dose for both the standard version of SNR 248 and the 3X version. As expected, the overall transmission decreases with higher loadings of the acid generator. In each resist mixture, if the darkening in the resist transmission results from acid generation, then the experimentally determined A parameter should be proportional to the concentration of acid generator within the resist [8]. A simplified expression for the A parameter can easily be derived [8] such that:

$$A = \frac{\ln\left[\frac{T(\infty)}{T(0)}\right]}{d} \qquad [6.1]$$

where d is the resist thickness and T(t) is the resist transmission at time t. Using this expression, it can easily be shown that the value of the fitted A parameter remains essentially independent of acid generator concentration. This result indicates that the acid generation reaction probably does not cause the experimental resist transmission darkening as suspected.

These results seem to establish a significant roadblock in modeling the complete resist process. Fortunately however, because of the nature of chemical amplification resists in the deep-UV, use of this ABC model in calculating the local acid concentration adds very little inaccuracy to the overall resist model. The lithographically useful dose for this resist (< 50 mJ/cm$^2$) is much smaller than the dose required to convert typical acid generators completely to acid (> 1000 mJ/cm$^2$) [9]. Therefore, it is expected that the resist is operating in a region where the local concentration of generated acid is approximately proportional to the exposure dose at that point, just as predicted with the fitted ABC model. Consequently, the simulated concentration of acid should be, at worst, in error by a multiplicative factor

only which will not significantly affect the overall accuracy of the model. However, to gain a better understanding of the resist exposure, further work is still required to determine the acid generation rate coefficient more accurately.

The importance of the optical properties of the resin in determining the resist performance can be easily understood from resist transmission measurements. Figure 6.5 shows the transmission versus exposure dose for an earlier version of the resist, XP-8798, that used a novolak resin. Novolak resins absorb much more strongly than poly (p-vinyl phenol) in the deep-UV as demonstrated by the lower transmission values in Figure 6.5. This absorption in the resin can lead to non-vertical sidewalls that seriously affect the ability of a resist to both resolve small features and to act as an etch mask during the pattern transfer process. Furthermore, in negative resists, the re-entrant profiles that result from high absorption can seriously impede both inspection and metrology.

## 6.4 MODELING THE BAKE

From the exposure model, the local concentration of acid at any point in the resist, within a multiplicative factor, can be determined as function of exposure dose, resist thickness, and substrate reflectivity. Modeling of the post-exposure bake consisted of relating the local extent of crosslinking to the photo-generated acid concentration through chemical reaction kinetics. The ***SAMPLE-ARK*** program described in Chapter 3 was used to simulate the kinetics of the crosslinking reaction at each point in the resist.

The structure of the melamine crosslinking agent is critical to the crosslinking reaction. Part of the melamine molecule from Figure 6.1b is reproduced in Figure 6.6. During the post-exposure bake, the ether groups on the melamine ($CH_2OR$ where R is an alkyl group), termed *crosslinking sites*, will bond to the resin. The sites that attach to a resin chain ($CH_2OAr$ where Ar is the aromatic ring of the resin) have been termed *activated crosslinking*

*sites*. For a single *crosslinking event* to occur, a connection or bridge must form between two different resin chains through the crosslinking agent. As a result, a melamine molecule must have at least two activated sites to participate in the crosslinking of the resin network. This result will have important consequences in the derivation of the dissolution rate model. The extent of crosslinking that occurs during the bake is thus described by the total number of crosslinking events and, consequently, by the number of activated crosslinking sites.

A reaction mechanism proposed by Blank for the activation of the crosslinking sites is shown in Figure 6.7 [10]. The mechanism consists of four chemical reactions. The regeneration of the acid in the final reaction produces the catalytic nature of SNR 248 that is fundamental to the resist behavior. With this acid catalyzed reaction, each acid molecule generated during exposure can activate many crosslinking sites during the bake, and thus the name chemical amplification has been applied.

A simplified kinetic model can be derived from the proposed crosslinking mechanism by assuming that the formation of the carbonium ion in the second reaction is the rate limiting step [10]. In addition, the alcohol produced in the second reaction of the crosslinking mechanism should evaporate from the thin resist film during the bake leading to an irreversible reaction. The resulting model is given by:

$$\frac{\partial C_{as}}{\partial t} = k_1 C_{us} C_a \qquad [6.2]$$

where $C_{as}$ is the normalized concentration of activated crosslinking sites, $C_{us}$ ($C_{us} = 1 - C_{as}$) is the normalized concentration of unactivated crosslinking sites, $C_a$ is the normalized concentration of acid, and $k_1$ is the reaction rate coefficient. Due to the poor quality of the fit with this simple model, two further additions became necessary. The reason for these additions will become apparent shortly. First, an acid loss reaction was included to quench the

crosslinking reaction. Also, the acid concentration term of the crosslinking reaction was raised to the m$^{th}$ power (m > 1). With these additions, the generalized model is then given by:

$$\frac{\partial C_{as}}{\partial t} = k_1 C_{us} C_a^m \qquad [6.3]$$

$$\frac{\partial C_a}{\partial t} = -k_2 C_a \qquad [6.4]$$

where $k_2$ is the rate coefficient for the acid loss reaction. These differential equations can be solved analytically leading to an expression for the concentration of activated crosslinking sites given by:

$$C_{as} = C_{cs}\left(1 - \exp\left[-C_{ao}^{m}\left(\frac{k_1}{mk_2}\right)(1 - e^{-mk_2 t})\right]\right) \qquad [6.5]$$

where $C_{cs}$ is a constant representing the total concentration of crosslinking sites and $C_{ao}$ is the initial concentration of photo-generated acid.

FTIR spectroscopy was used to monitor the extent of crosslinking during the bake and to determine the bake model parameters $k_1$, $k_2$, and m. Chapter 5 describes in more detail the use of FTIR spectroscopy for monitoring chemical changes in resist during baking. To avoid the large standing waves generated during exposure on silicon, a hard baked layer of KTI 820 resist was used as an anti-reflection coating. The effect of resist thickness changes on FTIR measurements from wafer to wafer decreased substantially with this modification. Typical FTIR results are shown in Figure 6.8 for a 2 minute bake at 150°C. Each of the spectra was obtained by subtracting the spectrum before bake from the spectrum after the bake. The effect of solvent loss was also removed. The downward peak at 1070 cm$^{-1}$, corresponding to a reactant in the reaction, was assigned to the unactivated crosslinking sites while the upward

peak near 990 $cm^{-1}$, corresponding to a product, was assigned to the activated crosslinking sites. The peaks at 990 $cm^{-1}$ and 1070 $cm^{-1}$ increased at the same relative rate as predicted from the model. Consequently, to reduce the noise associated with fitting a baseline, peak-to-peak measurements were used to quantify the concentration of activated sites, and thus the extent of crosslinking during the bake. Results were normalized to the largest peak-to-peak absorbance obtained at high exposure doses (> 50 $mJ/cm^2$): 0.022 on bare silicon and 0.026 when using an anti-reflection coating.

A matrix of experiments was performed at various exposure doses and bake times for bake temperatures of 130°C, 140°C, and 150°C to determine the model parameters. A value of $m = 1.42$ gave the best fit over the entire temperature range. Figure 6.9 shows the experimental results and the model for the three bake temperatures. The acid loss reaction of equation [6.4] was included to model the dose-dependent saturation of the curves in Figure 6.9. Without some type of an acid loss mechanism, the crosslinking would follow a simple catalytic behavior in which the activation of crosslinking sites would proceed to completion irrespective of the exposure dose. It is apparent from the results of Figure 6.9, however, that something causes the cessation of the crosslinking reaction before it reaches completion, and thus the need for the acid loss mechanism. While the simple first-order acid loss reaction of equation [6.3] does seem to fit the data quite well, other possible mechanisms such as the reduction of acid diffusivity due to crosslinking or out-diffusion of acid from the resist may also be responsible for this dose-dependent saturation behavior.

The temperature behavior of the two experimentally determined rate coefficients, $k_1$ and $k_2$, follows an Arrhenius behavior as depicted in Figure 6.10. Therefore, these rate coefficients can be expressed as a pre-exponential term and an activation energy:

$$k_i = k_{io} exp\left(-\frac{E_{ai}}{K_B T}\right)$$ [6.6]

where $K_B$ is Boltzmann's constant and T is the bake temperature. The best fit to the data, as shown in Figure 6.10, was obtained with $k_{1o} = 6.56 \times 10^{11}$ $sec^{-1}$, $E_{ai} = 0.88$ eV, $k_{2o} = 4600$ $sec^{-1}$, and $E_{a2} = 0.43$ eV.

## 6.5 MODELING THE DEVELOPMENT

The third step in the modeling process consists of relating the dissolution rate to the extent of crosslinking that occurred during the post-exposure bake. The crosslinking reaction during the bake increases the molecular weight of the resin. The dissolution rate of polymers has previously been related to the average molecular weight of the polymer through a general empirical expression given by [11]:

$$\text{Rate} \propto \frac{1}{M_w^{\alpha}}$$ [6.7]

where $M_w$ is the average molecular weight and $\alpha$ is an empirical constant dependent upon both the polymer itself as well as the solvent. During the crosslinking reaction, the total weight contained in the resin remains constant at $nM_w(\text{initial})$† where n is the initial number of resin chains. Each crosslinking event that occurs effectively removes one resin chain from the total number of chains when the initial number of chains is much larger than the number of crosslinking events.‡ Therefore, the average molecular weight during the crosslinking reaction can be expressed as:

†. This model assumes that the crosslinking agent has little effect on the weight of a given resin chain once it becomes attached to it.

‡. The reduction in the number of resin chains by one through a single crosslinking event assumes that the crosslinking agent does not connect to the same resin chain twice.

$$M_w = \frac{nM_w\,(\text{initial})}{n - CE} \qquad [6.8]$$

Combining equations [6.7] and [6.8] results in an expression for the dissolution rate in terms of the number of crosslinking events which is given by:

$$\text{Rate} = R_o\,(1 - \frac{CE}{C_o})^{\alpha} \qquad [6.9]$$

where CE is the number of crosslinking events and $R_0$, $C_0$, and $\alpha$ are dissolution model fitting parameters.

The model for the bake, however, was defined in terms of the concentration of activated crosslinking sites, not the number of crosslinking events. Therefore, the dissolution model is not quite complete. The number of crosslinking events must be related to the concentration of activated crosslinking sites. In SNR 248 resist, the melamine crosslinking agent contains six crosslinking sites. However, a more general approach can be taken in deriving a model for any number of crosslinking sites, $n_s$, which can then be made more specific for SNR 248 resist which is believed to be represented by $n_s = 6$. The probability of activating k of $n_s$ sites follows a binomial distribution and is given by:

$$P(k) = \binom{n_s}{k} C_{as}^2\,(1 - C_{as})^{n-k} \qquad [6.10]$$

After the activation of the first site on each melamine, activation of each remaining site effectively reduces the number of resin chains by one, and thus leads to one crosslinking event. Therefore, the expected value for the number of crosslinking events is given by:

$$CE = n_m \sum_{k=2}^{n_s} (k-1) P(k) \qquad [6.11]$$

where $n_m$ is the number of melamine molecules. Combining equations [6.9] and[6.10] results in an expression for the crosslinking events in terms of the concentration of activated crosslinking sites. For $n_s = 2$, this expression becomes:

$$CE = n_m C_{as}^2 \qquad [6.12]$$

while for SNR 248 with $n_s = 6$, this expression becomes:

$$CE = n_m [15C_{as}^2 - 20C_{as}^3 + 15C_{as}^4 - 6C_{as}^5 + C_{as}^6] \qquad [6.13]$$

The dissolution rate as a function of depth within the resist and exposure dose was measured using the Perkin-Elmer DRM [12] as described in Chapter 5. The dissolution parameter extraction program ***PARMEX*** [13] correlated the measured dissolution rate with the concentration of activated sites as determined from the bake model. Equation [6.9] in combination with equation [6.13] was then fit to the data to obtain the three fitting parameters. Figure 6.11 compares the resulting model using $R_o$ = 350 Å/sec, $C_o$ = 6.3, and $\alpha$ = 6.5 with experimental data for bake temperatures of both 130°C and 140°C. This dissolution model based on changes in the molecular weight fits the experimental data quite well. In addition, the fact that the measured dissolution rate produces a single valued function with respect to the concentration of activated crosslinking sites for two separate bake temperatures supports the validity of the bake model for different post-exposure bake conditions. As a result, the two FTIR peaks used to monitor the crosslinking reaction do provide a good measure of the resist dissolution characteristics as predicted.

Recently, Thackeray *et al.* have shown that the consumption of the hydroxyl group on the resin during the crosslinking reaction (see Figure 6.7) provides an alternative mechanism for dissolution inhibition [14]. However, the dominant mechanism, at this point, has yet to be determined. While the molecular-weight-based model of equation [6.9] does not include this alternative mechanism, the approach used in modeling the dissolution rate can be readily adapted to include an additional postulated term based on the hydroxyl-consumption mechanism. However, at this point, it is debatable whether such an expression would provide a more in-depth understanding of the mechanisms involved in the resist dissolution. A more complex expression may simply provide a better empirical fit to the experimental data with more available fitting parameters.

### 6.6 COMPARISON OF SIMULATION WITH EXPERIMENTAL RESULTS

The exposure, post-exposure bake, and development models were combined to simulate resist development profiles. Experimental resist images were generated at Intel on a Nikon deep-UV stepper with $\lambda = 248$ nm, NA = 0.42, and $\sigma = 0.5$. The resist was approximately 1 μm thick. Figure 6.12 compares the results obtained with a 0.4 μm equal lines and spaces pattern and a post-exposure bake of 130°C for 60 seconds. To normalize to the exposure conditions in the experiments from Intel without precise knowledge of resist thickness and stepper illumination, the dose was increased by a factor of 1.4 (from 30 to 42 mJ/cm$^2$) such that large areas cleared in about 1/4 of the total development time as was observed experimentally. With this dose adjustment, the simulated profile shape correlates well with the experimental profiles.

In Figure 6.13, results are compared for the same pattern using a post-exposure bake of 140°C for 60 seconds. Without changing the normalization factor for the dose, the simulated and experimental resist lines show a similar degree of undersizing for a 18 mJ/cm$^2$ dose experimentally and a 25.2 mJ/cm$^2$ dose in the simulation. The observed similarity between

results at different bake temperatures is a second verification that the model accurately predicts the resist behavior with respect to the post-exposure bake conditions.

A final comparison was done for the same bake conditions but with a 0.3 μm line and space pattern. This pattern size, corresponding to 0.5λ/NA, has a much lower image contrast than the 0.4 μm pattern. The results are shown in Figure 6.14. Both the simulation and the experiment show a reduction in the steepness of the sidewall. However, the degradation is more pronounced in the experiment. This could result from effects such as poorer image quality than predicted from diffraction-limited optics or image variations throughout the resist layer due to a high NA.

## 6.7 SUMMARY

A complete model based on the chemical and physical changes that occur during the processing of Shipley SNR 248 acid hardening resist has been developed. Optical transmission, IR absorbance, and dissolution rate measurements were used to characterize the individual process steps.

For the exposure, Dill's ABC model was fit to the optical transmission data. However, FTIR measurements combined with optical transmission measurements on a version of the resist with three times the amount of acid generator demonstrated that the resist darkening during exposure dose, and consequently, the ABC model, does not provide a good indicator of acid generation. Fortunately, it is expected that the amount of photo-generated acid is proportional to the local energy absorbed leading to an accurate prediction of the local acid concentration within a multiplicative factor when using this ABC model.

Peak-to-peak measurements of the IR absorption bands near 990 $cm^{-1}$ and 1070 $cm^{-1}$ were used to monitor the extent of crosslinking during the bake. A model consisting of a primary crosslinking reaction with an order of 1.42 in photo-generated acid and an acid loss

reaction demonstrated a good fit to the experimental data over a range of bake temperatures from 130°C to 150°C. The acid loss reaction was required to explain the dose-dependent saturation of the crosslinking measurements.

A dissolution rate expression based upon molecular weight changes in the resin was derived in terms of the number of crosslinking sites on the melamine and the extent of crosslinking during the bake. This model provided a good fit to the experimental data for post-exposure bakes of 130°C and 140°C. By combining the exposure, bake and development models, resist profiles were simulated using ***SAMPLE-ARK***. Good correlation was observed with experimental results obtained from Intel for several post-exposure bake conditions and pattern dimensions down to 0.3 μm.

## REFERENCES

[1] J. Thackeray, G. Orsula, E. Pavelchek, D. Canistro, L. Bogan, A. Berry, and K. Graziano, "Deep UV ANR Photoresists for 248 nm Excimer Laser Photolithography," *Proceedings SPIE: Advances in Resist Technology and Processing VI*, vol. 1086, pp. 34-47, 1989.

[2] C. Willson, H. Ito, J. Frechet, T. Tessier, and F. Houlihan, "Approaches to the Design of Radiation-Sensitive Polymeric Imaging Systems with Improved Sensitivity and Resolution," *J. Electrochem. Soc.*, vol. 133, no. 1, pp. 181-187, January 1986.

[3] R. Tarascon, E. Reichmanis, F. Houlihan, A. Shugard, and L. Thompson, "Poly(t-BOC-styrene sulfone)-Based Chemically Amplified Resists for Deep-UV Lithography," *Polymer Engineering and Science*, vol. 29, no. 13, pp. 850-855, Mid July, 1989.

[4] D. Seligson, S. Das, H. Gaw, and P. Pianetta, "Process Control with Chemical Amplification Resists Using Deep Ultraviolet and X-ray Radiation," *J. Vac. Sci. Technol. B*, vol. 6, no. 6, pp. 2303-2307, Nov/Dec 1988.

[5] S. Das, J. Thackeray, M. Endo, J. Langston, and H. Gaw, "A Systematic Investigation of the Photoresponse and Dissolution Characteristics of an Acid Hardening Resist," *Proceedings SPIE: Advances in Resist Technology and Processing VII*, vol. 1262, pp. 60-71, 1990.

[6] H. Fukuda and S. Okazaki, "Kinetic Model and Simulation for Chemical Amplification Resists," *J. Electrochem. Soc.*, vol. 137, no. 2, pp. 675-679, February 1990.

[7] D. Ziger, C. Mack, and R. Distasio, "The Generalized Characteristic Model for Lithography: Application to Negatively Chemically Amplified Resists," *Proceedings SPIE: Advances in Resist Technology and Processing VIII*, vol. 1466, 1991.

[8] F. Dill, W. Hornberger, P. Hauge, and J. Shaw, "Characterization of Positive Photoresist," *IEEE Trans. Electron Devices*, vol. ED-22, no. 7, pp. 445-452, July 1975.

[9] R. Ferguson, C. Spence, E. Reichmanis, L. Thompson, and A. Neureuther, "Investigation of the Exposure and Bake of a Positive Acting Resist with Chemical Amplification," *Proceedings SPIE: Advances in Resist Technology and Processing VII*, vol. 1262, pp. 412-424, 1990.

[10] W. Blank, "Reaction Mechanism of Melamine Resins," *Journal of Coatings Technology*, vol. 51, no. 656, pp. 61-70, September 1979.

[11] M. Bowden, "A Perspective on Resist Materials for Fine-Line Lithography," in *Materials for Microlithography - ACS Symposium Series 266*, ed. L. Thompson, C. Willson, and J. Frechet, p. 71, American Chemical Society, 1984.

[12] A. McCullough and S. Grindle, "Resist Characterization Using a Multichannel Development Rate Monitor," Perkin-Elmer Corporation, May 1984.

[13] W. Bell II, P. Flanner III, C. Zee, N. Tam, and A. Neureuther, "Determination of Quantitative Resist Models from Experiment," *Proceedings SPIE: Advances in Resist Technology and Processing V*, vol. 920, pp. 382-389, 1988.

[14] J. Thackeray, G. Orsula, M. Rajaratnam, R. Sinta, D. Herr, and E. Pavelchek, "Dissolution Kinetics of ANR Photoresists: Crosslinking vs. -OH Site Consumption," *Proceedings SPIE: Advances in Resist Technology and Processing VIII*, vol. 1466, 1991.

**Figure 6.1:** Chemical structure of a) the poly (p-vinyl phenol) resin and b) the melamine crosslinking agent in SNR 248 resist.

a)

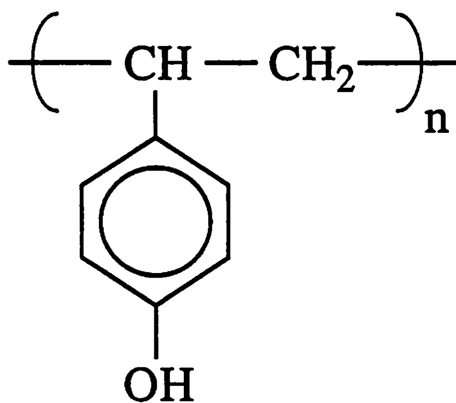


b)

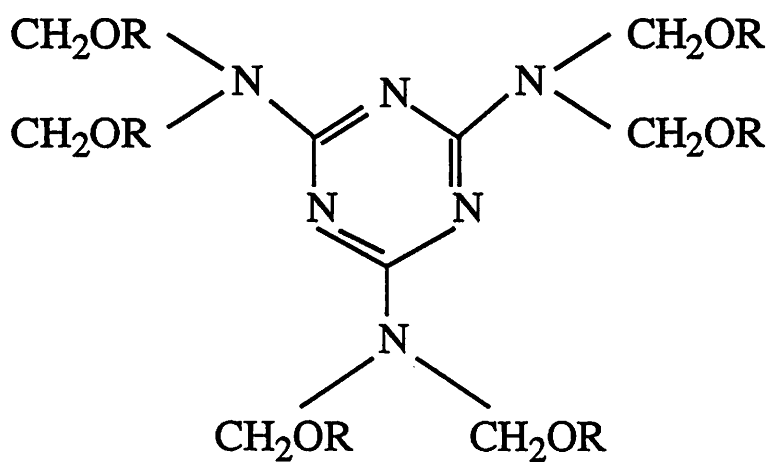

**Figure 6.2:** Experimental and simulated transmission characteristics of SNR 248 resist.

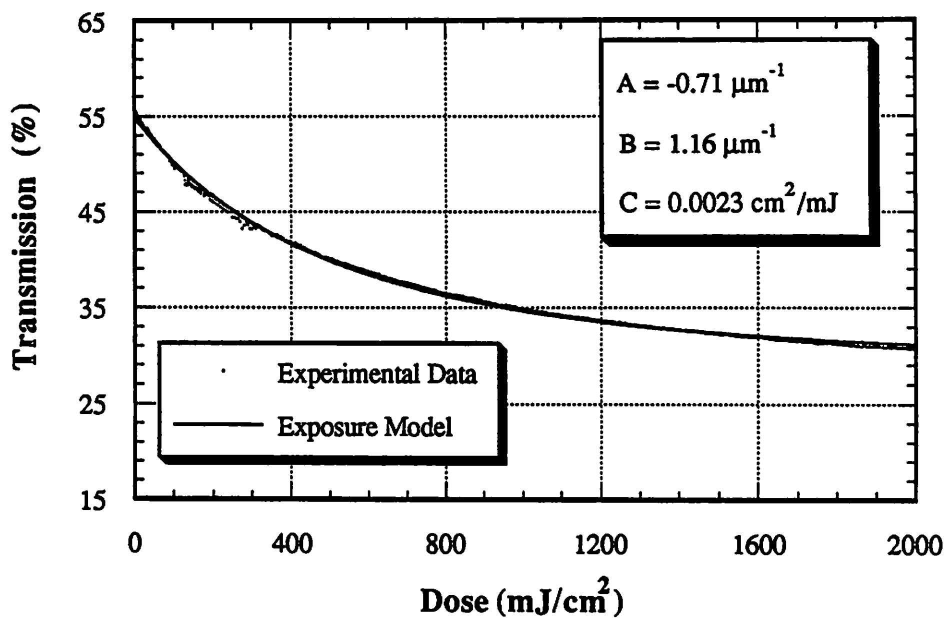


**Figure 6.3:** Change in IR absorbance at 1560 $cm^{-1}$ versus exposure dose for SNR 248 resist.

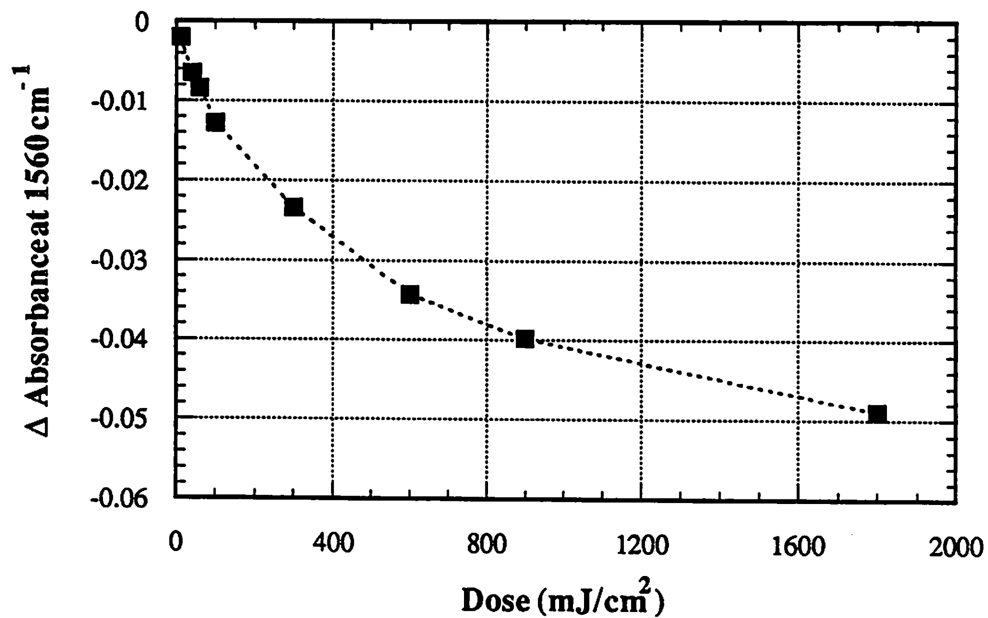

**Figure 6.4:** Experimental transmission measurements of both the standard SNR 248 resist and SNR 248 with three times the amount of acid generator.

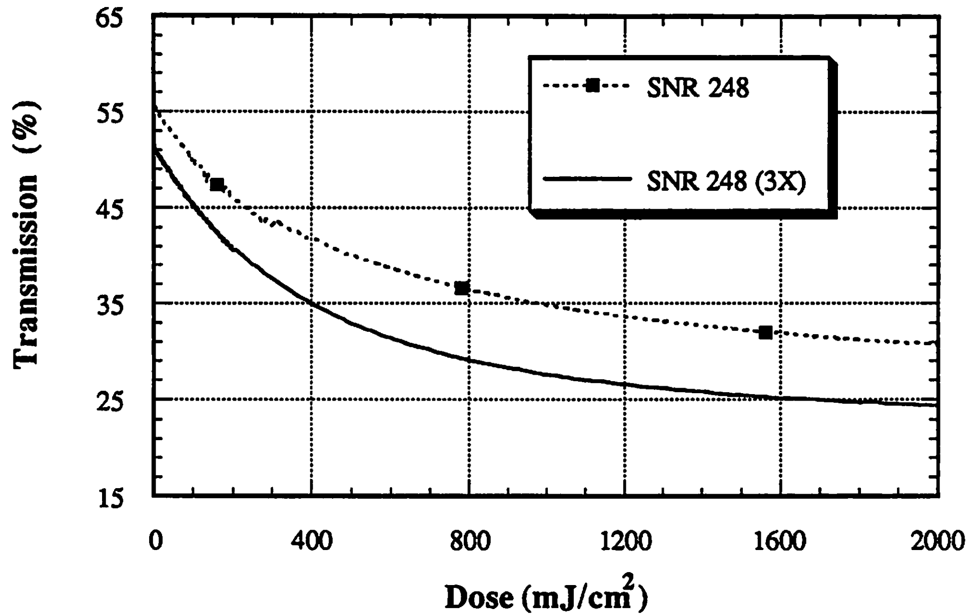


**Figure 6.5:** Experimental transmission measurements of both SNR 248 resist and XP-8798 resist, an earlier version of SNR 248 resist with a novolak resin.

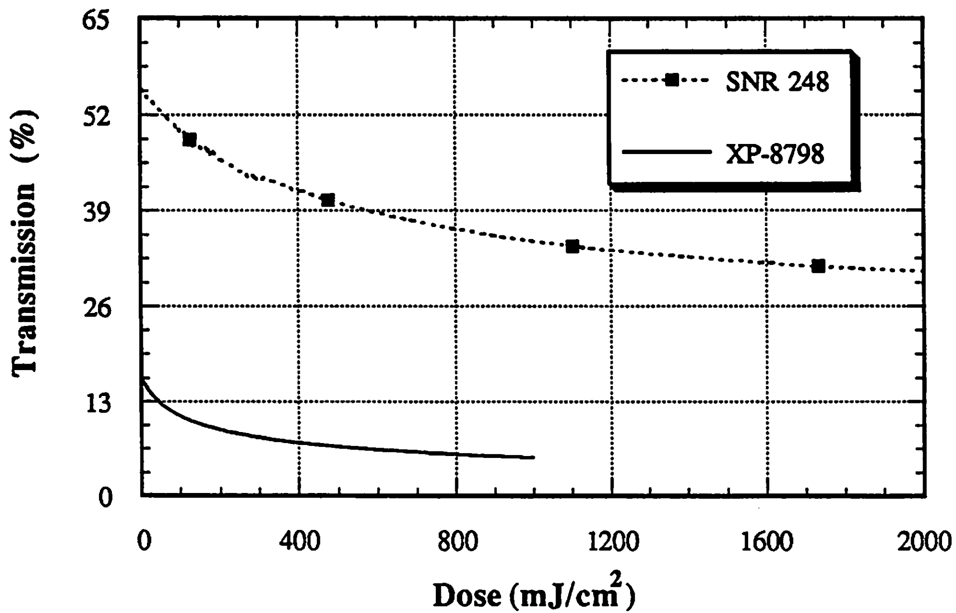

**Figure 6.6:** Part of the melamine crosslinking agent consisting of an unactivated and an activated crosslinking site.

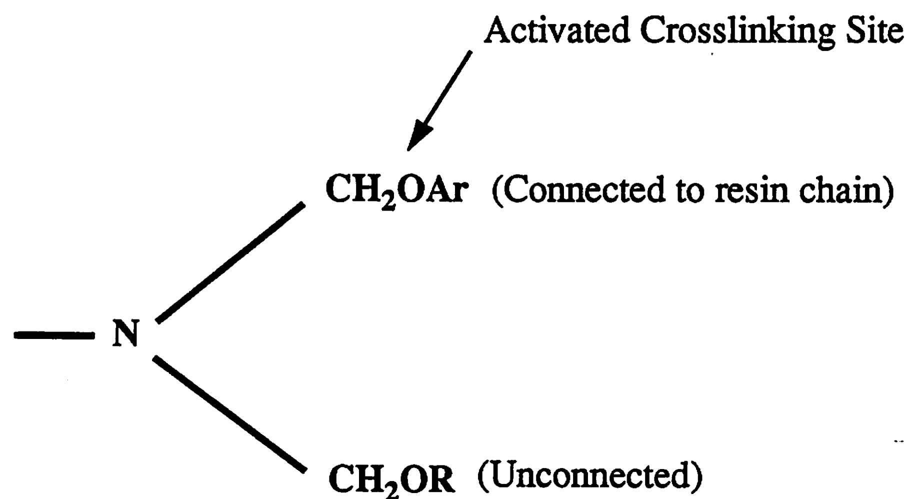


**Figure 6.7:** Proposed reaction mechanism for the crosslinking reaction in SNR 248 resist [10].

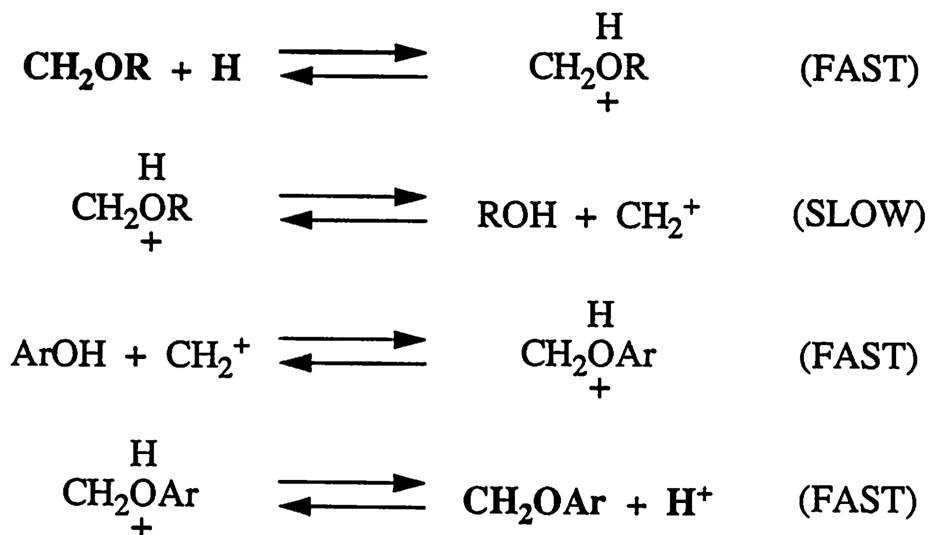

**Figure 6.8:** FTIR difference spectra of SNR 248 resist for doses of 4 and 6 mJ/cm$^2$ with a post-exposure bake of 150°C for 120 seconds.

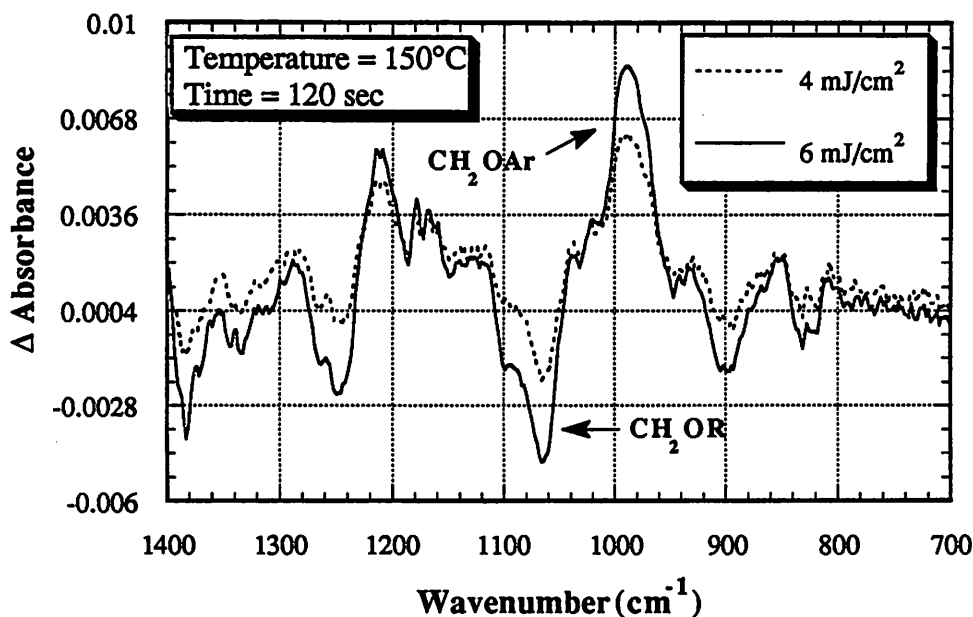


**Figure 6.9:** Comparison of FTIR measurements and the kinetic bake model for SNR 248 resist at bake temperatures of a) 130°C, b) 140°C, and c) 150°C.

a)

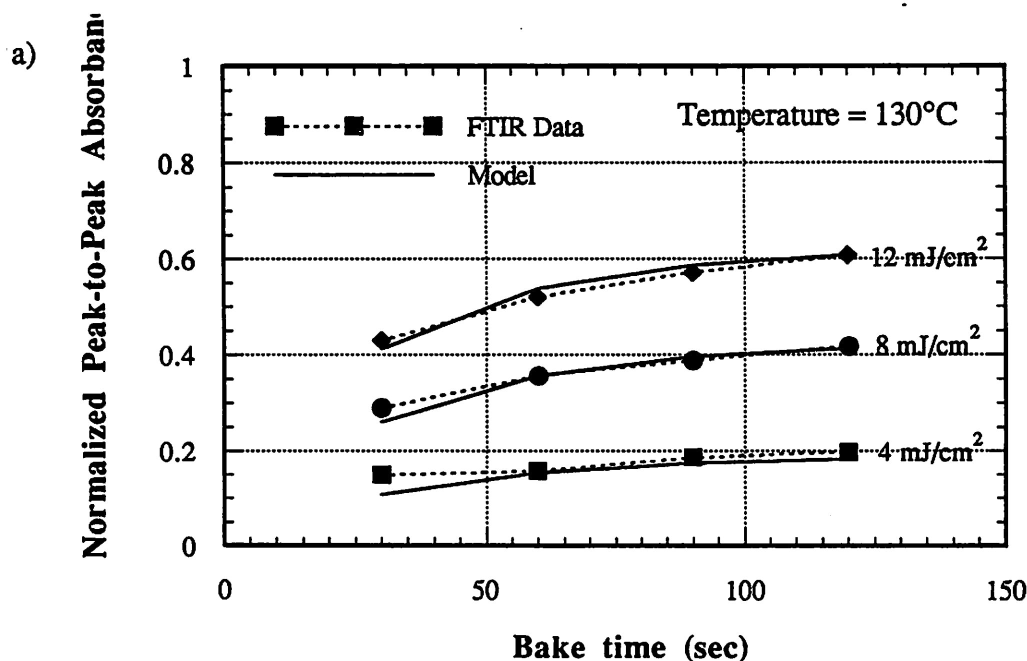

b)

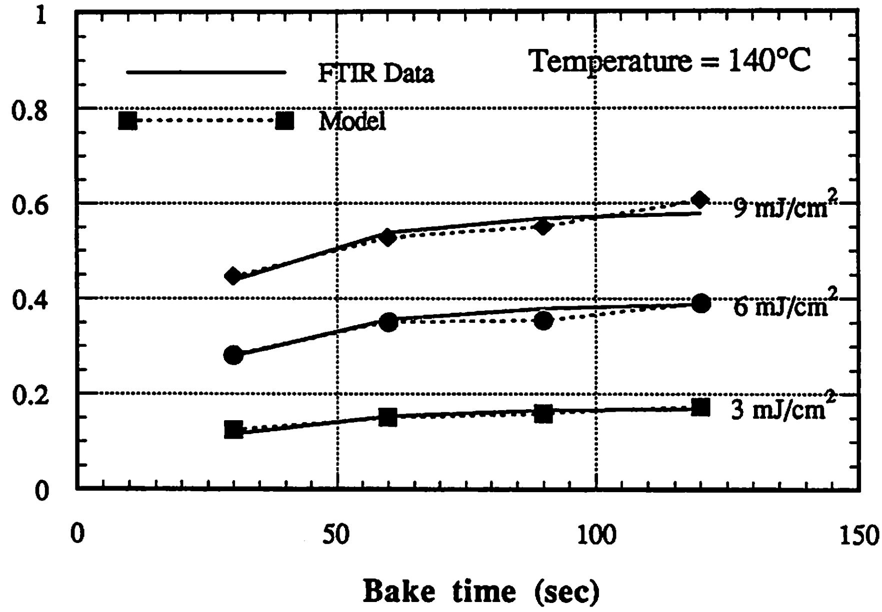


c)

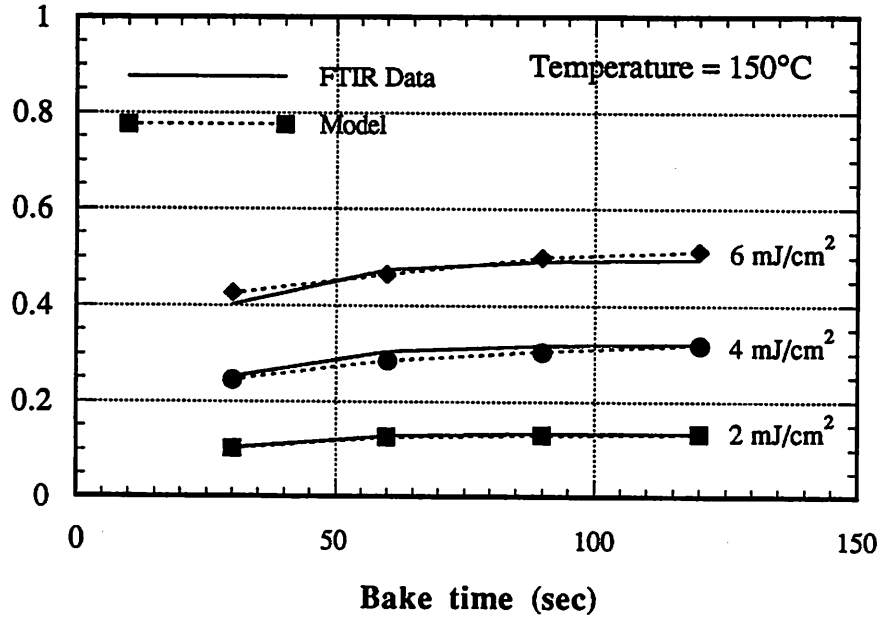

**Figure 6.10:** Reaction rate coefficients as a function of bake temperature including the Arrhenius fit to the data with a pre-exponential and an activation energy.

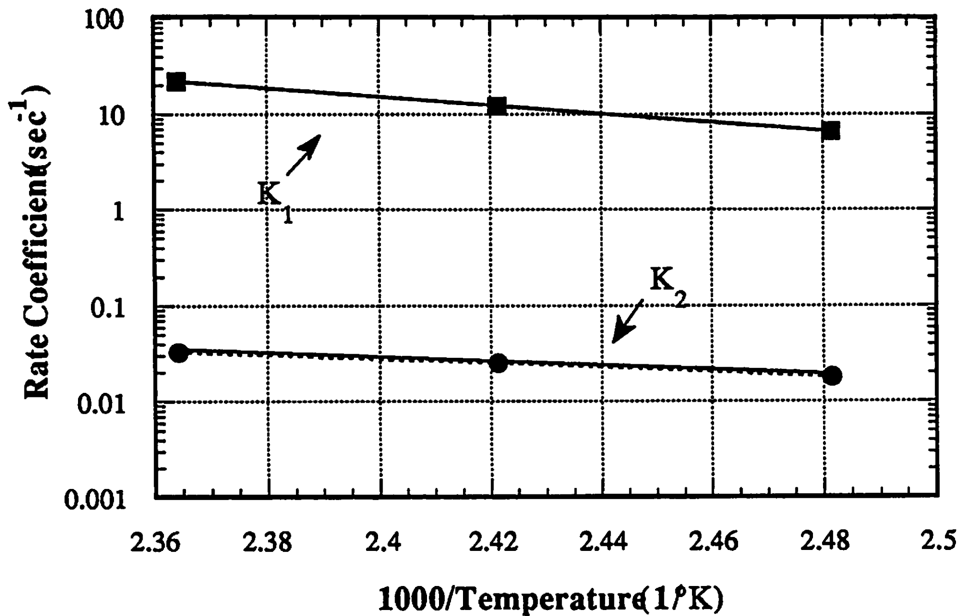


**Figure 6.11:** Dissolution rate measurements and the corresponding fit using the molecular weight based dissolution model for SNR 248 resist with post-exposure bakes of 130°C and 140°C for 60 seconds.

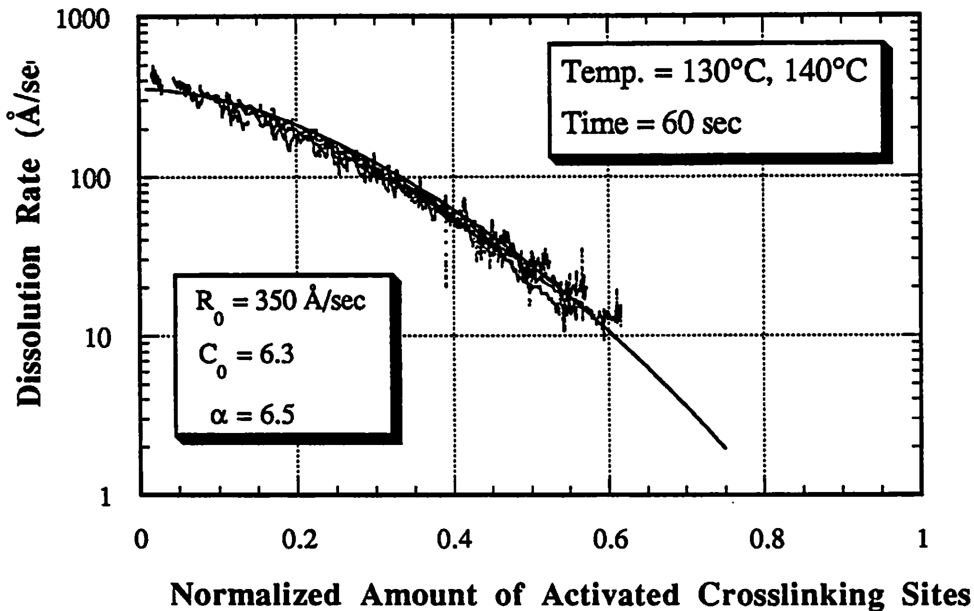

**Figure 6.12:** Resist development profiles of SNR 248 resist from a 0.4 μm equal lines and spaces pattern with NA = 0.42 and a post-exposure bake of 130°C for 60 seconds. Results are obtained from a) experiment using a dose of 30 mJ/$cm^2$ and b) simulation using a dose of 42 mJ/$cm^2$.

a)

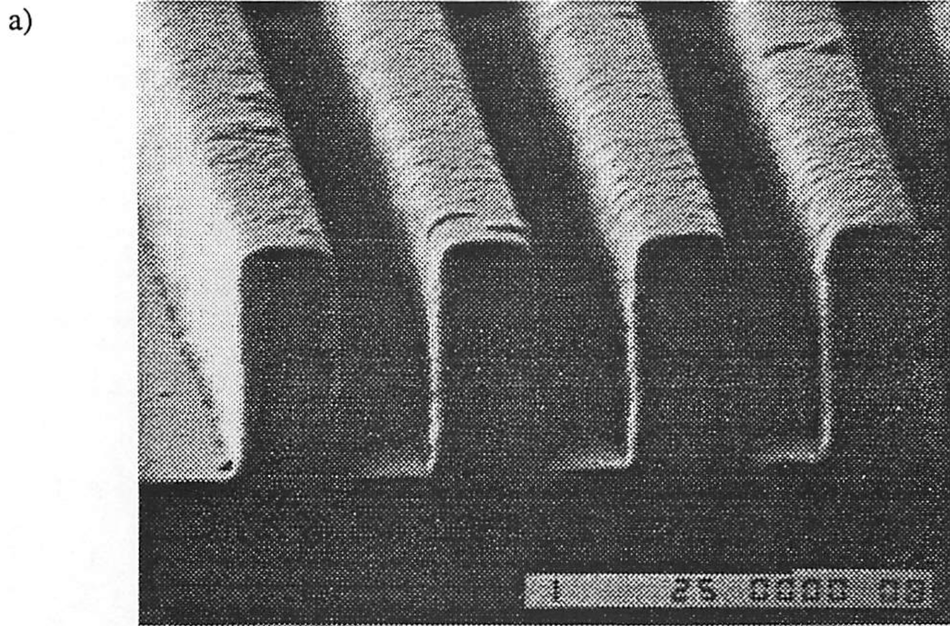

b)

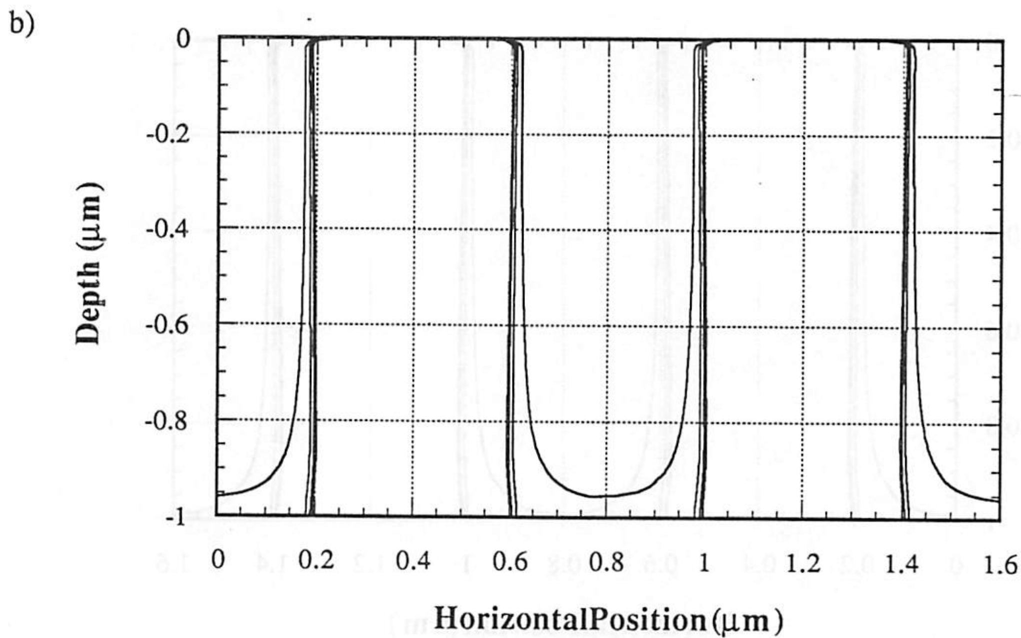

**Figure 6.13:** Resist development profiles of SNR 248 resist from a 0.4 μm equal lines and spaces pattern with NA = 0.42 and a post-exposure bake of 140°C for 60 seconds. Results are obtained from a) experiment using a dose of 18 $mJ/cm^2$ and b) simulation using a dose of 25.2 $mJ/cm^2$.

a)

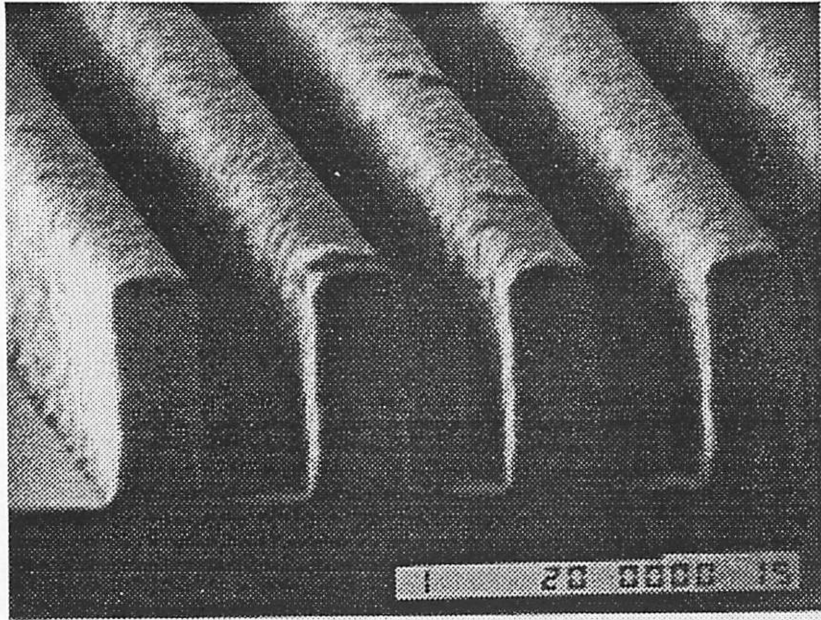


b)

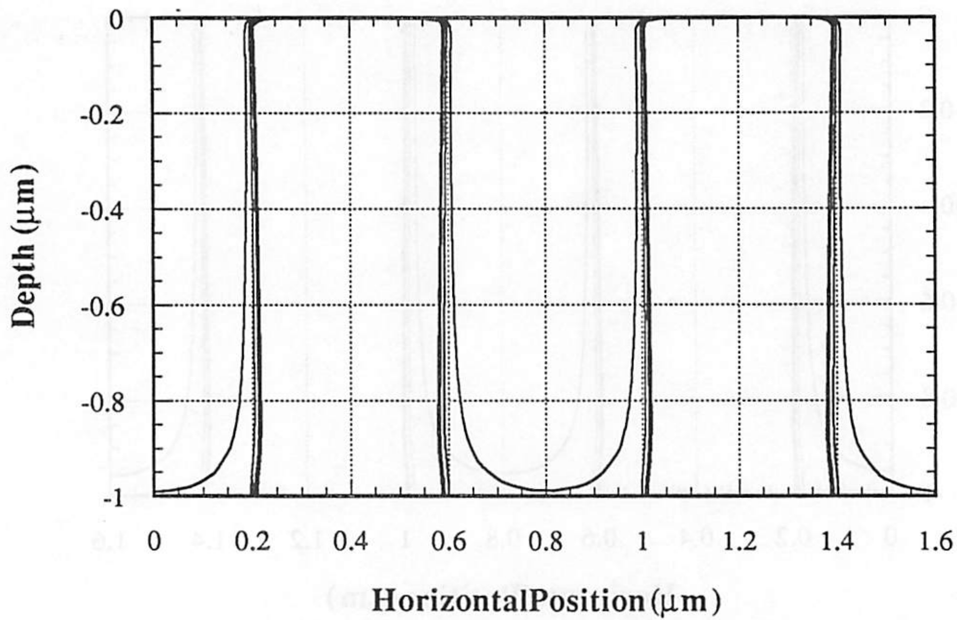

**Figure 6.14:** Resist development profiles of SNR 248 resist from a 0.3 μm equal lines and spaces pattern with NA = 0.42 and a post-exposure bake of 140°C for 60 seconds. Results are obtained from a) experiment using a dose of 18 mJ/cm$^2$ and b) simulation using a dose of 25.2 mJ/cm$^2$.

a)

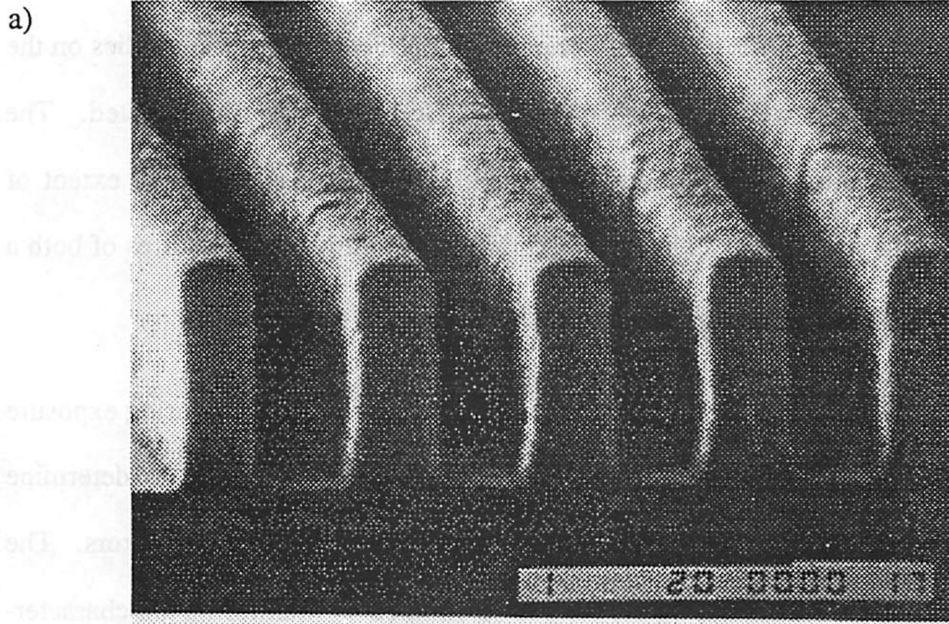

b)

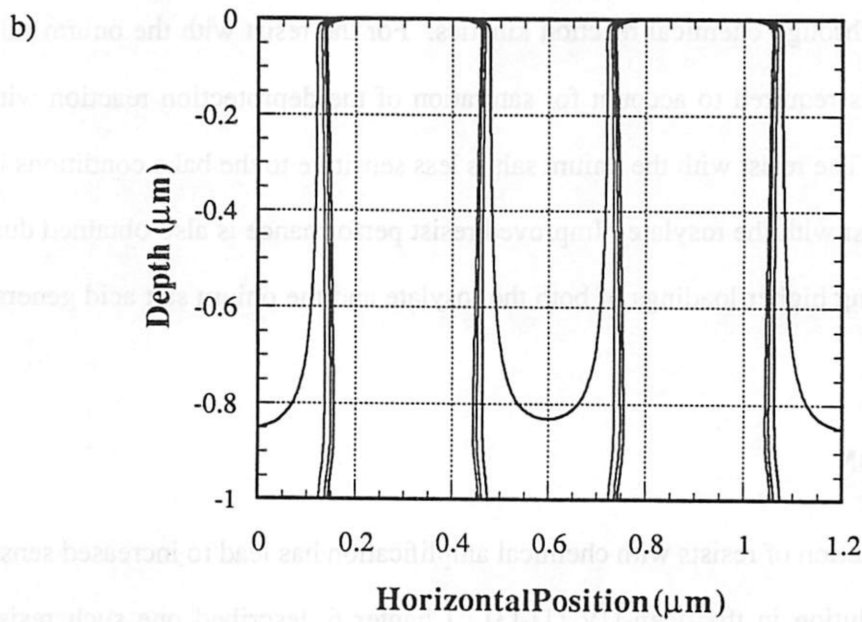

# CHAPTER 7

# MODELING OF A T-BOC RESIST

The exposure and post-exposure bake of a chemical amplification resist that relies on the acid catalyzed removal of a tert-butyloxycarbonyl (t-BOC) group are investigated. The effects of the acid generator on the production of acid during exposure and the extent of deprotection during the bake are examined using different weight percent mixtures of both a 2,6 dinitrobenzyl tosylate and a triarylsulfonium salt.

The generation of acid is monitored by measuring the resist transmission during exposure as well as through FTIR spectroscopy. The experimental results are used to determine absorption coefficients and acid generation rate coefficients for both acid generators. The extent of deprotection that occurs during the bake is determined by monitoring the characteristic FTIR absorbance band at 1760 $cm^{-1}$ over a range of exposure doses, bake temperatures, and bake times. The extent of deprotection is related to the local acid concentration generated during exposure through chemical reaction kinetics. For the resist with the onium salt, an acid loss reaction is required to account for saturation of the deprotection reaction with increasing bake time. The resist with the onium salt is less sensitive to the bake conditions in comparison to the resist with the tosylate. Improved resist performance is also obtained during the bake when using higher loadings of both the tosylate and the onium salt acid generators.

## 7.1 INTRODUCTION

The recent introduction of resists with chemical amplification has lead to increased sensitivity with good resolution in the deep-UV [1]-[3]. Chapter 6 described one such resist, Shipley SNR 248, in which acid catalyzed crosslinking during the post-exposure bake leads

to a negative-tone resist image [3]. The improvement in performance from these chemical amplification resists, however, has been accompanied by increased complexity in both the resist chemistry and processing. With the added complexity, the relationship between processing parameters and resist performance has become more difficult to ascertain. Detailed modeling studies can lead to both an improved understanding of the physical and chemical mechanisms that dominate the resist behavior and to models which can be used to simulate resist development profiles under a variety of processing conditions.

Mechanistic modeling approaches for the negative-tone SNR 248 resist have demonstrated great success [4] -[8] (see Chapter 6). However, a complimentary positive resist technology is needed for deep-UV lithography. One positive-acting resist based on the acid catalyzed removal of a t-BOC protecting group during the post-exposure bake has shown good promise as a high performance deep-UV resist [1][2]. However, the many factors that need to be considered in optimization of this resist process, including the choice of acid generator type and concentration, leads to a difficult problem to address. By gaining an understanding of the mechanisms that affect the resist behavior, the resist design and optimization process can be greatly simplified.

## 7.2 RESIST CHEMISTRY, PREPARATION, AND PROCESSING

The resist is composed of a poly(t-BOC-styrene sulfone) resin and an acid generator. Upon heating in the presence of acid, the t-BOC protecting group is catalytically removed from the resin leaving a poly(hydroxystyrene sulfone) matrix. The resin structure and the deprotection reaction are shown in Figure 7.1 [1]. With the removal of the t-BOC group, the resin becomes soluble in aqueous developer. The difference in solubility may be exploited to pattern images in the resist through the selective introduction of a catalytic acid. Deep-UV radiation produces an acid from the acid generator through a photolytic reaction. Both 2,6-dinitrobenzyl tosylate and triphenylsufonium hexafluoroarsenate were used as acid genera-

tors in this study. The structure and the proposed acid generation reactions for the tosylate [9] and the onium salt [1] are shown in Figure 7.2.

In addition to the acid catalyzed deprotection reaction, the resin will also undergo chain scission at the sulfone group upon exposure leading to a decrease in molecular weight [1]. This effect will act in concert with the deprotection reaction to increase the resist solubility in the exposed regions. However, since the sensitivity of the resin alone to deep-UV patterning has been shown to be greater than 1 J/cm$^2$ [1], it is expected that the extent of deprotection will be the dominant factor in determining the resist dissolution characteristics at lithographically useful exposure doses.

The resist was prepared by first dissolving the resin in cyclohexanone in a ratio of 1 gram of resin to 8 milliliters of solvent. Different amounts of both acid generators were then dissolved in the solution to examine the effect of acid generator type and concentration on resist performance. The mixtures that were investigated were 6 and 12 weight percent of tosylate, and 2.5 and 5 weight percent of onium salt. The resist was then applied to the substrate with spin speeds of 2500 to 5000 rpm for 30 seconds. The resist was spun onto quartz substrates for the transmission experiments and double-polished silicon wafers for the FTIR measurements. The spin was followed by a pre-exposure bake of 105°C for 2 minutes to remove excess solvent. The exposures were done with an excimer laser at a wavelength of 248 nm. Following the exposure, the resist was baked on a hot plate at temperatures ranging from 95°C to 115°C to drive the catalytic deprotection reaction.

## 7.3 MODELING THE EXPOSURE

Modeling of photoinduced acid generation in chemical amplification resists by fitting Dill's ABC parameters [10] to measurements of resist transmission during exposure has been

previously demonstrated for the acid hardening resist, SNR 248, in Chapter 6. In this model, the absorption coefficient, α, is described by:

$$\alpha(z,t) = AM(z,t) + B \qquad [7.1]$$

where M is the normalized concentration of the acid generator, z is the depth into the resist, and t is the exposure time. The photolytic conversion of the acid generator to acid is described by:

$$\frac{\partial}{\partial t}M(z,t) = -I(z,t)M(z,t)C \qquad [7.2]$$

where I is the illumination intensity and C is the reaction rate coefficient. In this model, 1-M represents the normalized concentration of the photo-generated acid.† It is important to note when using this model, that if other reactions occur simultaneously with the acid generation reaction during exposure, the expression for α may be more complex than equation [7.1].

Measurements of the transmission versus exposure dose were made by spinning the resist onto a quartz substrate and then monitoring the transmission as the resist was exposed as described in Chapter 5. Typical results are shown in Figure 7.3a for the 12% tosylate mixture and in Figure 7.3b for the 2.5% onium salt mixture as well as the resin alone. The resin demonstrates a strong darkening behavior independent of acid generation. This effect, which must be accounted for in the exposure modeling, can be attributed in part to the chain scission reaction of the resin. The following sections describe the determination of α and C of equations [7.1] and [7.2] for the resist with both the tosylate and the onium salt acid generators.

†. This assumes that all of the acid generator can be converted to acid.

### 7.3.1 Tosylate Exposure Model

While the transmission of the 12% tosylate mixture in Figure 7.3a was measured over a range of 2500 mJ/cm$^2$, the lithographically useful range for this resist is below 100 mJ/cm$^2$ [11]. Over this smaller range, the change in the transmission, and thus the change in the absorption coefficient, is quite small. Therefore, the exposure model for the tosylate acid generator can be simplified by considering the absorption coefficient as essentially constant ($A = 0$). This result contrasts with standard positive resists where significant bleaching of the resist can occur during typical exposure doses ($A > B$). To determine the value of $\alpha$, the ***SAMPLE*** program was modified to perform a rigorous simulation of the resist/quartz substrate stack transmission as described in Chapter 5. Values of $\alpha = 0.63\ \mu m^{-1}$ and $\alpha = 1.06\ \mu m^{-1}$ resulted in the best fit to the experimental transmission near the beginning of exposure for the 6% and 12% tosylate mixtures, respectively.

The measured absorption coefficient consists of two components given by:

$$\alpha = \alpha_s + \alpha_r \qquad [7.3]$$

where $\alpha_s$ is the component of the absorption coefficient due to the acid generator and $\alpha_r$ is the component due to the resin. From the resin transmission curve in Figure 7.3b, the absorption coefficient of the resin in the range of ~100 mJ/cm$^2$ is $\alpha_r \approx 0.1\ \mu m^{-1}$. Consequently, the ratio of the $\alpha_s$'s for the two weight percent mixtures is calculated to be 1.8, slightly lower than the expected value of 2, the ratio of the acid generator concentrations. This discrepancy may result from experimental error or other effects such as a reduction in resist density from the introduction of the acid generator within the resist.

The last step in modeling the exposure was to determine the rate coefficient for acid generation, C. The resist transmission curve in Figure 7.3a has three distinct regions: 0 to 100 mJ/cm$^2$ where the resist initially darkens, 100 to 600 mJ/cm$^2$ where the resist bleaches,

and the region beyond 600 $mJ/cm^2$ where the resist again darkens with increasing exposure. The final region beyond 600 $mJ/cm^2$ can be attributed to the darkening reaction in the resin seen in Figure 7.3b. However, it is impossible to determine directly from the transmission data the region that corresponds to the acid generation reaction.

For this reason, FTIR spectroscopy was used to monitor the acid generation in the resists with the tosylate acid generator. The spectra were obtained in transmission mode using a silicon substrate polished on both sides as described in Chapter 5. To examine the changes that occurred during exposure, the initial spectrum of the resist before exposure was subtracted from the spectra obtained after exposure. Figure 7.4 shows typical results for the 6% tosylate mixture with exposure doses of 50 and 500 $mJ/cm^2$. The decrease in absorbance near 1540 $cm^{-1}$ corresponds to the loss of the nitro group of the tosylate during conversion to acid (see Figure 7.2a). By dividing the peak size for each dose by the largest peak size obtained at high exposures, the normalized concentration of acid as a function of exposure dose was determined.

The FTIR results were simulated in ***SAMPLE*** by averaging the local concentration of acid calculated using the previously determined values of $\alpha$ over the resist thickness for a range of rate coefficient values. Figure 7.5 shows the FTIR results as well as the ***SAMPLE*** simulation for the resist with the 6% tosylate. The best fit to the FTIR data occurred with $C \approx 0.0045\ cm^2/mJ$ for both the 6% and 12% tosylate mixtures. As expected, the rate coefficient was essentially independent of acid generator concentration.

Since the acid generation reaction in Figure 7.5 reaches completion near 1000 $mJ/cm^2$, the bleaching of the resist, which dominates the middle region of the transmission curve, has been attributed to the generation of acid. As mentioned previously, the resist darkening,

observed at high doses, results the darkening reaction in the resin itself. At this point, the cause of the initial decrease in transmission has yet to be determined.

### 7.3.2 Onium Salt Exposure Model

Similar methods were used to determine the exposure model parameters for the resist sensitized with the onium salt. As shown in Figure 7.3b, the change in the transmission of the resist with the 2.5% onium salt mixture was also quite small over the lithographically useful range of exposure of less than 50 mJ/cm$^2$ [11]. As a result, constant values of $\alpha$ = 0.41 $\mu m^{-1}$ and $\alpha = 0.55$ $\mu m^{-1}$ were obtained for the initial stages of exposure for the 2.5% and 5% onium salt mixtures, respectively. By using a resin absorption coefficient of $\alpha_r$ = 0.1 $\mu m^{-1}$ as before, the ratio of the $\alpha_s$'s is found to be 1.45, again less than the expected ratio of 2.

Since FTIR spectroscopy yielded no measurable peaks with which to monitor acid generation as with the tosylate acid generator, the rate coefficient C was determined solely from transmission data. The difficulty of this approach is apparent from Figure 7.3b where the darkening reaction in the resin dominates the transmission curve for the 2.5% onium salt mixture. By assuming that the quantum yield of the acid generator does not depend on the resin, however, the value of C can be determined by measuring the transmission versus exposure dose of the acid generator in a resin matrix where the resin alone has only a weak darkening reaction. For this purpose, a 2:1 t-BOC styrene:styrene copolymer was used. Figure 7.6 shows the transmission of the resin alone and a 5 weight percent onium salt mixture. With this resin, changes in resist transmission independent of the resin darkening can be observed for the 5% onium salt mixture. This change in transmission can be attributed to the acid generation and thus provides a good measure of the rate coefficient, C. To determine C, Dill's ABC parameters were first fit to the transmission data for the resin alone. With the assumption that the darkening reaction in the resin occurs simultaneously with, but indepen-

dent of, the acid generation reaction, the ABC values for the resin were held constant and a second set of ABC values were fit to the transmission data for the 5% onium salt mixture. An excellent fit was obtained as shown in Figure 7.6 using A = -0.24 $\mu m^{-1}$, B = 0.77 $\mu m^{-1}$ C = 0.0011 $cm^2/mJ$ for the acid generation reaction. With the above assumptions, the rate coefficient C = 0.0011 $cm^2/mJ$ also applies to the 2.5% and 5% onium salt mixtures in the poly(t-BOC-styrene sulfone) resin.

The complete set of parameters for modeling the exposure of the resist with both the tosylate and onium salt acid generators are summarized in Table 7.1.

| Acid Generator | $\alpha(\mu m^{-1})$ | $C(cm^2/mJ)$ |
|---|---|---|
| 6% tosylate | 0.63 | 0.0045 |
| 12% tosylate | 1.06 | 0.0045 |
| 2.5% onium salt | 0.41 | 0.0011 |
| 5% onium salt | 0.55 | 0.0011 |

**Table 7.1:** Exposure model parameters.

## 7.4 MODELING THE BAKE

The models determined for the resist exposure can be used to calculate the local concentration of acid at any depth within the resist as a function of exposure dose, resist thickness, and substrate reflectivity. To model the post-exposure bake, the catalytic acid concentration must be related to the local amount of deprotection, the dominant factor in determining the resist dissolution rate. The models are defined in terms of the differential equations which

describe the chemical reactions that occur during the bake. These kinetic models are easily incorporated into the *SAMPLE-ARK* program described in Chapter 3 to simulate the deprotection reaction.

Experimental measurements of the deprotection reaction were made with FTIR spectroscopy. The spectra of Figure 7.7 obtained before and after the bake are typical. The peak at 1760 $cm^{-1}$, which decreases during the bake, corresponds to the carbonyl bond of the t-BOC protecting group that is removed during the deprotection reaction (see Figure 7.1). The extent of deprotection is quantified by fitting a baseline to the spectra in the region of 1760 $cm^{-1}$ and integrating the area under this peak using the FTIR software package described in Chapter 5. The peaks near 1150 $cm^{-1}$ and 1280 $cm^{-1}$ are also indicative of the deprotection reaction. However, the peak at 1760 $cm^{-1}$ is expected to yield more accurate results because it is isolated from other absorbing bonds. It is important to note that the results obtained with FTIR are bulk measurements that are averaged over the entire thickness of the resist. Therefore, in order to compare the bake models with experimental results, the simulations in *SAMPLE-ARK* must also be averaged over the resist thickness.

A matrix of experiments was done to investigate the effects of acid generator type and concentration, bake temperature and time, and exposure dose (acid concentration) on the deprotection reaction. Typical results from the FTIR measurements for bake temperatures of 95, 105, and 115°C are shown for the 12% tosylate mixture in Figures 7.8a, 7.8b, and 7.8c and for the 2.5% onium salt mixture in Figures 7.9a, 7.9b, and 7.9c. It is evident from the differences between these two results that the kinetics of the deprotection reaction depend strongly upon the acid generator type. The modeling of these two distinct types of reactions is discussed in detail in the following sections.

### 7.4.1 Tosylate Bake Model

From the results shown in Figure 7.8, the deprotection reaction appears to proceed towards complete deprotection at a rate that increases as the exposure dose, and thus the acid concentration, is increased. Further FTIR measurements confirmed that almost complete deprotection was obtained after a 20 minute bake for all exposure doses. This type of behavior is consistent with a simple catalytic reaction in which the acid is regenerated after each deprotection reaction. From chemical reaction kinetics, a simple model for such a reaction would be:

$$\frac{\partial}{\partial t}[T] = -k_1 [T] [A] \qquad [7.4]$$

$$\frac{\partial}{\partial t}[A] = 0 \qquad [7.5]$$

where [T] is the normalized concentration of t-BOC groups (1-[T] is the normalized amount of deprotection), [A] is the normalized concentration of acid, and $k_1$ is the reaction rate coefficient. Equation 7.4 describes the removal of the t-BOC protecting group while equation 7.5 describes the acid loss, assumed in this case to be zero. Simulated results from the modified version of ***SAMPLE-ARK*** with $k_1 = 0.08\ sec^{-1}$ are compared with the experimental results in Figure 7.10. It is evident from the fit that this simple model is unable to replicate the spacing between the curves for the different doses.

The curves for the different doses represent different concentrations of acid within the resist at the start of the bake. Therefore, the spacing between the curves can be increased by raising the acid concentration term in equation [7.5] to a power greater than one. This modi-

fication to the simple catalytic model was required to describe the crosslinking reaction in SNR 248 resist in Chapter 6 as well. The resulting model is described by:

$$\frac{\partial}{\partial t}[T] = -k_1 [T] [A]^m \qquad [7.6]$$

$$\frac{\partial}{\partial t}[A] = 0 \qquad [7.7]$$

If it is assumed that the resist dissolution rate is primarily determined by the extent of deprotection, then a higher value of the acid exponent, m, will lead to increased resist contrast. Figure 11 compares the simulated results using values of $m = 1.8$ and $k_1 = 0.6\ sec^{-1}$ with the experimental data.

While the spacing between the curves for the model is generally consistent with the spacing for the experimental data, there is a flattening or bowing of the experimental data during the initial stages of the bake that does not coincide with the shape of the model curves. Examination of the experimental results in Figure 7.8 reveals that this bowing effect increases at higher bake temperatures. One mechanism that may account for this involves an initial reaction between the acid and the t-BOC group to form an intermediate species. In a second reaction, the protecting group is removed and the acid is regenerated. Depending on the relative sizes of the rate coefficients for these two reactions, this mechanism can result in a slow rate of deprotection during the initial stages of the bake as the concentration of the intermediate begins to build. If the two reactions have different activation energies, then the amount of flattening in the curves will depend on the bake temperature. At this point, this speculative mechanism has not been included in the deprotection model.

The model of equations [7.6] and [7.7] was also applied to the 6% tosylate mixture. A good fit for the 105°C bake, shown in Figure 7.12, was obtained with $m = 1.3$ and $k_1 = 0.125\ sec^{-1}$. The value of the acid exponent, m, for the 6% tosylate mixture is significantly

smaller than that for the 12% tosylate mixture. Although the chemical cause is not readily apparent, this effect suggests that higher contrast can be obtained when a higher loading of the tosylate acid generator is used. This result has in fact been observed experimentally [11]. However, the increase in contrast cannot be attributed unambiguously to the observed increase in m since the increased loading of the acid generator itself may affect the resist dissolution characteristics.

A summary of the rate coefficients and values of m obtained as a function of bake temperature and acid generator concentration is given in Table 7.2.

| Tosylate Conc. | Bake Temp(°C) | $k_1(sec^{-1})$ | m |
|---|---|---|---|
| 6 wt % | 95 | 0.031 | 1.2 |
| | 105 | 0.125 | 1.3 |
| | 115 | 0.45 | 1.4 |
| 12 wt % | 95 | 0.20 | 1.8 |
| | 105 | 0.60 | 1.8 |
| | 115 | 2.05 | 1.8 |

**Table 7.2:** Bake model parameters for the tosylate acid generator.

### 7.4.2 Onium Salt Bake Model

While the deprotection reaction with the tosylate acid generator proceeded towards complete deprotection, the saturation of the experimental curves of Figure 7.9 over the range of measured bake times indicates that the deprotection reaction was quenched before complete

deprotection was attained with the onium salt acid generator. It is postulated, therefore, that the acid that catalyzed the reaction was rendered inactive during the bake just as was the case for SNR 248 resist in Chapter 6. The mechanism for this acid loss is not yet known, but it likely results from reactions with other contaminants within the resist which neutralize the acid. A first order reaction was assumed for this acid loss. Combining the acid loss reaction with the deprotection reaction from the tosylate model results in a model given by:

$$\frac{\partial}{\partial t}[T] = -k_1 [T] [A]^m \quad [7.8]$$

$$\frac{\partial}{\partial t}[A] = -k_2 [A] \quad [7.9]$$

where $k_2$ is the rate coefficient for the acid loss reaction.

Figure 7.13 compares the model to the experimental results from two independent measurements for the 2.5% onium salt mixture with a bake temperature of 105°C. A good fit is obtained with $m = 1.2$, $k_1 = 16.7$ sec$^{-1}$, and $k_2 = 0.035$ sec$^{-1}$. The fit obtained using $m = 1.6$, $k_1 = 580.9$ sec$^{-1}$, and $k_2 = 0.029$ sec$^{-1}$ for the 5% onium salt mixture at a bake temperature of 105°C is shown in Figure 14. Once again, the acid exponent, m, increased as the loading of the acid generator was increased. The deprotection model parameters for the onium salt acid generator are summarized in Table 7.3.

| Onium Salt Conc. | Bake Temp(°C) | $k_1(sec^{-1})$ | $k_2(sec^{-1})$ | m |
|---|---|---|---|---|
| 2.5 wt % | 95 | 19.7 | 0.026 | 1.3 |
| | 105 | 16.7 | 0.035 | 1.2 |
| | 115 | 31.7 | 0.033 | 1.3 |
| 5 wt % | 95 | 130.9 | 0.032 | 1.4 |
| | 105 | 580.9 | 0.029 | 1.6 |
| | 115 | 700.0 | 0.026 | 1.7 |

**Table 7.3:** Bake model parameters for the onium salt acid generator.

## 7.5 COMPARISON OF ACID GENERATOR PERFORMANCE

The plots of deprotection versus bake time of Figures 7.8 and 7.9 are beneficial for comparing the performance of the two acid generators. While these plots do not include any information concerning the resist dissolution, some useful results can still be inferred.

Sensitivity, a good quantitative measure of throughput, is an important parameter for chemical amplification resists. For the bake times shown in Figures 7.8 and 7.9 the resist with the onium salt demonstrates a higher sensitivity since the same amount of deprotection occurs at a lower exposure dose. However, the deprotection reaction saturates in the resist with the onium salt. Since the deprotection reaction proceeds towards completion in the tosylate sensitized resist, higher values of sensitivity are expected for the resist with the tosylate at increased bake times. In theory, the achievable sensitivity in this resist should only be limited by lateral diffusion of the acid at extreme bake times.

The process latitude of the resist with respect to the bake conditions also plays an important role in rating the resist performance. In this case, as a result of the acid loss reaction, the resist with the onium salt is superior in all respects. The amount of deprotection in the resist with the onium salt remains essentially constant regardless of the bake temperature for a given exposure dose (see Figures 7.9a, b, and c). This result can be compared with the tosylate sensitized resist where the exposure dose changes significantly to achieve a similar amount of deprotection at different bake temperatures (see Figures 7.8a, b, and c). Apparently, the acid loss reaction in the resist with the onium salt tracks the temperature behavior of the deprotection reaction with a similar activation energy. The acid loss reaction also reduces the sensitivity to the bake time for the resist with the onium salt by saturating the deprotection reaction at a dose-dependent level. In the resist with the tosylate acid generator, the amount of deprotection continuously changes as the bake time increases.

## 7.6 SUMMARY

The exposure and post-exposure bake of a resist composed of a poly(t-BOC-styrene sulfone) resin with both a tosylate and an onium salt as photo-acid generators have been investigated. Optical transmission and FTIR absorbance measurements have been used to monitor the extent of acid production during the exposure and the amount of deprotection during the bake. As observed from the experimental results, the resist behavior was strongly dependent on both acid generator type and concentration. The experimental measurements were used to develop models based upon chemical reaction kinetics for both the exposure and post-exposure bake steps.

Dill's exposure model was applied to the generation of acid during exposure. The model consisted of an absorption coefficient, $\alpha$, and an acid generation rate coefficient, C. For both acid generators, the change in resist transmission was small over lithographically useful exposure doses such that the absorption coefficient was modeled as a constant ($A = 0$). Resin

darkening observed at large exposures of the resin alone was accounted for in the modeling of both acid generators. Because of the complex transmission behavior of the resist with the tosylate, the decrease in the nitro-group absorbance at 1540 $cm^{-1}$ in the FTIR spectrum was used to determine the acid generation rate coefficient. To determine the rate coefficient for acid generation with the onium salt, a t-BOC styrene:styrene copolymer resin was used to reduce the dominance of resin darkening on the resist transmission.

The carbonyl absorption band at 1760 $cm^{-1}$ in the FTIR spectrum was used to monitor the deprotection reaction over a range of exposure doses, bake temperatures, and bake times. From the measurements, the deprotection proceeded to completion with the tosylate acid generator, but saturated at a dose-dependent level with the onium salt acid generator. In addition, the amount of deprotection depended only weakly on both bake temperature and bake time for the resist with the onium salt when compared with the tosylate. Chemical reaction kinetics were used to relate the local concentration of acid generated during the exposure to the amount of deprotection that occurred during the bake. The tosylate sensitized resist was modeled with a single deprotection reaction where the rate of deprotection was proportional to the acid concentration to the $m^{th}$ power. The value of m for all mixtures was always greater than one. Modeling of the resist with onium salt required an additional acid loss reaction to account for the dose-dependent saturation of experimental data. It was observed that the performance of the resist during the bake, as determined by the acid exponent m, improved as the acid generator loading was increased.

## REFERENCES


[1] R. Tarascon, E. Reichmanis, F. Houlihan, A. Shugard, and L. Thompson, "Poly(t-BOC-styrene sulfone)-Based Chemically Amplified Resists for Deep-UV Lithography," *Polymer Engineering and Science*, vol. 29, no. 13, pp. 850-855, Mid July, 1989.

[2] C. Willson, H. Ito, J. Frechet, T. Tessier, and F. Houlihan, "Approaches to the Design of Radiation-Sensitive Polymeric Imaging Systems with Improved Sensitivity and Resolution," *J. Electrochem. Soc.*, vol. 133, no. 1, pp. 181-187, January 1986.

[3] J. Thackeray, G. Orsula, E. Pavelchek, D. Canistro, L. Bogan, A. Berry, and K. Graziano, "Deep UV ANR Photoresists for 248 nm Excimer Laser Photolithography," *SPIE Advances in Resist Technology and Processing VI*, vol. 1086, pp. 34-47, 1989.

[4] D. Seligson, S. Das, H. Gaw, and P. Pianetta, "Process Control with Chemical Amplification Resists Using Deep Ultraviolet and X-ray Radiation," *J. Vac. Sci. Technol. B*, vol. 6, no. 6, pp. 2303-2307, Nov/Dec 1988.

[5] S. Das, J. Thackeray, M. Endo, J. Langston, and H. Gaw, "A Systematic Investigation of the Photoresponse and Dissolution Characteristics of an Acid Hardening Resist," *SPIE Advances in Resist Technology and Processing VII*, vol. 1262, 1990.

[6] H. Fukuda and S. Okazaki, "Kinetic Model and Simulation for Chemical Amplification Resists," *J. Electrochem. Soc.*, vol. 137, no. 2, pp. 675-679, February 1990.

[7] D. Ziger, C. Mack, and R. Distasio, "The Generalized Characteristic Model for Lithography: Application to Negatively Chemically Amplified Resists," *SPIE Advances in Resist Technology and Processing VIII*, vol. 1466, 1991.

[8] R. Ferguson, J. Hutchinson, C. Spence, and A. Neureuther, "Modeling and Simulation of a Deep-UV Acid Hardening Resist," *J. Vac. Tech. B*, November/December 1990.

[9] F. Houlihan, A. Shugard, R. Gooden, and E. Reichmanis, "Nitrobenzyl Ester Chemistry for Polymer Processes Involving Chemical Amplification," *Macromolecules*, vol. 21, pp. 2001-2006, July 1988.

[10] F. Dill, W. Hornberger, P. Hauge, and J. Shaw, "Characterization of Positive Photoresist," *IEEE Trans. Electron Devices, vol. ED-22*, no. 7, pp. 445-452, July 1975.

[11] F. Houlihan, E. Reichmanis, L. Thompson, and R. Tarascon, "Chemically Amplified Resists," in *Polymers in Microlithography: Materials and Processes - ACS Symposium Series 412*, ed. E. Reichmanis, S. MacDonald, and T. Iwayanagi, pp. 39-56, American Chemical Society, 1989.

**Figure 7.1:** Resin structure and deprotection reaction for poly(t-BOC-styrene sulfone).

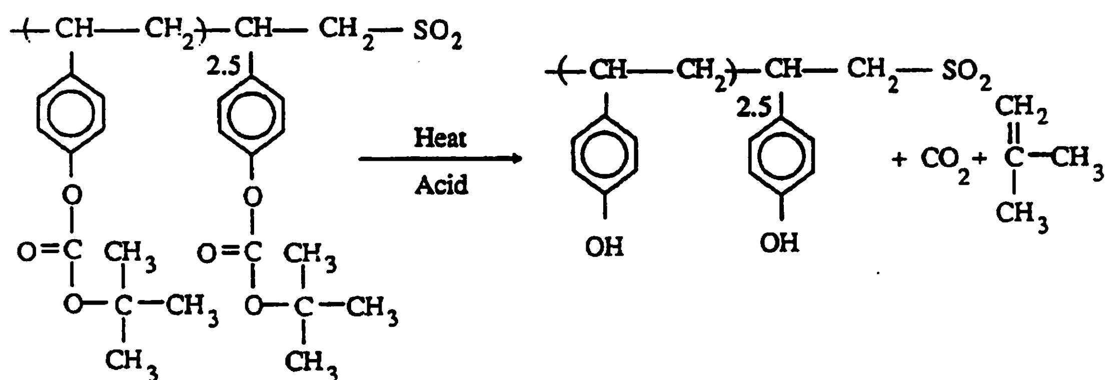


**Figure 7.2:** Acid generation reaction for a) the tosylate and b) the onium salt acid generators.

a)

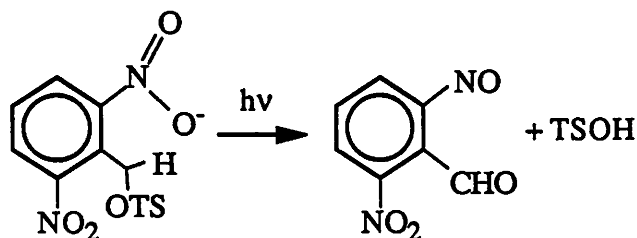


b)

**Figure 7.3:** Transmission versus exposure dose for a) the 12% tosylate mixture, b) the 2.5% onium salt mixture and the resin alone.

a)

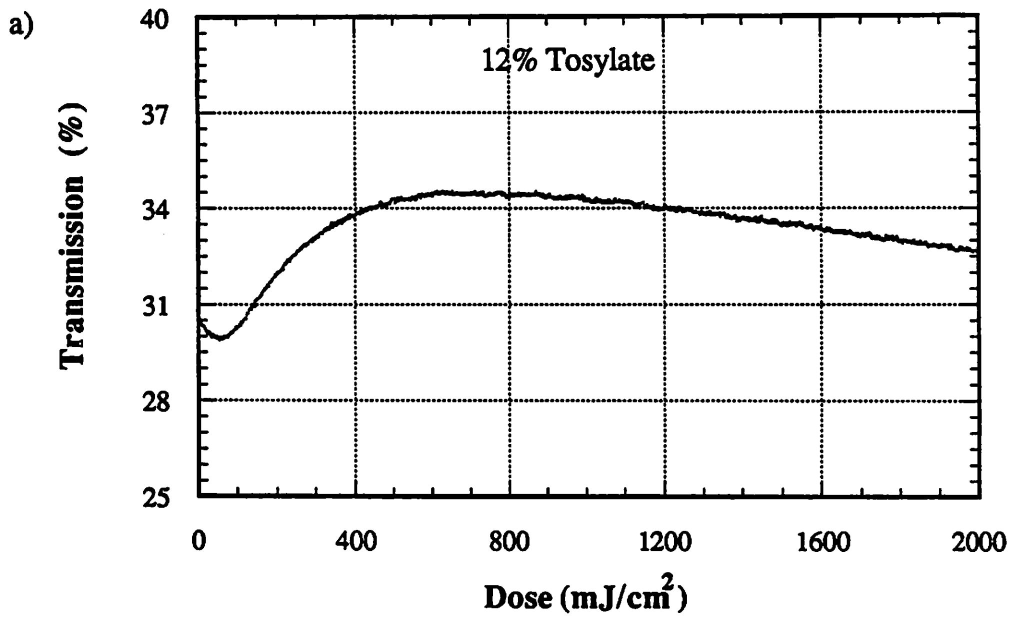


b)

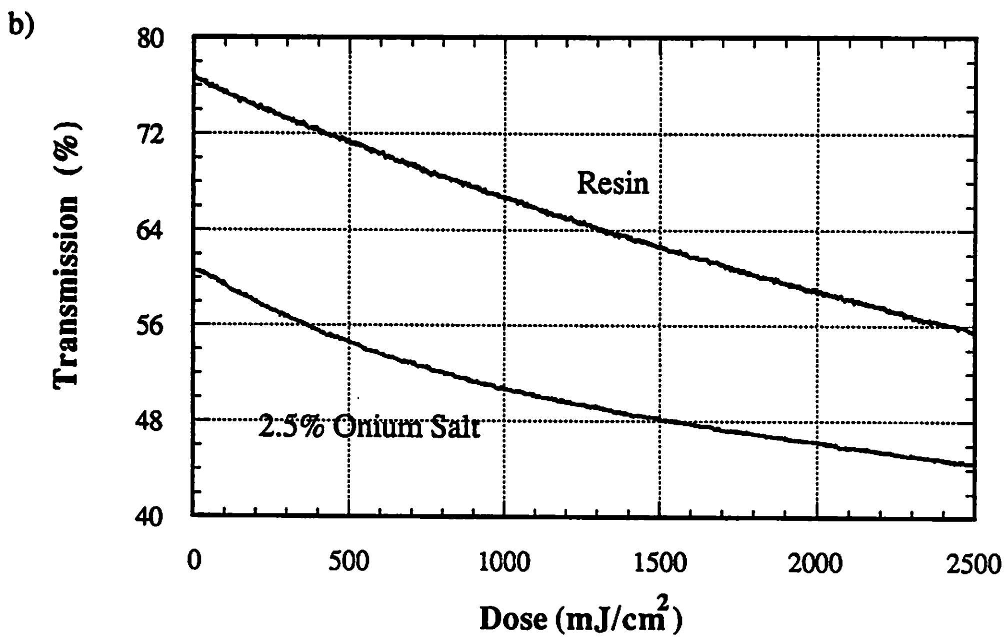

**Figure 7.4:** FTIR difference spectra for the 6% tosylate mixture after exposure doses of 50 $mJ/cm^2$ and 500 $mJ/cm^2$.

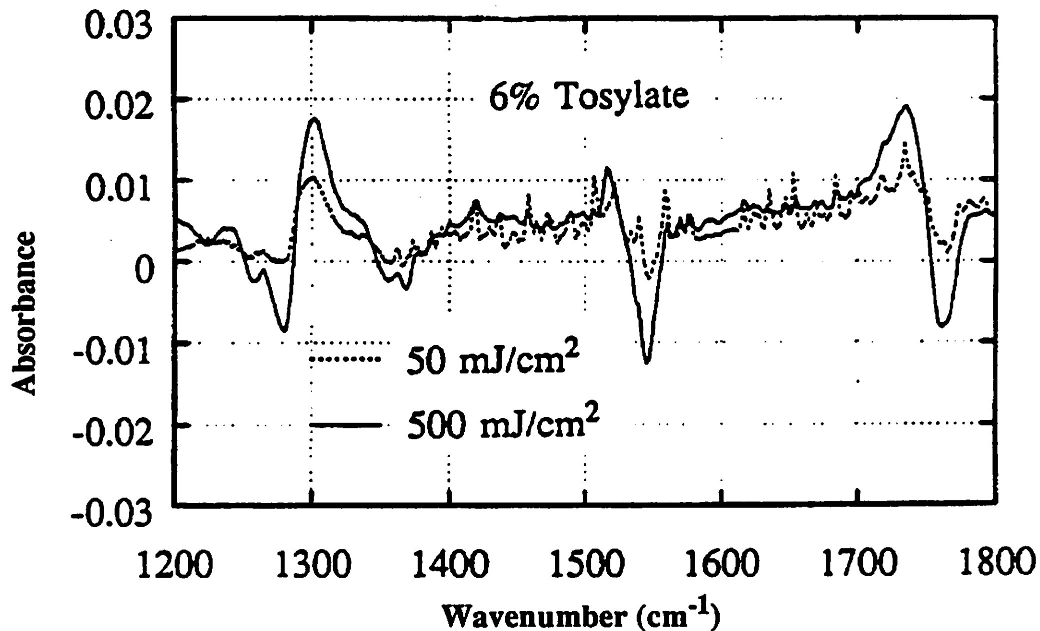


**Figure 7.5:** Normalized acid concentration versus exposure dose as determined from the FTIR peak near 1540 $cm^{-1}$ and from simulation with $C = 0.0045\ cm^2/mJ$.

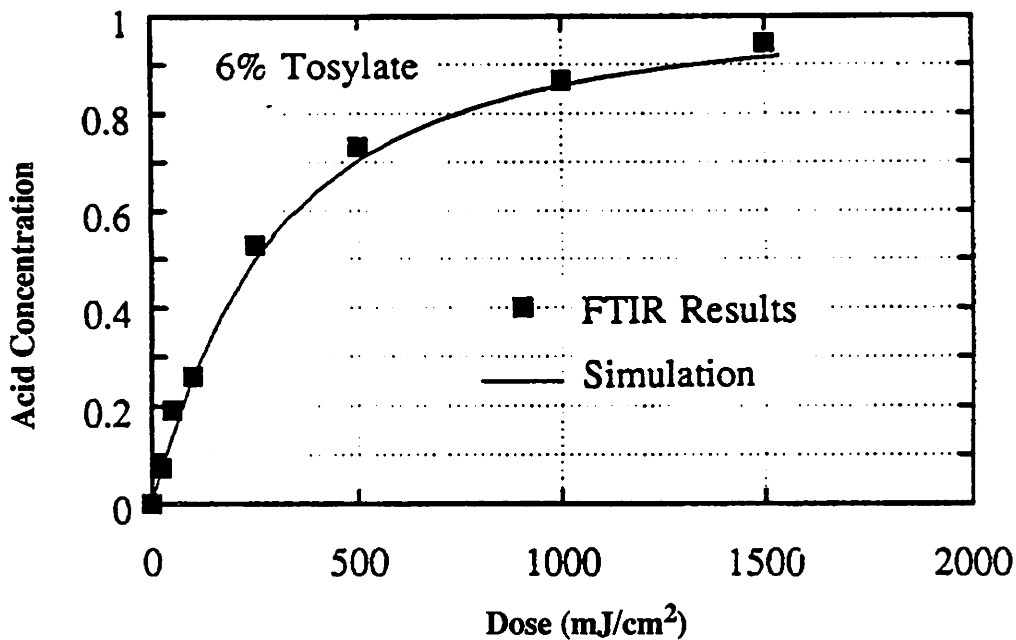

**Figure 7.6:** Transmission versus exposure dose for a 2:1 t-BOC styrene:styrene copolymer alone and with 5 weight percent onium salt.

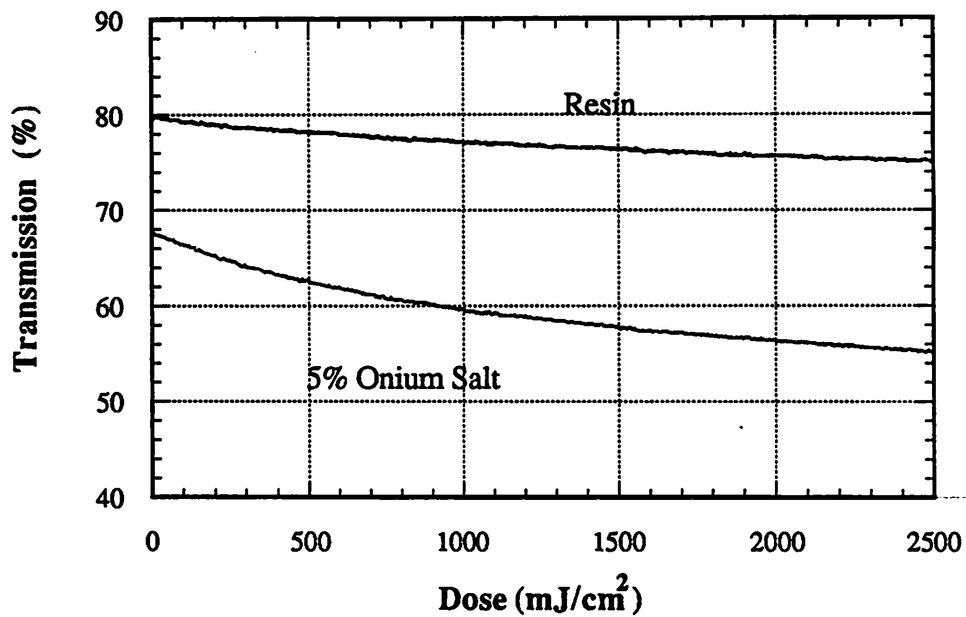


**Figure 7.7:** Typical FTIR spectra taken before and after the post-exposure bake. The peak at 1760 $cm^{-1}$ corresponding to the carbonyl bond is used to monitor the deprotection reaction.

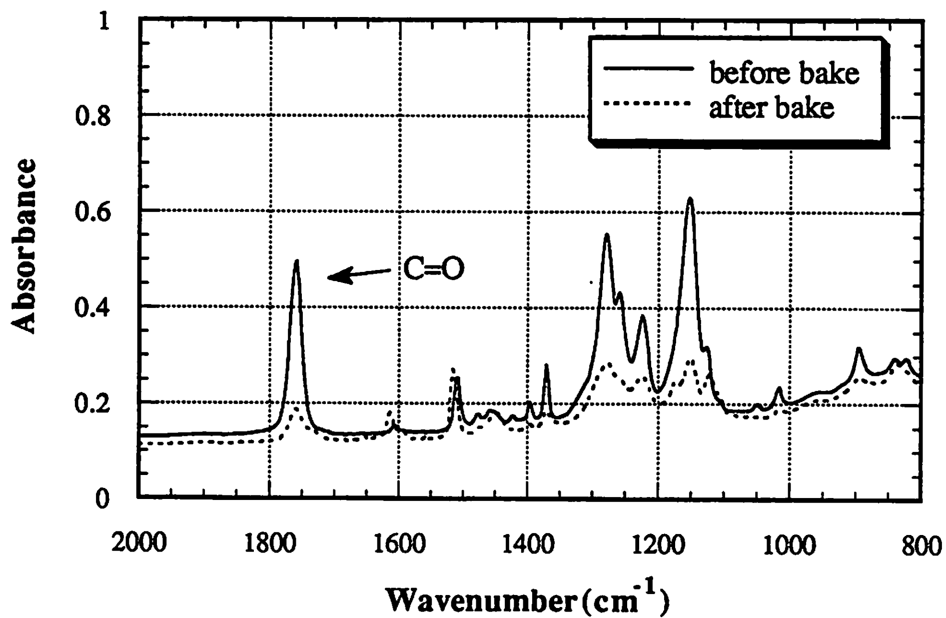

**Figure 7.8:** Normalized amount of deprotection versus bake time for the 12% tosylate mixture for bake temperatures of a) 95°C, b) 105°C, and c) 115°C.

a)

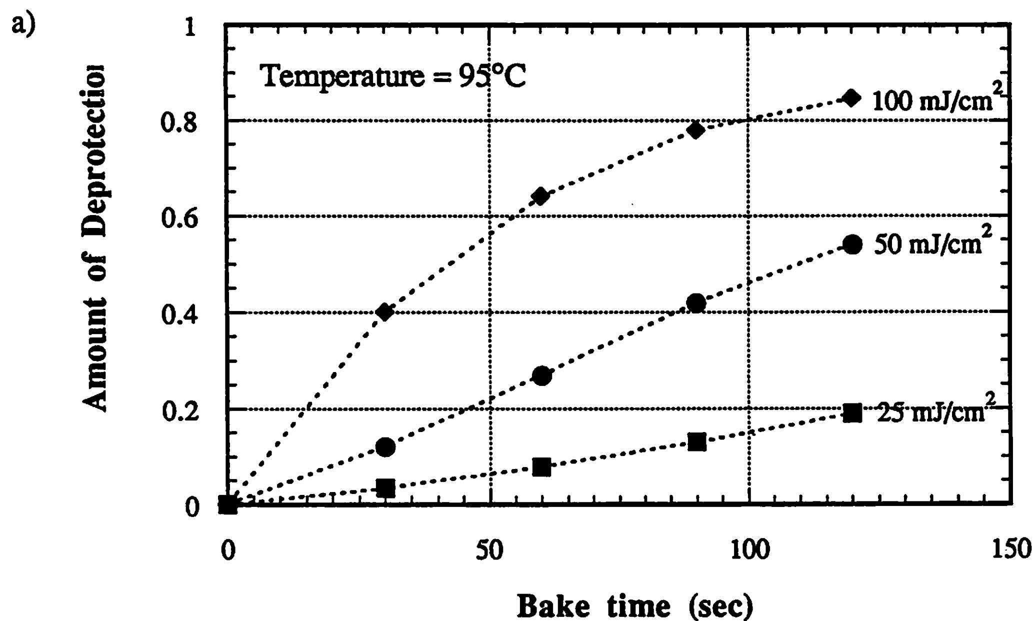


b)

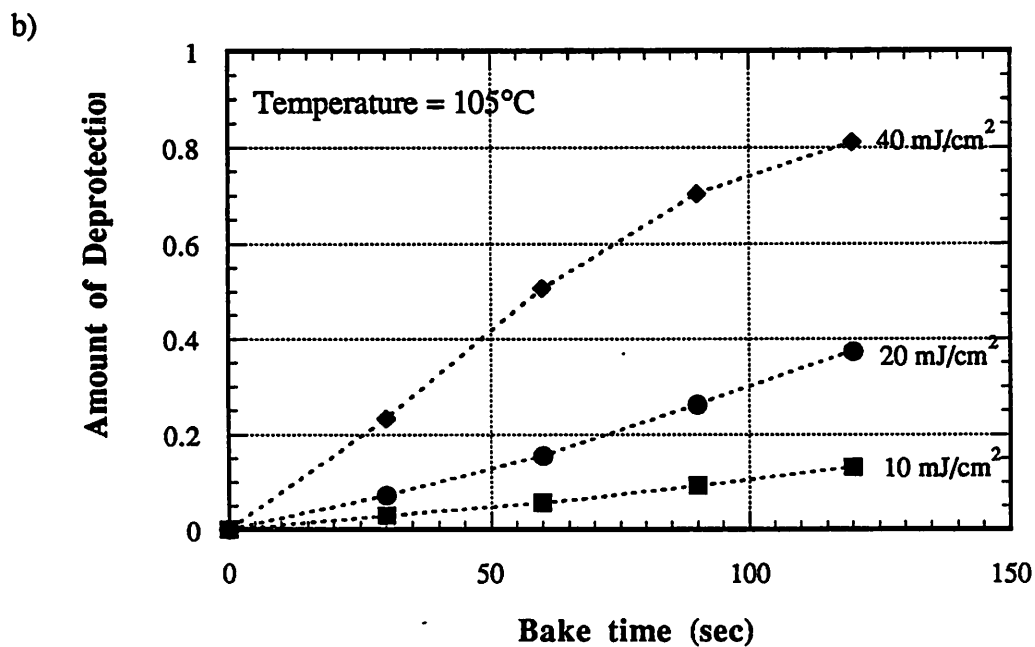

c)

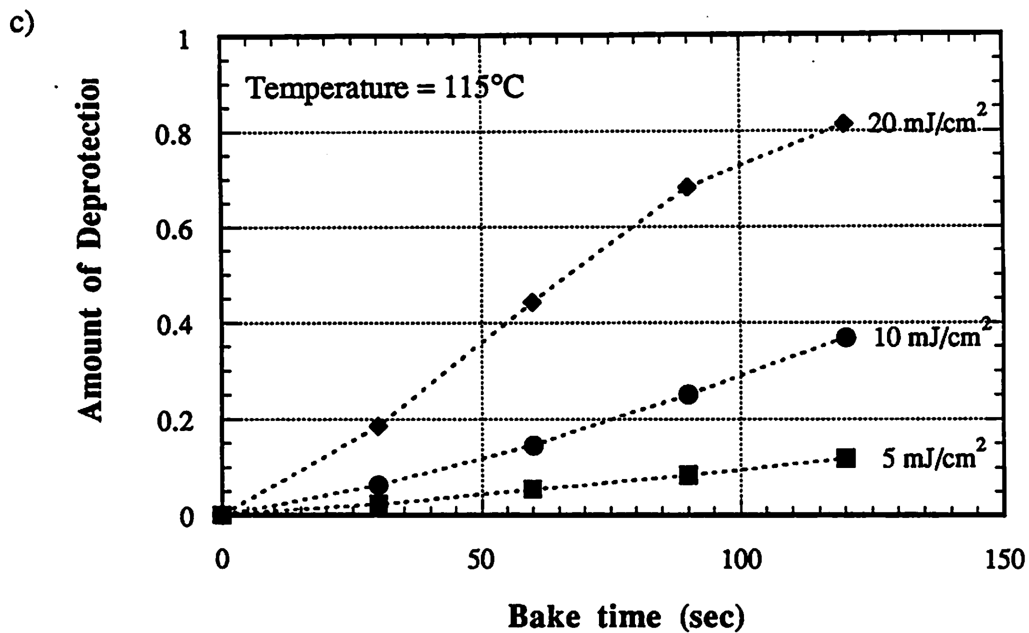


**Figure 7.9:** Normalized amount of deprotection versus bake time for the 2.5% onium salt mixture for bake temperatures of a) 95°C, b) 105°C, and c) 115°C.

a)

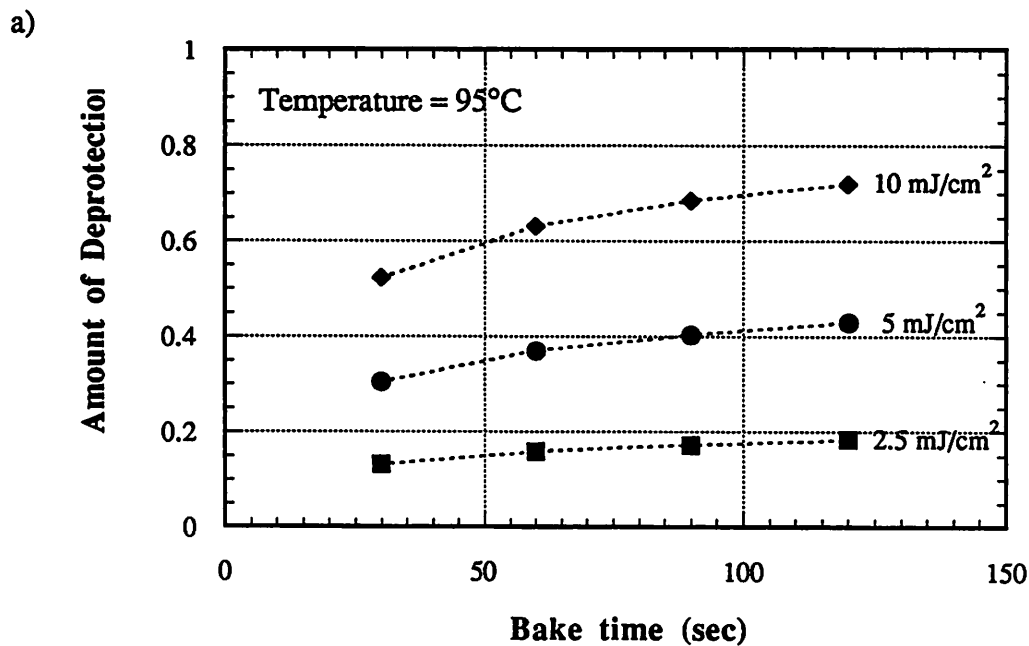

b)

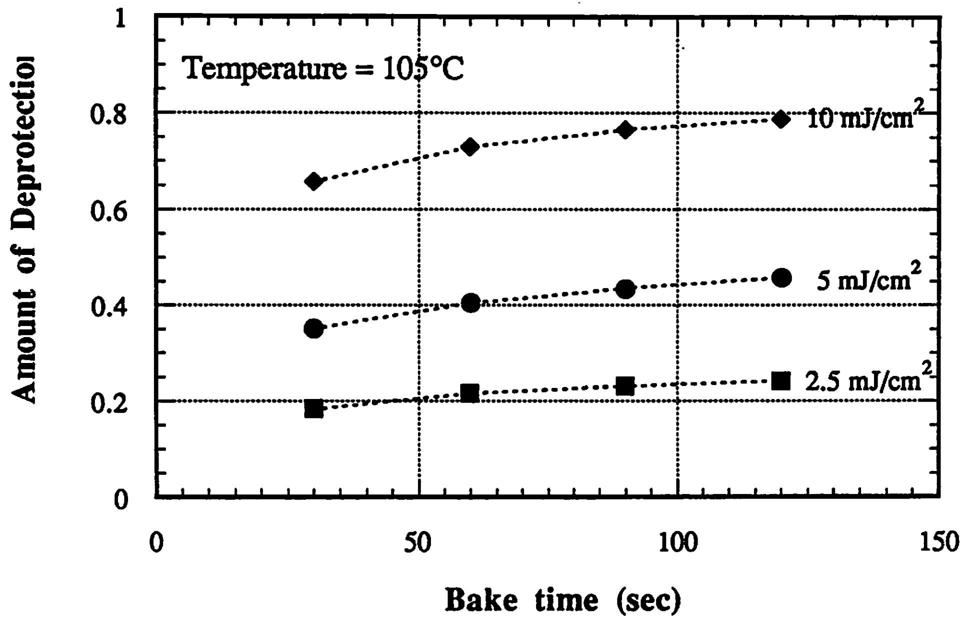


c)

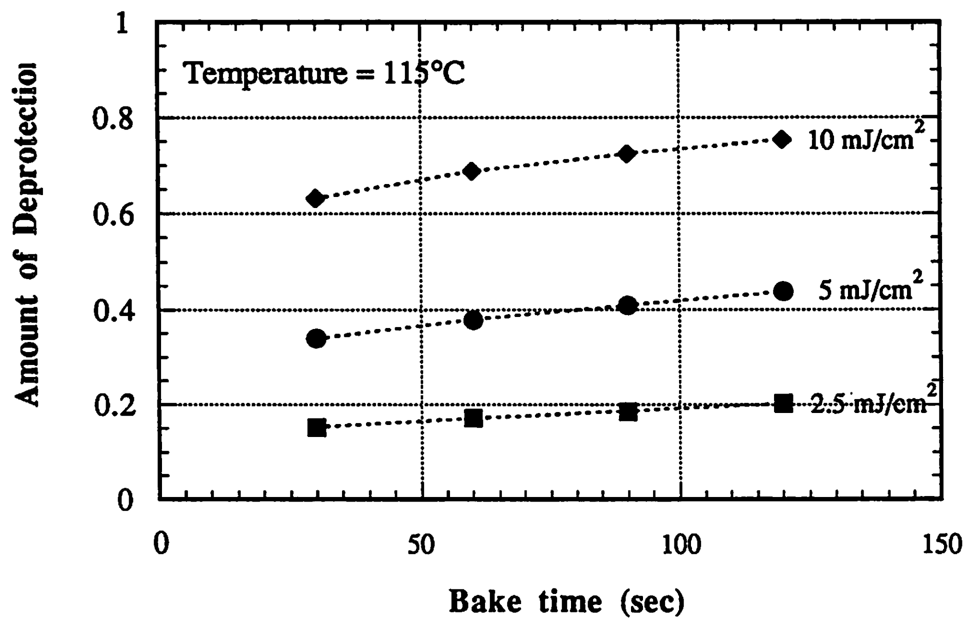

**Figure 7.10:** Comparison between FTIR results and a simple catalytic model for the 12% tosylate mixture at a bake temperature of 105°C.

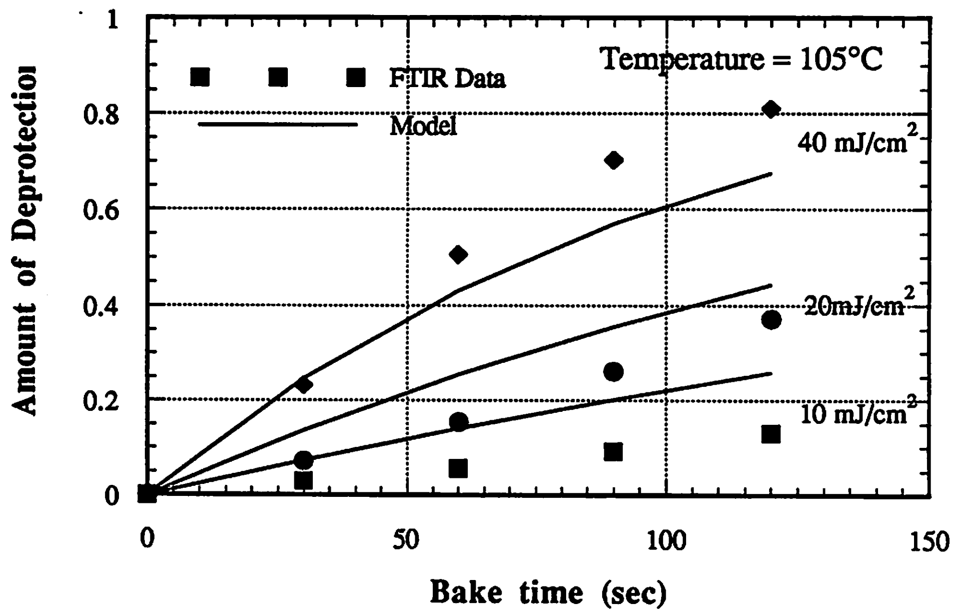

**Figure 7.11:** Comparison between FTIR results and the tosylate kinetic model using m = 1.8 for the 12% tosylate mixture at a bake temperature of 105°C.

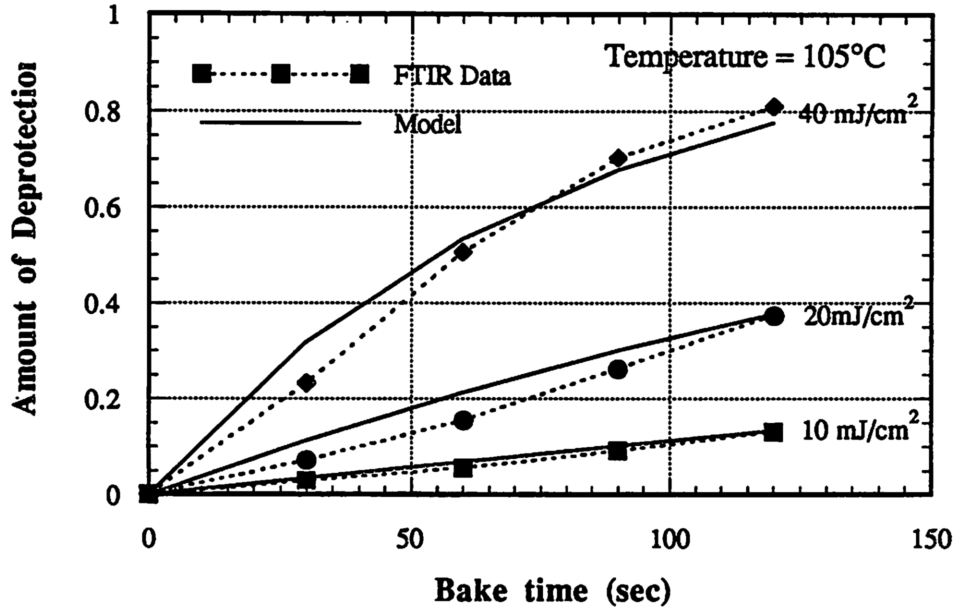


**Figure 7.12:** Comparison between FTIR results and the tosylate kinetic model using m = 1.3 for the 6% tosylate mixture at a bake temperature of 105°C.

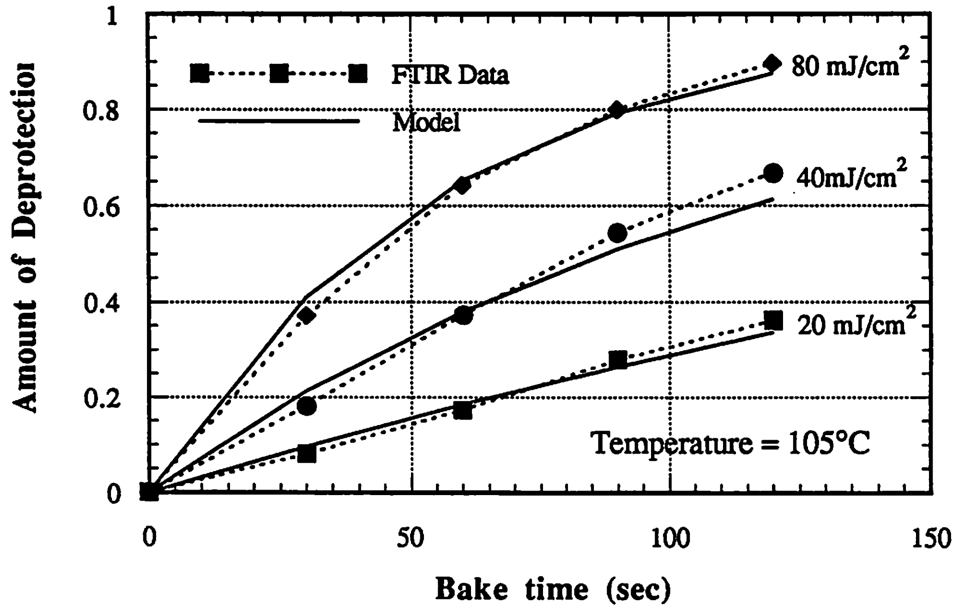

**Figure 7.13:** Comparison between FTIR results and the onium salt kinetic model using m = 1.2 for the 2.5% onium salt mixture at a bake temperature of 105°C.

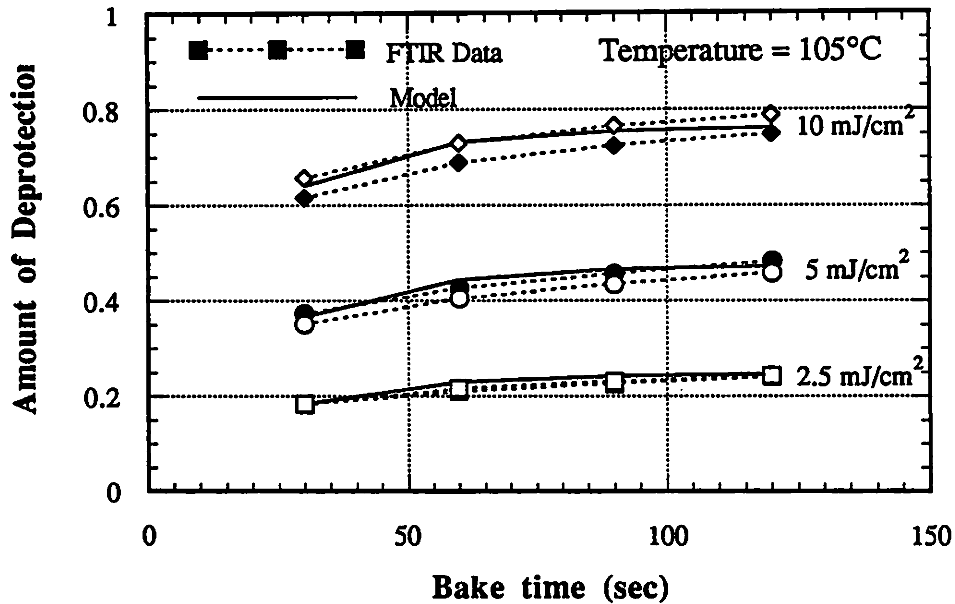


**Figure 7.14:** Comparison between FTIR results and the onium salt kinetic model using m = 1.6 for the 5% onium salt mixture at a bake temperature of 105°C.

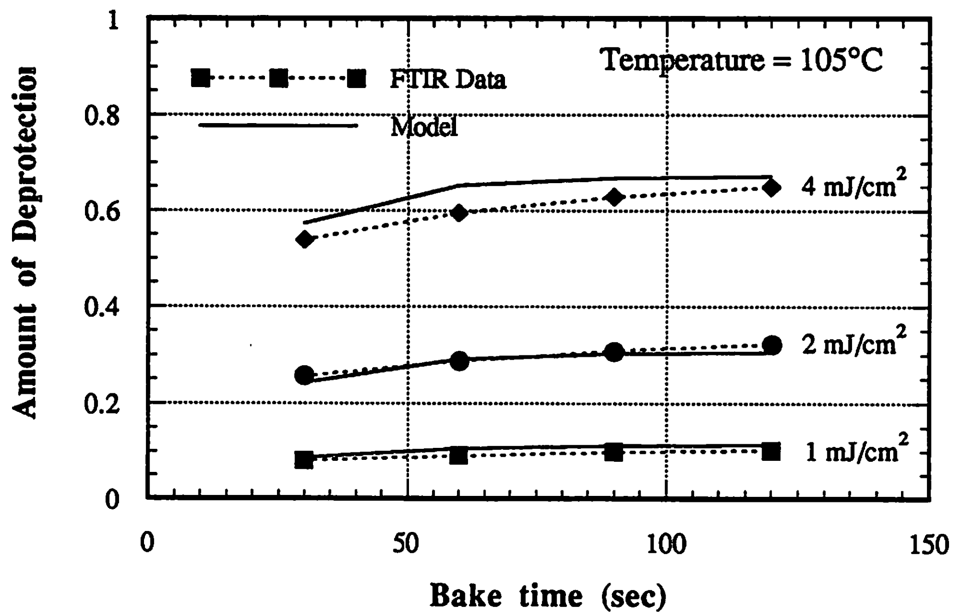

# CHAPTER 8

# CONCLUSIONS, COMMENTS, AND PERSPECTIVE

## 8.1 CONCLUSIONS

A comprehensive methodology has been developed for the characterization, modeling, and simulation of advanced resist technologies for optical lithography. This methodology relies upon a mechanistic approach in which the resist is described in terms of the basic chemical and physical changes that occur within the resist during processing. Key aspects of this methodology are the development of a new lithographic simulator based on reaction kinetics as well as the refinement of materials characterization techniques for quantitatively measuring and modeling these reactions. The application of this methodology to two state-of-the-art resist materials with chemical amplification has been successful in establishing predictive models for the accurate simulation of these resists under a variety of processing conditions as well as a more fundamental understanding of the basic mechanisms which determine their behavior.

The foundation of this methodology is a new lithography simulation program, *SAMPLE-ARK*. This program, an extension of *SAMPLE*, simulates the chemical and physical changes the resist undergoes during processing. The new addition to this program, a post-exposure bake simulation routine, tracks the concentration of up to ten chemical species in the resist as the bake progresses. The local concentrations of these species change during the bake as a result of a system of user-defined chemical reactions and diffusion coefficients which describe the particular resist process under simulation. Various input options provide for such possibilities as multiple chemical reactions, concentration-dependent diffusion coefficients, and diffusion into the resist from an outside source. The program calculates the

local species concentrations during the bake using a variable step Runge-Kutta numerical algorithm. At the conclusion of the bake, the user may specify an unlimited variety of dissolution rate functions using a basic set of operators to generate an algebraic expression in terms of any of the species concentrations within the resist.

A set of characterization techniques has been explored and refined for developing mechanistic models for use in ***SAMPLE-ARK***. Experimental methods such as optical transmission, FTIR spectroscopy, and interferometry have demonstrated success in monitoring the chemical and physical changes occurring within the resist during processing. Several new software packages have been written for automating the conversion of experimental data to kinetic models. One program designed for the quantitative analysis of FTIR data locates absorption bands within the spectrum and then evaluates the peak size through various methods including baseline fitting, area integration, maximum peak height determination, and peak-to-peak calculations. Other programs fit kinetic models to experimental exposure and bake data using nonlinear least squares fitting routines.

The power and flexibility of this new program were demonstrated by examining some fundamental issues associated with three complex resist technologies of importance today: image reversal, chemical amplification, and silylation. For example, in simulating the image reversal process, modifications to the post-exposure bake input description demonstrated that the incomplete conversion of ICA to indene during the bake can lead to a loss in sensitivity but has no significant effect on the resist contrast. For chemical amplification resists, the relationship between the exposure dose and the bake time in driving the catalytic reaction were explored. Finally, the silicon uptake was simulated for both a diffusion-controlled as well as a site-controlled silylation process. In the future, the development of more quantitative models describing the oxygen plasma etch will provide the opportunity to compare the performance of these fundamentally different silylation processes.

These characterization and modeling techniques as well as the simulation capabilities of ***SAMPLE-ARK*** have been used in the modeling of two state-of-the-art deep-UV resists that employ chemical amplification for high sensitivity. In Shipley SNR 248, an acid hardening resist, an acid catalyzed crosslinking reaction during the bake produces a negative-tone resist process. For this resist, a complete model describing the exposure, post-exposure bake, and development steps was derived in terms of the fundamental changes that occurred during each individual process step. FTIR spectroscopy was used for the direct observation of the crosslinking reaction. A dissolution rate expression was derived based upon molecular weight changes during the post-exposure bake. Overall, results of this study indicated that acid loss during the bake as well as the chemical structure of the crosslinking agent both play an important role in determining the resist performance. The inclusion of the exposure, bake, and development models in ***SAMPLE-ARK*** lead to the accurate simulation of resist development profiles which compared favorably with experimental SEM's over a variety of bake conditions and mask patterns.

In a second chemical amplification resist from AT&T, photo-generated acid catalyzes the removal of a t-BOC protecting group from the resin during the bake. FTIR spectroscopy was once again used to monitor the deprotection reaction. A complete study involving the mixture of various resist compositions demonstrated that both the type of acid generator as well as the concentration have significant effects on the resist behavior. For the resist with the onium salt, the deprotection reaction saturated at a dose-dependent level indicating the presence of an acid loss mechanism. However, in the resist with the tosylate, the deprotection reaction proceeded to completion for all exposure doses. In addition, increasing the loading of both acid generators resulted in improved resist contrast during the bake.

## 8.2 COMMENTS FOR FUTURE WORK

With the completion of this comprehensive methodology and its successful application to several important resist materials, it is appropriate at this time to add comments and ideas for further improvement. For the general simulator, ***SAMPLE-ARK***, these improvements concern the reduction of CPU time through improved algorithms and simplifying assumptions, further generalization to current models, and the implementation of additional physical phenomena. To improve upon the characterization and modeling aspects of this methodology, further automation and additional characterization techniques are needed.

The following suggestions for improvements to ***SAMPLE-ARK*** could result in considerable savings in CPU time. These suggestions are:

1. The implementation of one-dimensional diffusion in the vertical direction when the diffusion length is significantly smaller than lateral feature sizes.

2. Modification to the data structure for storing concentration-dependent diffusion coefficients to reduce the computation time associated with converting a string describing the diffusion coefficient to a number.

3. Replacement of the current routine for solving the system of differential equations with a more sophisticated algorithm having increased speed.

The following improvements would increase the generality of ***SAMPLE-ARK*** to encompass a larger class of resist mechanisms and processes. These suggestions are:

1. The inclusion of additional boundary conditions when solving the diffusion equation to allow for cases such as out-diffusion during the bake

2. The implementation of additional mechanisms such as thickness variations during the bake.

3. The implementation of stress effects such as those occurring during silylation.

During the application of this methodology to the deep-UV chemical amplification resists, several practical issues arose concerning the characterization and modeling techniques which should be addressed in the future. First of all, the time required to complete these models was excessively long. This development time must be shortened in order for this mechanistic approach to achieve widespread use as a valuable aid in the evaluation and optimization of complex resist processes. Of course, repeated application will lead to a more streamlined process with refined techniques, shortcuts, and an avoidance of the initial mistakes that occurred in the initial applications. However, in order to speed up the modeling process further, alternative in-situ characterization techniques for monitoring chemical changes during the bake should be sought whenever possible for increasing the data acquisition rate. The benefits derived from real time data acquisition were clearly visible in Chapter 5 when interferometric measurements were used to indirectly monitor the deprotection reaction in the t-BOC resist. Following the data collection, additional software is a necessity for automating the extraction of mechanistic models from the raw experimental data. New software for the kinetic modeling of exposure and bake data could be incorporated into existing programs such as ***PARMEX*** which extracts development model parameters from dissolution rate data.

In several instances, the proposed set of characterization techniques were unable to monitor the chemical or physical changes of interest. For example, in the SNR 248 resist, neither optical transmission or FTIR spectroscopy measurements could accurately account for the

generation of acid during exposure. In addition, these bulk measurement techniques were unable to evaluate the diffusion coefficient of the acid during the bake. Consequently, the current set of measurement techniques must be expanded to include a wider variety of characterization methods. Perhaps alternative techniques which are not consistent with standard processing procedures such as titration, gel permeation chromatography, nuclear magnetic resonance, and Rutherford backscattering spectroscopy to name a few should be considered in the future. However, the time required to implement new characterization methods must be balanced with the level of accuracy required in the model. Often, an approximating assumption can provide a desired level of accuracy without resorting to more sophisticated measurement techniques. For example, it was assumed that the diffusion length for the acid in the SNR 248 resist was sufficiently long to blur out the vertical standing wave pattern without affecting to the lateral resolution capabilities of the resist.

## 8.3 A FINAL PERSPECTIVE

The goal of achieving a comprehensive methodology for the characterization, modeling, and simulation of advanced resist processes has been attained. The simulation program, ***SAMPLE-ARK***, provides a major advancement in simulation capability in that it is now possible to address the resist behavior in terms of chemical and physical mechanisms during processing for complex technologies such as image reversal, chemical amplification, and silylation. Materials characterization techniques have been refined to monitor the behavior of spin-coated resists during the exposure, post-exposure bake, and development processes. In addition, new modeling software has begun to automate the generation of mechanistic models from experimental data. These combined capabilities should be of interest during many stages of lithographic materials development such as research on mechanisms, tuning resist components, optimization of process conditions, diagnosing production problems, and even hypothetical materials studies. It is hoped that the ***SAMPLE-ARK*** program as well as

the refined characterization techniques will find wide spread applications throughout the IC industry.

# Appendix

## *SAMPLE-ARK* Program Commands

This section describes the complete set of commands for use with the *SAMPLE-ARK* bake routine. While these commands represent the current status of *SAMPLE-ARK*, changes to these commands including further additions will most likely occur before the final release of the code.

The command format is similar to the standard *SAMPLE* command structure, but contains some important differences. In the descriptions below, the keywords are emphasized with bold-faced type. Additional words or entries that must be included in the command are written in standard font. User-specified parameters are italicized. *SAMPLE-ARK* contains a unique feature in that the chemical species within the resist are identified through different names assigned by the user. These names are represented by the *species* entries in the commands that follow.

**startbake** [*matrix*]

The **startbake** statement initiates the post-exposure bake routine. The optional *matrix* parameter specifies the *SAMPLE* exposure matrix that gets sent to the post-exposure bake routine. When *matrix* is equal to 0, the RMZDOS matrix which contains M, or the PAC concentration, as a function of depth and exposure dose is sent. this option is used for increased speed when no diffusion occurs during the bake. The program defaults to this option. When *matrix* is equal to 1, the RMXZ matrix which contains M as a function of position within the resist is sent. This option must be used in conjunction with any diffusion within the resist.

**endbake**

The **endbake** statement completes the simulation of the post-exposure bake and returns control to the standard *SAMPLE* routines.

**temperature** *temp*

The **temperature** statement specifies the bake temperature for the post-exposure bake. The *temp* parameter gives the bake temperature in degrees Celsius.

**time** *time*

The **time** statement specifies the length of time for the post-exposure bake. The *time* parameter gives the bake time in seconds.

**reaction** k = *k* [ea = *ea*] in = *species#1* [,*species#2*, ...] out = *species#i* [,*species#j* ,...]

The **reaction** statement specifies a chemical reaction during the post-exposure bake. Any number of reactions can be specified in the post-exposure bake description. When an activation energy is not specified with "ea", the rate coefficient is given by *k*. When an activation energy is specified, the rate coefficient has an Arrhenius behavior with *k* as the pre-exponential term and *ea* as the activation energy in eV. The reactants are specified following "in" and the products are specified following "out".

**initialize** *species* [expose]/[expose_inv] *conc*

The **initialize** statement initializes the concentration of *species* at each point in the resist. When "expose" or "expose_inv" are not present, the concentration is uniformly initialized to *conc*. When the "expose" command is given, the concentration is initialized to the M matrix obtained from the ***SAMPLE*** exposure routine and is scaled by *conc*. The "expose_inv" command initializes the concentration to 1-M.

**define** *species expression*

The **define** statement specifies the concentration of *species* at each point in the resist through an algebraic expression constructed from the algebraic operators summarized in the table below, other species concentrations, and mathematical constants (see Chapters 3 and 4 for examples).

**return** *species*

The **return** statement returns the concentration matrix of *species* to the standard ***SAMPLE*** development routine.

**diffuse** *species expression*

The **diffuse** statement specifies the diffusion coefficient of *species*. The diffusion coefficient is given by *expression* which is constructed using the same method as described for the **define** statement. This expression can be given as a single constant for simple diffusion or as an expression in terms of any species concentrations for concentration-dependent diffusion.

**diffsource** *species conc*

The **diffsource** command alters the boundary conditions at the resist surface such that *species* is diffused into the resist from an outside source. The *conc* parameter specifies the solid solubility concentration at the resist surface.

**Table of operators for constructing algebraic expressions**

| Operator | Description |
|---|---|
| + | Addition |
| - | Subtraction |
| * | Multiplication |
| / | Division |
| ^ | Raise to power |
| ( ) | Parentheses |
| exp( ) | $e^x$ |
| log( ) | Log (base 10) |
| ln( ) | Natural Log |